

DESIGN OF MINIATURIZED KU BAND NARROWBAND CAVITY FILTER

A THESIS SUBMITTED TO  
THE GRADUATE SCHOOL OF NATURAL AND APPLIED SCIENCES  
OF  
MIDDLE EAST TECHNICAL UNIVERSITY

BY

YUSUF SEVİNÇ

IN PARTIAL FULFILLMENT OF THE REQUIREMENTS  
FOR  
THE DEGREE OF DOCTOR OF PHILOSOPHY  
IN  
ELECTRICAL AND ELECTRONICS ENGINEERING

FEBRUARY 2018



Approval of the Thesis:

**DESIGN OF MINIATURIZED KU BAND NARROWBAND CAVITY  
FILTER**

submitted by **YUSUF SEVİNÇ** in partial fulfillment of the requirements for the degree of **Doctor of Philosophy in Electrical and Electronics Engineering Department, Middle East Technical University** by,

Prof. Dr. Gülbin Dural Ünver  
Dean, Graduate School of **Natural and Applied Sciences** \_\_\_\_\_

Prof. Dr. Tolga Çiloğlu  
Head of Department, **Electrical and Electronics Engineering** \_\_\_\_\_

Prof. Dr. Şimşek Demir  
Supervisor, **Electrical and Electronics Engineering Dept., METU** \_\_\_\_\_

**Examining Committee Members**

Prof. Dr. Sencer Koç  
Electrical and Electronics Engineering Dept., METU \_\_\_\_\_

Prof. Dr. Şimşek Demir  
Electrical and Electronics Engineering Dept., METU \_\_\_\_\_

Prof. Dr. Özlem Aydın Çivi  
Electrical and Electronics Engineering Dept., METU \_\_\_\_\_

Assoc. Prof. Dr. Mehmet Ünlü  
Electrical and Electronics Engineering Dept.,  
Yıldırım Beyazıt University \_\_\_\_\_

Assoc. Prof. Dr. Özlem Özgün  
Electrical and Electronics Engineering Dept.,  
Hacettepe University \_\_\_\_\_

**Date:** 28 /02/2018

**I hereby declare that all information in this document has been obtained and presented in accordance with academic rules and ethical conduct. I also declare that, as required by these rules and conduct, I have fully cited and referenced all material and results that are not original to this work.**

Name, Last Name : Yusuf Sevinç

Signature :

## **ABSTRACT**

### **DESIGN OF MINIATURIZED KU BAND NARROWBAND CAVITY FILTER**

Sevinç, Yusuf

Ph.D., Department of Electrical and Electronics Engineering

Supervisor: Prof. Dr. Şimşek Demir

February 2018, 115 pages

Frequency multiplexer structures are of a crucial role as an essential part of huge variety of communication systems including, satellite-communication systems, wireless communication systems and radio transmission. They are indispensable multiple port components that are used for combination and separation of specific signals or frequency bandwidths selectively from a single signal or frequency bandwidth in multiplexing communication system. The main blocks that form a multiplexer are a set of filters, named as channel filters, and junctions connecting to filters to the common port. In satellite-communication systems, waveguide filter structures are mostly preferred and employed as channel filter in multiplexing configuration due to the fact that they are of low insertion loss, high power handling capability and high quality factor. On the other, bulkiness and large sizes of them are

troublesome in satellite-communication applications. Therefore, one of the main goals of this thesis is to design miniaturized, compact and weight-reduced channel filter structure including coupled resonators. Also, developing a framework for methodical design involving surface roughness effect and physically realizing the waveguide filter structure as a significant part of the multiplexer with lowest possible size and weight and sharp passband characteristic to be minimized the adjacent channel interference is in the main scope of this study.

Keywords: Waveguide filter, frequency multiplexer, cavity resonator, conductor surface roughness

## ÖZ

### **KU BANT DAR BANTLI MİNYATÜRİZE EDİLMİŞ KAVİTE FİLTRE TASARIMI**

Sevinç, Yusuf

Doktora, Elektrik ve Elektronik Mühendisliği Bölümü

Tez Yöneticisi : Prof. Dr. Şimşek Demir

February 2018, 115 sayfa

Frekans çoklayıcı yapıları; uydu haberleşme sistemleri, kablosuz haberleşme sistemlerini ve radio iletimini içeren çok çeşitli haberleşme sistemlerinin önemli bir parçası olarak mühim bir role sahiptir. Çok portlu sistemlerde tek bir sinyalden veya frekans band genişliğinden belirli sinyallerin veya frekans band genişliklerinin seçici bir şekilde birleştirilmesinde ve ayrılmasında kullanılan vazgeçilmez çok portlu elemanlardır. Bir çoklayıcıyı oluşturan temel bloklar kanal filtresi olarak adlandırılan filtre seti ve filtreleri ortak porta bağlayan eklem kısımlarıdır. Dalga klavuzu filtre yapıları, çoklayıcı konfigürasyonunda düşük iletim kaybına, yüksek güç taşıma yeteneğine ve yüksek kalite faktörüne sahip olmalarından dolayı uydu haberleşme sistemlerinde kanal filtresi olarak çoğunlukla tercih edilir ve kullanılır. Bununla birlikte, bu yapıların hantallığı ve büyük boyutları uydu haberleşmesi

uygulamalarında sorun yaratmaktadır. Bu sebeple, bu tezin ana amaçlarından birisi bağımlı rezonatörler içeren miniaturize, kompakt ve ağırlığı düşürülmüş kanal filtre tasarımı olacaktır. Ayrıca yüzey pürüzlülük etkisini içeren sistematik tasarım için bir çerçeve çizmek ve mümkün olan en düşük ağırlık ile boyuta sahip ve komşu kanallar arası girişimin minimize edilmesi için keskin geçiş bandı karakteristiğine sahip çoklayıcı yapılarının önemli bir parçası olan dalga kılavuzu filtre yapısının gerçekleştirilmesi de bu çalışmanın kapsamı içerisindedir.

Anahtar kelimeler: Dalga kılavuzu filtreler, frekans çoklayıcılar, kavite rezonatörler, iletken yüzey pürüzlülüğü



*To my family...*

## ACKNOWLEDGEMENTS

I would like to express my gratitude to my advisor, Prof. Dr. Şimşek Demir for his guidance and encouragement. Having his supervision throughout my graduate education is privilege and a great honor for me. I would also like to thank member of my thesis committee Prof. Dr. Özlem Aydın Çivi and Assoc. Prof.Dr. Mehmet Ünlü for their guiding comments and recommendations during my study.

I would especially thank Mechanical Design Unit of ASELSAN Inc, Ertuğrul Kolağasıoğlu, Serdar Terzi and Bilal Bilgin for their priceless support in fabrication and measurement activities of my thesis.

I would also thank Alper Yalım, Orçun Kiriş, Enis Kobal and Çağrı Çetintepe for their friendship and invaluable helps.

I would express my deepest appreciation to my family for their unprecedented support. I cannot complete my thesis successfully without their love, encouragement and endurance. I dedicate this thesis to them as a show of my appreciation.

## TABLE OF CONTENTS

ABSTRACT .....	v
ÖZ .....	vii
ACKNOWLEDGEMENTS .....	x
LIST OF TABLES .....	xiv
LIST OF FIGURES.....	xvi

### CHAPTERS

1. INTRODUCTION.....	1
1.1 Satellite Payload System .....	1
1.2 Research Aim and Organization.....	2
1.3 Achievements and Accomplishments.....	4
2. LITERATURE SURVEY .....	7
2.1 Literature Review on Microwave Waveguide Filters and Multiplexer Structures .....	7
2.1.1 Multiplexer Configurations .....	7
2.1.2 Review of the Prior Studies on Contiguous-Channel Waveguide Multiplexers.....	11

2.2 Microwave Waveguide Filters .....	19
2.2.1 Evanescent-Mode Waveguide Filters .....	19
2.2.2 Coupled Cavity Filters .....	23
2.2.3 Dielectric Resonator Filters .....	25
2.2.4 E-Plane Filters.....	27
2.3 Review of the Prior Studies on Influence of Conductor Surface Roughness on Microwave Structures.....	32
3. CHANNEL FILTER DESIGN.....	37
3.1 Generalized Design Methodology .....	37
3.2 Calculation of the Filter Order.....	41
3.3 Developing a design framework for miniaturized waveguide channel filter.....	42
3.3.1 Design of the Direct-Coupled Waveguide Filter .....	42
3.3.2 Construction of Circuit Equivalent Model.....	52
4. MANIFOLD-COUPLED MULTIPLEXER DESIGN.....	65
4.1 Multiplexer Design Studies with the Analysis of Various Approaches .	65
4.1.1 Design of the Manifold via Short-Circuited Method.....	65
4.1.2 Design of the Manifold with E-plane T-junctions .....	71
4.2. Development of Design Framework for the Contiguous Band Multiplexer	74

4.2.1 Design Procedure of the H-Plane Manifold Coupled Multiplexer.....	74
5. ANALYSIS OF THE SURFACE ROUGHNESS EFFECT ON FILTERING PERFORMANCE AND EXPERIMENTAL ACTIVITIES .....	85
5.1 TRL Calibration Procedure .....	86
5.2 Analysis of the Surface Roughness Effect with Realization and Measurement of the Channel Filter .....	89
6. CONCLUSIONS .....	101
REFERENCES.....	105
CURRICULUM VITAE .....	113

## LIST OF TABLES

### TABLES

Table 3.1 Comparison between different realization technologies [3] .....	38
Table 3.2 Calculated design parameters .....	50
Table 3.3 Calculated lengths and distances .....	50
Table 3.4 Effect of iris aperture on circuit parameters for $t=0.4$ mm and $t=0.6$ mm	54
Table 3.5 Effect of iris aperture on circuit parameters for $t=0.8$ mm and $t=0.9$ mm	54
Table 3.6 Effect of iris aperture on circuit parameters for different thickness values .....	58
Table 3.7 Lengths ( in millimeters) of the transmission lines .....	59
Table 3.8 Values of the capacitances in series.....	59
Table 3.9 Values of the inductances (in nH) in parallel and series.....	59
Table 3.10 Parameter values (in millimeters) for the channel filters.....	64
Table 4.1 Gap distance values (in millimeters) for H-plane manifold .....	79
Table 4.2 Resonator length values (in millimeters) for H-plane manifold .....	80

Table 4.3 Channel performances of the multiplexer .....	80
Table 4.4 Parameter values (in millimeters) for the six fifth-order channel filter.....	82
Table 4.5 Gap distance values (in millimeters) for H-plane manifold .....	84
Table 4.6 Resonator length values (in millimeters) for H-plane manifold.....	84

## LIST OF FIGURES

### FIGURES

Figure 1.1. Layout of a satellite payload system [1].....	2
Figure 2.1. Basic block diagram of a satellite payload. ....	8
Figure 2.2. Schematic of Hybrid-coupled multiplexer. ....	8
Figure 2.3. Directional filter multiplexer. ....	9
Figure 2.4. Circulator-coupled multiplexer. ....	9
Figure 2.5. Manifold-coupled multiplexer.....	10
Figure 2.6. Manifold MUX configurations: (a) comb, (b) herringbone, (c) one filter feeding.....	10
Figure 2.7. Block diagram of three-channel multiplexer proposed in [6]. ....	11
Figure 2.8. Cross sectional view of three-channel multiplexer proposed in [6]......	12
Figure 2.9. Representation of a dielectric filled cavity bandpass filter in [7].....	13
Figure 2.10. Horizontal and vertical cross-sectional view of 6-8.6 GHz cavity filter in [8].....	13
Figure 2.11. Seven-channel manifold multiplexer in [10].....	14
Figure 2.12. Ten-channel manifold multiplexer with circular waveguides in [12]. .	15
Figure 2.13. Six-channel manifold multiplexer with rectangular waveguides in [13]. .....	16
Figure 2.14. Evanescent mode waveguide filters (a) with screws, (b) with dielectrics [31].....	20



Figure 2.15. (a) T, (b) $\pi$ equivalent circuit model of evanescent mode WG for $l$ length [35].	21
Figure 2.16. Lumped circuit model for Evanescent-mode WG filter in [35].	21
Figure 2.17. Electric field distribution in (a) single ridge (b) double ridge [39].	22
Figure 2.18. Equivalent circuit model for rectangular ridge waveguide [39].	22
Figure 2.19. Circular cavity filters (a) with tuning screws and coupling iris (b) with opening obstacles [31].	23
Figure 2.20. Bimodal rectangular cavities with small cuts [31].	24
Figure 2.21. Dual-mode band-pass filter in [44].	24
Figure 2.22. Dielectric resonator filters (a) axially positioned (b) laterally positioned resonators [31].	26
Figure 2.23. E-plane filter (a) filter structure (b) metallization types [31].	27
Figure 2.24. E-plane filters with metallic inserts (a) one insert (b) two parallel inserts [31].	27
Figure 2.25. Periodically loaded E-plane waveguide filters [55].	28
Figure 2.26. Fabricated E-plane resonator in [56].	28
Figure 2.27. Micromachined cavity filter in [60].	29
Figure 2.28. Quartz-loaded WG filter proposed in [61].	30
Figure 2.29. Morgan-Jensen model [65].	33
Figure 2.30. Snowball model [65].	34
Figure 3.1. Filter design procedure [1].	40
Figure 3.2. Ideal filter response.	42

Figure 3.3 (a) Direct-coupled filter, (b) equivalent circuit of n section coupled filter. .....	43
Figure 3.4. Low pass prototype with 'g' constants.....	44
Figure 3.5. (a) Iris filter scheme, (b) impedance inverter representation of iris filter. .....	47
Figure 3.6. Circuit parameters of symmetrical inductive iris [62].....	49
Figure 3.7. View of the direct-coupled filter. ....	51
Figure 3.8. S-parameters for analytically calculated parameters without optimization .....	52
Figure 3.9. Inductive iris and its representation as impedance inverter.....	53
Figure 3.10. Inductance variation curves with respect to changing gap distance.....	53
Figure 3.11. $S_{21}$ curves as $d=6$ mm in full-wave and circuit level (dashed line: full-wave simulation result, solid line: circuit simulation result). ....	55
Figure 3.12. $S_{21}$ curves as $d=6$ mm in full-wave and circuit level (dashed line: full-wave simulation result, solid line: circuit simulation result). ....	56
Figure 3.13. Inductive iris and its representation for larger iris thickness.....	57
Figure 3.14. Phase of $S_{21}$ as $d=6$ mm and $t=1$ mm in full-wave and circuit level. ....	57
Figure 3.15. Shunt inductance variation curves with respect to changing gap distance. ....	58
Figure 3.16. (a) Circuit schematic, (b) filter response of the direct-coupled filter ...	60
Figure 3.17. Comparison of the passband responses at $f_{center} : 16.954$ GHz (dashed black: passband response of the design from scratch, solid red: passband response with scaling).....	61

Figure 3.18. Passband responses of the filters at different center frequencies.....	62
Figure 3.19. Passband responses of the filters at different center frequencies.....	63
Figure 4.1. Manifold-coupled multiplexer. ....	66
Figure 4.2.(a) Parallel connection, (b) series connection of two short-circuited waveguide [28]. ....	66
Figure 4.3. (a) Three-channel multiplexer with short circuits (b) Group delay response of the common port with short circuits for three-channel multiplexer.....	69
Figure 4.4. (a) View of three-band contiguous band multiplexer, (b) S-parameter results for the contiguous band MUX, (c) Transmission characteristic of each band. ....	70
Figure 4.5. (a) Modified E-plane manifold, (b) Triple band multiplexer with filter-loaded manifold, (c) Transmission and reflection response .....	72
Figure 4.6. (a) Modified E-plane manifold, (b) Triple band multiplexer with filter-loaded manifold, (c) Transmission and reflection response .....	73
Figure 4.7. Layout of six-channel H-plane manifold .....	75
Figure 4.8. Circuit model of multiplexer with ideal transmission lines .....	75
Figure 4.9. Channel transmission for the circuit model of MUX (a) before, (b) after optimization process. ....	76
Figure 4.10. Circuit model of multiplexer with full-wave equivalent blocks. ....	77
Figure 4.11. Channel transmission of the MUX with full-wave equivalent blocks. .	77
Figure 4.12. Three-dimensional view of six-channel multiplexer. ....	78
Figure 4.13. (a) Channel transmission of the multiplexer, (b) passband of the channels. ....	79

Figure 4.14. Three-dimensional view of six-channel multiplexer in X-band.....	81
Figure 4.15. Transmission and reflection response of the filter. ....	82
Figure 4.16. Channel transmission of the multiplexer (Step1). ....	83
Figure 4.17. Channel transmission of the multiplexer (Step2). ....	83
Figure 4.18. Channel transmission of the multiplexer (Step3). ....	84
Figure 5.1. TRL calibration procedure (a) Error model with DUT for TRL calibration, (b) Thru connection, (c) Reflect connection, (d) Line connection .....	87
Figure 5.3.(a) Perspective, (b) Vertical-cut view of the fabricated channel filter, ...	90
Figure 5.4. Measured and simulated S-parameters for the channel filter. ....	91
Figure 5.5. Snowball model for surface irregularities in cross section.....	92
Figure 5.6. (a) Cut-view of the channel filter with rough surfaces, (b) circuit schematic of the channel filter including $R_{\text{rough}}$ and $L_{\text{rough}}$ .....	93
Figure 5.7. Transmission and rejection characteristics of the channel filter in circuit level and full-wave simulator for (a) radius of spherical roughness: 0.5um, (b) radius of spherical roughness: 1um, (c) radius of spherical roughness: 2um .....	94
Figure 5.8.(a) Measured and simulated response with surface roughness, (b) Optimized transmission and rejection characteristics of the channel filter in circuit level and full-wave EM simulation with the existence of surface roughness.....	95
Figure 5.8. Measured Surface roughness profile of the material .....	96
Figure 5.9. Transmission and reflection response of the channel filter .....	97
Figure 5.10. Computed and fitted insertion in passband of the filter. ....	98

# CHAPTER I

## INTRODUCTION

### 1.1. Satellite Payload System

Huge variety of communication systems such as satellite communication systems, wireless communication systems and radio transmission networks involve frequency multiplexer structures in order for the operation of combining and separating frequency bandwidths selectively. Especially in satellite communication systems, multiplexer structures are mostly employed in the uplink and downlink stage of the satellite payload, as illustrated in Figure 1.1. The payload system is basically composed of power amplifiers, low noise amplifiers, oscillators, frequency synthesizer, orthomode transducers, power dividers, circulators, couplers, filters and multiplexers [1].

One of the main subcomponents in the satellite payload is the input multiplexer (IMUX) stage in which separation of the input signals into frequency channels is accomplished just before amplification of each channel. Another important component, in which the combination of the amplified signals in each channel is done, is the output multiplexers (OMUX) for retransmission. Basically, a MUX is typically composed of channel filters and proper junction sections. Due to the fact that the waveguides are of low insertion loss, high power handling capability and high quality factor, they are usually employed in MUX and the channel filter. As far

as system requirements are concerned, there are different types of MUX configurations used in the payload network to fulfill them [2]. The channel filters utilized in IMUX and OMUX are preferred to have sharp selectivity in passband and high isolation in out of band. Moreover, total mass of them are meticulously considered since launch cost is directly proportional to overall weight of the satellite. Therefore, miniaturization and size reduction become extremely critical factor while conceiving the channel filter.

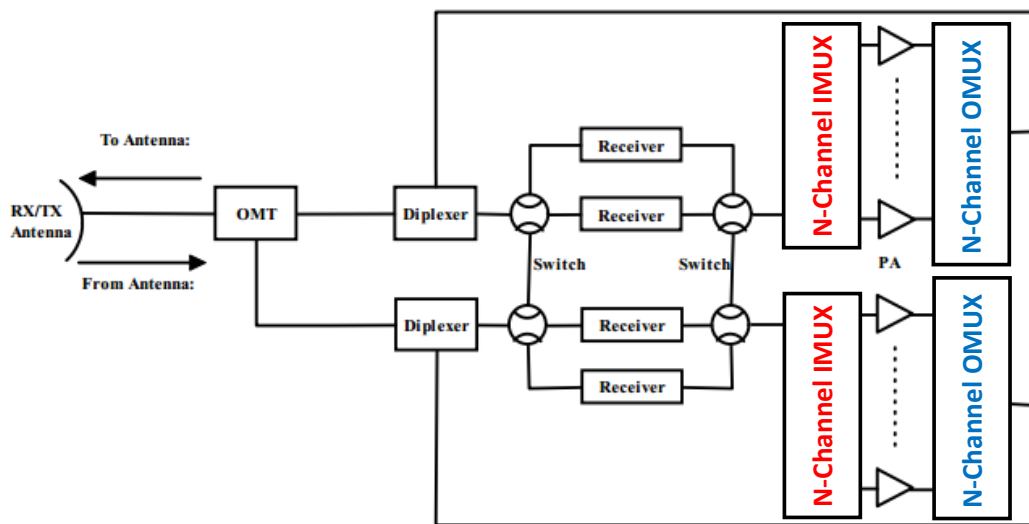


**Figure 1.1.** Layout of a satellite payload system [1].

## 1.2. Research Aim and Organization

This study focuses on design of miniaturized waveguide filter involving the impact of conductor surface roughness and investigates the various multiplexing techniques with respect to the field applications. In the scope of this thesis, the following research goals particularly elaborate on:

- A systematic design procedure for compact and narrowband waveguide filters are investigated. A novel approach to extract the circuit model of them is developed. And, hybrid optimization method is introduced for faster filter construction.
- Prior works on multiplexing techniques such as E-plane and H-plane are examined thoroughly and the most convenient one considering thesis frame work is determined as a result of deep evaluations.
- H-plane multiplexer structures are analyzed and a new design method based on simultaneous circuit and full-wave optimization is developed. Design procedure for multi-channel contiguous band multiplexers are explained stage by stage. As an illustration, three-channel and six-channel contiguous band waveguide multiplexers are conceived.
- In order to validate the proposed design method, a number of single channel filter are realized and experimental results are compared with the simulation results. Furthermore, TRL (Thru, Reflect, Line) measurement set-up is formed meticulously for the accurate testing and all performance parameters are measured.
- A thorough analysis on influence of the surface roughness effect on narrowband and highly-selective channel filter is accomplished a novel design procedure involving it is developed for high quality waveguide filters. The proposed procedure is validated with experimental consequences that are in well consistency with the expected results.
- Developing a systematic way for conceiving compact waveguide filter in the existence of the conductor surface roughness is one of the most critical achievements together with circuit modeling of the surface roughness and significant contribution to the literature. Hence, deteriorating impact of the surface roughness on waveguide implementations with high quality factor is

analyzed and desired filtering performance is obtained efficiently considering this impact by applying the proposed design steps.

The research goals mentioned above are pursued in this thesis comprising five chapters. Following this introduction chapter, a brief literature review on microwave waveguide filters and multiplexer structures are presented in Chapter 2. Similar works in the literature are assessed and compared with the proposed methodologies in the scope of this thesis. Chapter 3 provides all explanatory knowledge and details about the design of miniaturized waveguide filter together with numerical and analytical expectations. The validation of the design method is accomplished successfully by exemplifying specifically defined miniaturized waveguide filter structure. Chapter 4 presents the design procedure for the contiguous band six channel manifold-coupled multiplexer. Also, design trials using various approaches are simulated and the development of a novel design methodology is accomplished. Chapter 5 reports the detailed analysis surface roughness effect on waveguide filter response together with systematic design procedure involving this effect. Fabrication and measurement activities are also mentioned comprehensively with all computed and measured results. Chapter 6 mentions about the reached accomplishments in the scope of this thesis and future works.

### **1.3. Achievements and Accomplishments**

Following the completion of comprehensive full-wave and circuit level computations and analysis involving surface roughness phenomena on miniaturized and narrowband waveguide filter, next, a number of channel filter realization performed and the proposed technique was successfully validated as comparing the experimental results with expected ones.

In the scope of this thesis, accomplishments can be listed as follows:



- A novel approach to extract the circuit model of the narrowband waveguide filter is developed and systematic design procedure with hybrid optimization technique is introduced for faster filter construction.
- Surface roughness phenomena is investigated versatilely and effect of it on high quality factor waveguide filters are examined. It is concluded that surface roughness becomes a dominant limiting factor for miniaturized and highly-selective waveguide configurations and ought to be considered at design stage properly. Taking this phenomena into consideration, desired filtering response is achieved successfully after the modification of the design parameters such as resonator lengths, iris thicknesses and gap distances.
- Manifold-coupled multiplexer configurations are analyzed and detailed design study based on simultaneous circuit and full-wave optimization is completed. As an illustration, three-channel and six-channel contiguous band waveguide multiplexers are conceived and demonstrated.



## **CHAPTER II**

### **LITERATURE SURVEY**

#### **2.1.Literature Review on Microwave Waveguide Filters and Multiplexer Structures**

Multiplexer configurations and waveguide filter structures in the literature are analyzed thoroughly and a brief summary including basic theoretical background, similar implementations and qualitative comparison of the prior works with the proposed methodologies is presented in this section. Also, a review of the prior works on conductor surface roughness effect in microwave structures is presented.

##### **2.1.1 Multiplexer Configurations**

In microwave payloads of communication satellites filters are wanted to have high performance in order to reject undesired signals introducing noisy effects into the communication networks. Due to the nature of a satellite payload illustrated in Figure 2.1, where captured signal coming from earth are drastically weak whilst back-transmitted signals are of high power, the filters are required to be highly frequency selective. Especially, filters that make up IMUX, OMUX employed in satellites are to provide low insertion loss, high frequency selectivity and spurious free wideband. Furthermore, passband flatness is also significant so as to reduce deterioration amount of the channels laying at the edges of reception band [3].

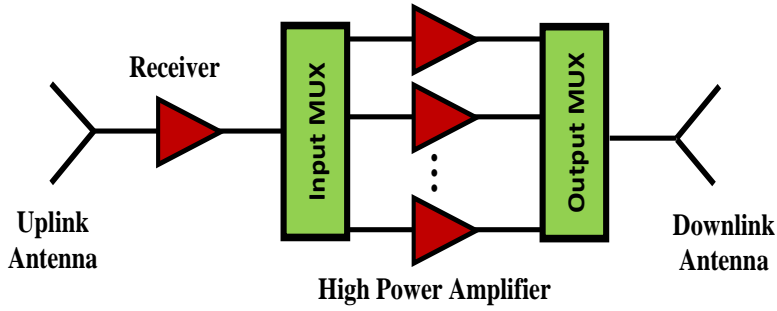


**Figure 2.1.** Basic block diagram of a satellite payload.

In the implementation of the multiplexing configurations for satellite communications, mainly four various types of MUX networks are encountered in the literature: hybrid-coupled multiplexers, directional filter multiplexers, circulator-coupled multiplexer, and manifold-coupled multiplexers [4].

Hybrid-coupled MUX network, shown in Figure 2.2, are composed of two exactly the same channel filters and  $90^\circ$  hybrids. The directionality is one of the advantages of it, which reduces channel filter interactions with each other. Another advantage is that the design of filter may be casual by utilizing this sort of MUX in high-power implementations since each filter is experienced half of input power [4]. However, it is disadvantageous of larger sizes due to the requirement of two filters and hybrids per channel. Also, phase deviations between the each filter paths deteriorate the MUX performance. Therefore, the structure must be fabricated by considering minimum phase deviation [4].

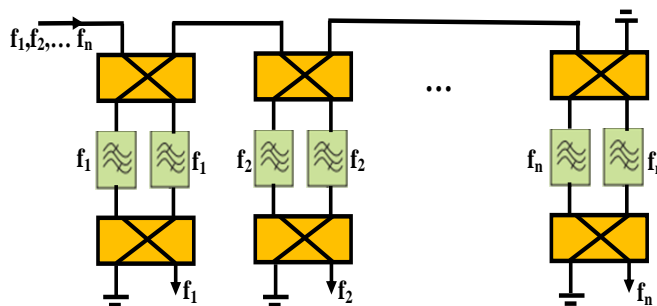


**Figure 2.2.** Schematic of Hybrid-coupled multiplexer.

Directional filter approach illustrated in Figure 2.3 is composed of series-connected directional filters which have four ports and one of ports is terminated in a load and the others act like a circulator [4]. Power entering one port exiting at the second port with bandpass response whilst power reflected from filter flows at the third port. Directional filter multiplexing approach has the same advantages whereas it is of restricted usage only in narrow-band applications.

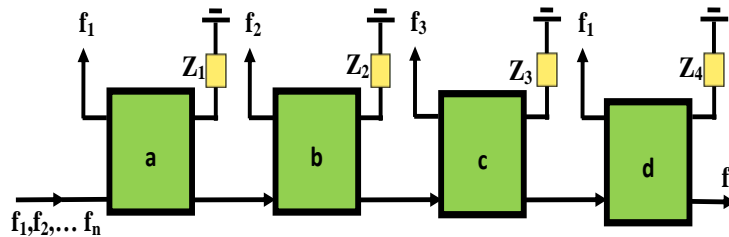


**Figure 2.3.** Directional filter multiplexer.

Circulator-coupled multiplexer has a channel-dropping circulator and one filter as illustrated in Figure 2.4. The unidirectionality of the circulator serves the similar advantages as the hybrid-coupled multiplexing [4]. But, insertion loss of the channels is high due to additional loss of the circulator.

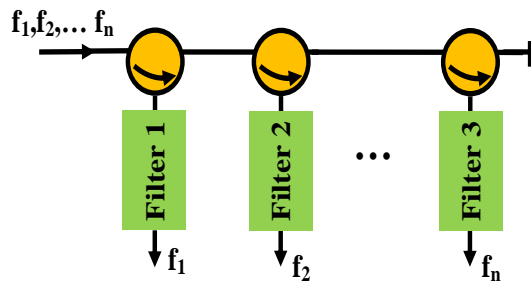


**Figure 2.4.** Circulator-coupled multiplexer.

Considering miniaturization, compactness and insertion loss level, the manifold-coupled multiplexer, shown in Figure 2.5 is the most preferred structure in satellite payloads. It provides miniaturized and lowest-insertion loss operation and also has

the capability of optimum performance for amplitude and group delay response [4]. On the other hand, main disadvantages of this approach are complexity in design, high sensitivity and lack of amenability to adaptable frequency allocation [4]. If any changes are desired in channel frequency or allocation, it is required to design a new multiplexer. All the channel filters are to be present at the same time so that interaction effects between channels can be made up for at the design stage [2].

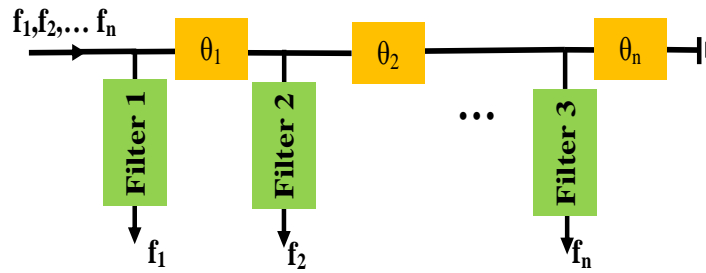


**Figure 2.5.** Manifold-coupled multiplexer.

There are mainly three types of configurations for the manifold-coupled multiplexers: comb, herringbone and directly filter feeding into manifold as illustrated in Figure 2.6.

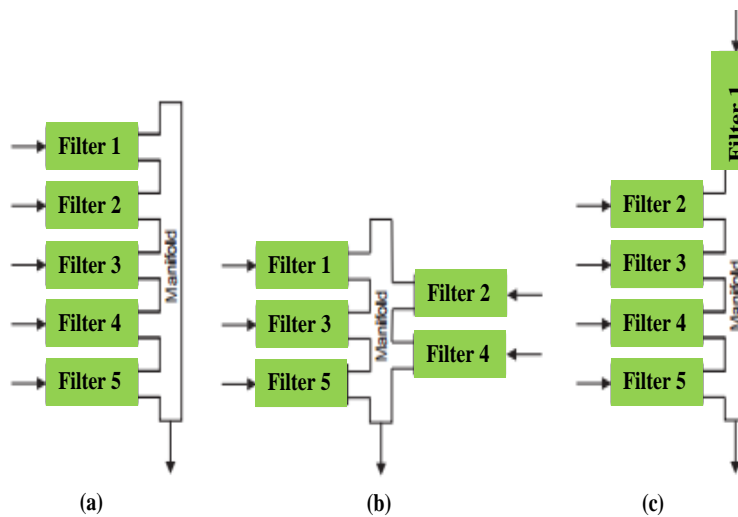


**Figure 2.6.** Manifold MUX configurations: (a) comb, (b) herringbone, (c) one filter feeding.

### 2.1.2. Review of the Prior Studies on Contiguous-Channel Waveguide Multiplexers

General multiplexer theory is presented in [5] as an earlier study in 1979. Related formulations and derivations for multiplexers are given thoroughly. Design methodology and equivalent circuit representation of waveguide contiguous-channel frequency multiplexer are investigated and introduced in [6]. The proposed one is three-channel multiplexer including ridge-waveguide channel filters and manifold coupling networks and port coupling network, as shown in Figure 2.7. The operational frequency band of this multiplexer is 4-6.25 GHz.

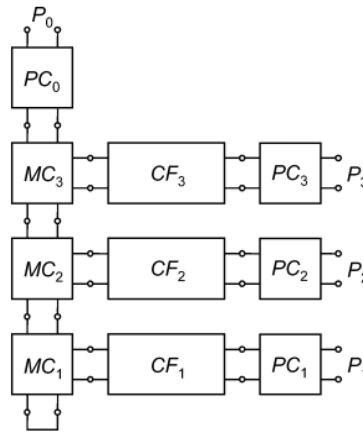


**Figure 2.7.** Block diagram of three-channel multiplexer proposed in [6].

Cross sectional view of the three-channel multiplexer schematically shown in Figure 2.7 is illustrated in Figure 2.8. It comprises vertically stacked fourth-order channel filters which consist of five evanescent mode sections and four ridge waveguide sections that are exploited to couple adjacent ridge-waveguide resonator sections with first and last resonator of the channel filters [6]. Equivalent circuit representation of each stage is introduced, pertinent parameters are also derived.

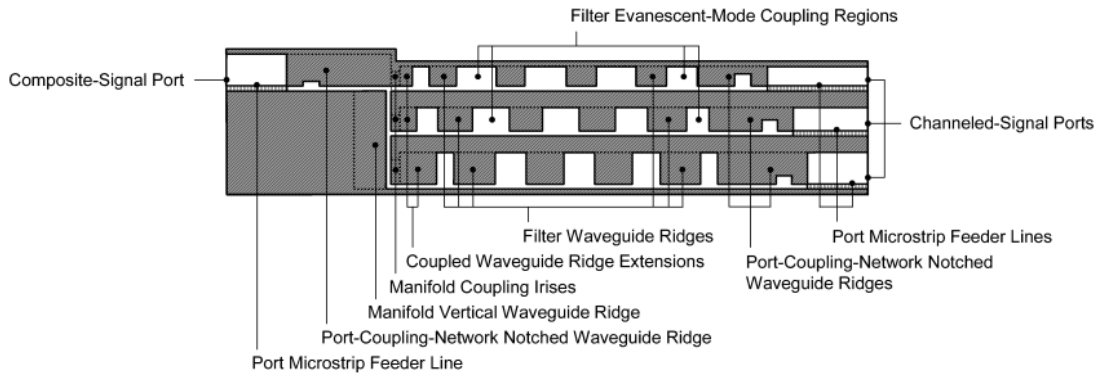


**Figure 2.8.** Cross sectional view of three-channel multiplexer proposed in [6].

The channel filters used in this multiplexer structurally akin to ridge-waveguide filters introduced in [7] and [8] which are the previous manuscripts of the same author. Dielectric-filled and five-pole ridge waveguide bandpass filter is proposed in [7], as illustrated in Figure 2.9. High-dielectric constant materials are exploited at the resonator ridge's high-field gap regions so as to suitably enlarge the ridge-gap spacing for easier realization and also adjust the bandwidth of the ridge waveguide at 1-1.45 GHz frequency band [7]. Moreover, related parameters of equivalent circuit model for ridge and evanescent mode waveguide sections are derived and formulated. Four-pole and air-filled version of that filter is employed in this three-channel multiplexer structure by scaling the pertinent design parameters properly.



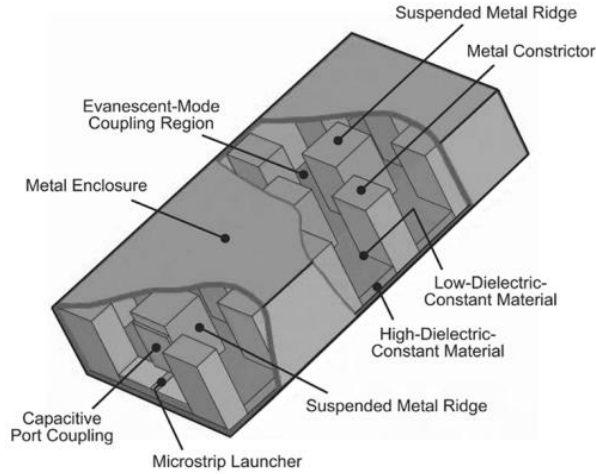


**Figure 2.9.** Representation of a dielectric filled cavity bandpass filter in [7].

In [8], the 6-8.6 GHz five pole ridge waveguide filter, as shown in Figure 2.10, derived from 1-1.45 GHz bandpass filter is described and also parameter analysis are presented for 8.6-11 GHz and 11-18 GHz frequency band operation.

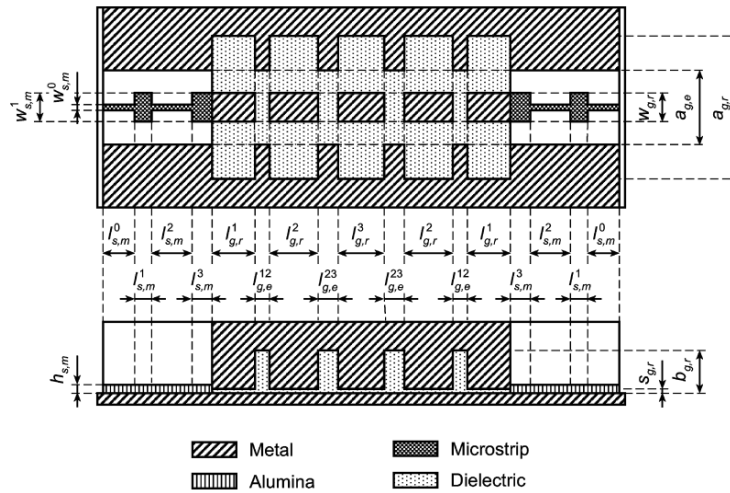


**Figure 2.10.** Horizontal and vertical cross-sectional view of 6-8.6 GHz cavity filter in [8].

In [9], reactive load-based manifold design procedure is introduced and five-channel output multiplexer is conceived as an illustration in X-band using proposed method. In order to determine manifold lengths, amplitude and the phase variation of channel filter's input reflection coefficient are modeled as a polynomial and manifold structure is determined using that fictitious reactive model of channel filters instead of full-wave ones for initial lengths of manifold. Then, initial lengths are optimized and full-wave configuration of the multiplexer is formed. In [10], computer-aided design steps of multiplexer are explained without tuning elements. A hybrid optimization method is proposed for the seven-channel multiplexer in X-band. Both parameters in circuit and the full-wave model are optimized, respectively and then hybrid model is formed for the final optimization of the multiplexer's parameters as shown in Figure 2.11.

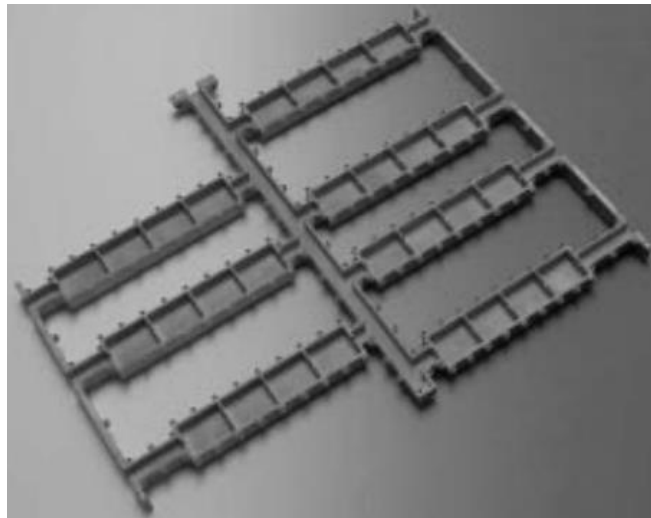


**Figure 2.11.** Seven-channel manifold multiplexer in [10].

In [11], manifold-coupled triplexer is design by connecting filters to the manifold sequentially and parameters optimization is reiterated after each connection. It is also proposed a detailed flowchart including the design steps of manifold and multiplexer. In order to determine the lengths of the manifold junctions accurately, channel filters are connected to manifold body one by one and scattering parameters of network are recalculated after the connection of the each section. At final stage,

convenient manifold iris sizes and junction lengths are obtained at the end of numerical iteration cycles. Furthermore, the information about the C-Band quadruplexer is presented for the passive intermodulation measurements.

The authors of [12] introduce a design procedure for the manifold multiplexers including dual mode circular waveguide filters. Low-order multimode model is exploited for the construction of the entire multiplexer. Distributed model of the circular waveguide filters with coupled irises are used for the optimization of the manifold lengths. Ten-channel circular waveguide multiplexer, shown in Figure 2.12 is conceived together with the formulations for the low-order model and extraction of multiplexer dimensions.

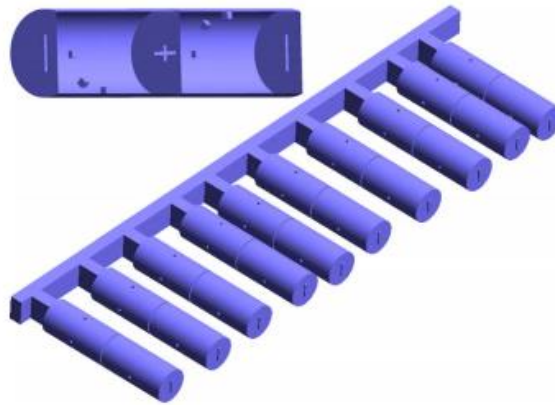


**Figure 2.12.** Ten-channel manifold multiplexer with circular waveguides in [12].

In [13], six-channel multiplexers with rectangular waveguides using low-order model is mentioned by giving related geometrical details. Different multiplexer topologies are carried out and coupling matrix for multiplexer configurations is calculated. Furthermore, channel filters are analyzed by separating coupled resonator sections and filtering mechanism is explained with produced transmission zeros at finite frequencies, as shown in Figure 2.13.

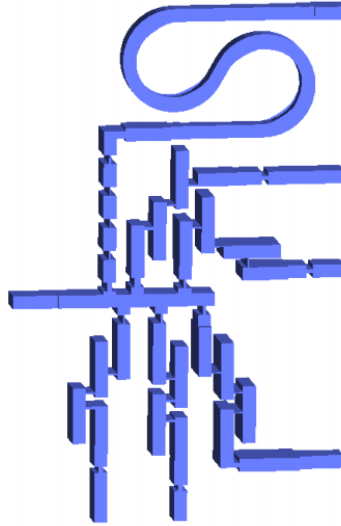


**Figure 2.13.** Six-channel manifold multiplexer with rectangular waveguides in [13].

In [14], design technique for diplexer with WR112 rectangular waveguide is presented. Seventh-order waveguide filters are employed as channel filters. Also, T-junction and manifold distances are determined by virtue of the full-wave and circuit-based optimization.

In [15], elliptic-response four-channel rectangular waveguide multiplexer covering from 11.9 GHz to 12.25 GHz is designed starting from the synthesis of channel filters based on Cauer ladder method. Mode matching response of the multiplexer is obtained by taking the circuit response of that as reference and geometrical dimensions are extracted for standard WR75.

In [16], detailed information about the construction of X-band three-channel manifold multiplexer with dual-mode rectangular waveguide filters is mentioned. Coupling matrix representation method is carried out for the synthesis of the E-plane and H-plane multiplexer configuration. Considering reactive loading effect of H-plane T-junctions, junction distances to the channel filter are revised by observing the amplitude and phase deviation of the scattering parameters.

In [17], X-band diplexer is designed by using metal-inserted H-plane T junction. Impedance inverter equivalent for the WR-75 channel filters are exploited and a new

method is proposed based on considering common junctions of manifold body as a part of channel filters.

In [18], design procedure for the ten-channel output multiplexer with dielectric resonator channel filters are mentioned. Space-mapping formulations are derived for the evaluation of the geometrical dimensions of the manifold and channels. Coarse model of the multiplexer is firstly created, and then space-mapping optimization is applied for each channel. Finally, the geometry of the multiplexer are determined after several iterations via extracted coupling matrix of the channels. Similarly, Ku band triplexer is presented in [19] on the basis of coupling matrix extraction with derivatives of the scattering matrix.

In [20], a method for the synthesis of the Chebyshev filters with complex load is mentioned. Coaxial and waveguide diplexer applications using synthesized filters is presented by identifying the root locations of filtering function on complex  $s$ -plane and diplexer's dimensions are found iteratively at the end of the evaluation of the coupling mechanism of the entire multiplexer.

In [21], furcated-type E-plane triplexer is proposed together with iris-coupled cavity filters. Main idea of that method is to conceive a three-way E-plane power divider and connect the channel filters to the end of the divider. In order to design the power divider and multiplexer structure, numerical iteration and mode matching method are applied for the optimum response. Furthermore, design process of a similar E-plane tri-furcation triplexer is presented in [22], which is companion work of the same author.

The authors of [23] focus on the field theory of the  $n$ -furcation waveguide multiplexer by deriving the electric and magnetic field expressions for an arbitrary place at the multiplexer. Ku-band diplexers including E-plane metal-inserted channel filters are conceived by calculating modal scattering matrices of each section and manifold lengths are optimized at the end of the numerical iteration of the modal  $S$ -matrix.

In [24], a new formulation is suggested for the optimization of T-junction manifold multiplexers. Design steps based on the manipulations of the scattering matrix formulations of the WR90 diplexer employing E-plane filters are presented thoroughly. Positions of the channel filters in manifold structure are found with the exploitation of the proposed formulation.

In [25], computer-aided design procedure of the contiguous band seven-channel multiplexer employing Y-junctions is explained. Once the initial dimensions are found, final multiplexer structure is obtained by applying “the adjoint network method” and full-wave optimization. Similarly, X-band waveguide diplexer with Y-junctions and iris-coupled channel filters are presented in [26]. Also, dimensional synthesis procedure of single iris in waveguide filters is mentioned step by step.

In [27], an optimization and the design method is proposed for the large-scale multiplexers in X-band. Starting from the derivation of [ABCD] matrix, distributed model for the channel filters is extracted. Each resonator of the dual-mode elliptic filter is evaluated individually. Mode-matching technique and circuit model are used for the design of the multiplexer.

In [28], the design of multiplexing network based on the influence of the E-plane T-junction on group delay of the multiplexer is presented. Considering that “the channel filter is of short-circuited character at out of band, channel filter input ports of the manifold body are short-circuited and peak value of group delay at common port is adjusted at the center frequency of each band. An illustration of the two-channel multiplexer is depicted with group delay formulations. Also, H-plane multiplexer is designed by applying the same procedure in [29].

Artificial neural network method is applied for the design of iris-coupled circular multiplexer in [30]. Coarse and fine model of the multiplexer are evaluated to obtain desired transmission-rejection response and space-mapping algorithm based on the extraction of the coupling matrix is carried out. In order to compensate the spurious modes, the employment of the artificial neural network method is explained thoroughly.

## **2.2. Microwave Waveguide Filters**

Cavity filters are commonly employed in satellite communications since they are of the ability to provide high quality factors, high frequency selective filter response with low insertion losses and handle the high power requirements [31]. Several types of cavity filters are listed as: evanescent-mode waveguide filters, coupled cavity filters, dielectric resonator filters and E-plane filters [31]. Theory and the implementation of these filter types are briefly mentioned in this section.

### **2.2.1. Evanescent-Mode Waveguide Filters**

Satellite communication networks demand filtering and multiplexing structures which are of high performance to efficiently allocate the swarmed frequency spectrum [32]. The most commonly sought features for filters embedded in the input and output multiplexers are lower insertion loss, high power handling capability, high frequency selectivity and compact size. In addition to these essential requirements, spurious free stopband is also important for wide spectrum applications. So, an appropriate candidate for trading-off all the required features is the evanescent mode technology [32]. Conventional waveguides can be employed below cut off frequency of its dominant mode so that miniaturized and compact waveguide filters with desired performances are realized. For below cut off operations, propagation constant becomes imaginary and, the waves are deteriorated exponentially in all modes with regard to the length passed into the waveguide and so it is called Evanescent Mode Waveguide, as shown in Figure 2.14 [33]. On the other hand, the attenuation of the evanescent waves can be explained as like attenuation in stopbands of lossless filter components. However, the waveguide are of purely imaginary characteristic impedance in the cutoff operation and behaves as a reactive element instead of the propagating one [33]. This reactive characteristic impedance is the key factor for the realization of various filters.

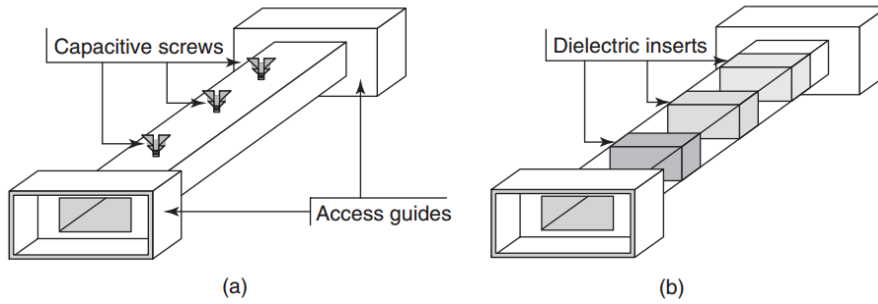


**Figure 2.14.** Evanescent mode waveguide filters (a) with screws, (b) with dielectrics [31].

At below cut off operations of a waveguide, it has the features of an inductive component. In order to conceive evanescent mode waveguide bandpass filter, appropriately designed capacitive elements with metal posts, irises and tuning capacitive screws or inserting dielectrics are needed [34]. Definition of the filtering characteristics is only valid for the fundamental mode due to the assumption that all higher order modes will vanish between capacitive elements. Transmission line and lumped circuit equivalent of the evanescent mode waveguide are first introduced by Craven and Mok [35] in 1971 and an evanescent mode waveguide filter with capacitive screws, similar with Figure 2.14.a, is proposed. Under the assumption that evanescent  $TE_{10}$  mode is existing solely in the waveguide [35], the simple transmission line equivalent of the evanescent mode waveguide is shown in Figure 2.15. For TE evanescent modes may be used as equivalent circuit of the waveguide section. The lumped element approximations become closer when operation frequency is below the cut of frequency extremely [36].



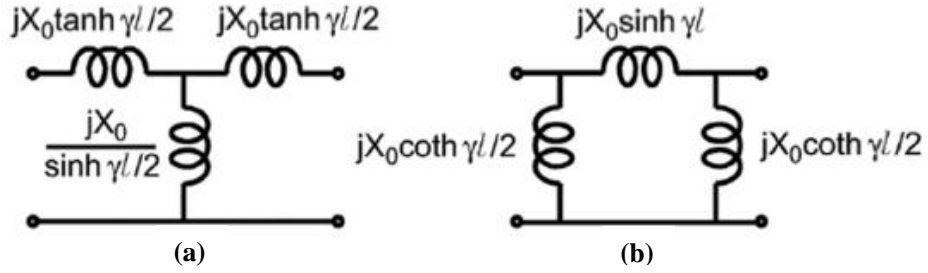


**Figure 2.15.** (a) T, (b)  $\pi$  equivalent circuit model of evanescent mode WG for  $l$  length [35].

It is possible to obtain such a lumped circuit equivalent as shown in Figure 2.16 by manipulating the  $\pi$  equivalent circuit properly to form an admittance inverter [35]-[36]. By inserting shunt inductive elements in Figure 2.16, an admittance inverter is formed to obtain shunt-connected filter configuration.

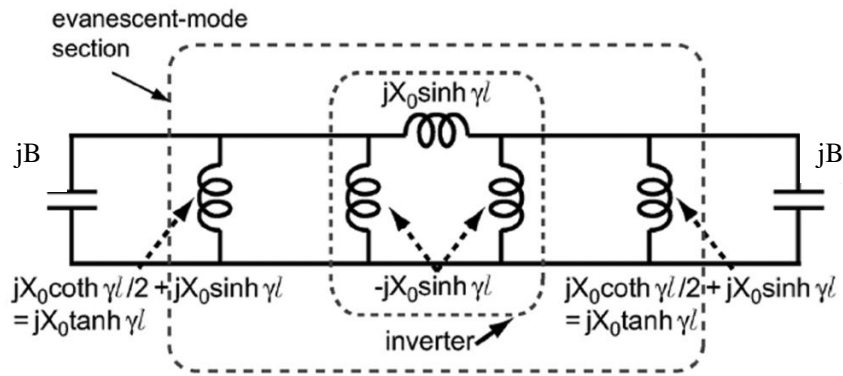


**Figure 2.16.** Lumped circuit model for Evanescent-mode WG filter in [35].

Evanescent mode WG filter with dielectric inserts instead of the capacitive screws is proposed in [37]. The filter is composed of a series of resonators coupled through evanescent-mode waveguide sections. This design method allows significant restrictions on lengths and exact positions of the dielectric portions and tunability property [37]. Furthermore, ridge waveguides are mostly preferred in evanescent mode filter applications since they are more advantageous compared to rectangular waveguide as far as fundamental-mode operation bandwidth, cut off frequency; wave impedance and compactness of the filter are concerned. Wider fundamental

mode operation bandwidth can be easily obtained with ridge waveguides. It is possible to have smaller cross-sectioned and more compact ridge waveguide filters due to the lower fundamental mode cut off frequency. Transition from ridge waveguide to microstrip or strip lines are much easier due to the fact that it is of the low wave impedance [38]. Also, the achievement of wide spurious-free out-of-band response may be obtained by using various ridge configurations. The most commonly used single and double ridge wave guides with E-field distributions are depicted in Figure 2.17.

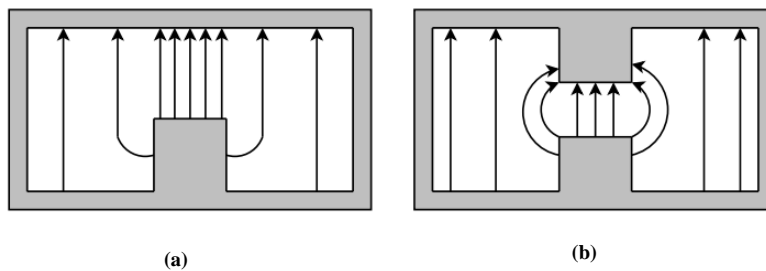


**Figure 2.17.** Electric field distribution in (a) single ridge (b) double ridge [39].

At the gap region, the strong E-field is observed and charges are accumulated between two sides of the gap it is possible to model this structure as the combination of two shunt capacitors and two characteristic admittances, where  $Y_{02}$  is in the gap and  $Y_{01}$  outside gap is as shown in Figure 2.18.

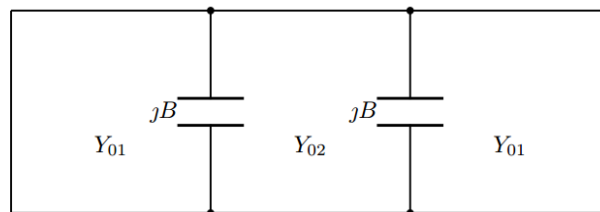


**Figure 2.18.** Equivalent circuit model for rectangular ridge waveguide [39].

### 2.2.2. Coupled Cavity Filters

Coupled cavity filters are based on the resonance of several degenerated modes inside the same cavity. One of the earliest study on direct-coupled filters is presented by Cohn in [40]. The first realization of this concept appears in [41]. Bimodal circular cavities are commonly used in implementation of these filters as illustrated in Figure 2.19. The coupling coefficients and overall response of the filter can be tuned by virtue of tuning screws, circular coupling irises [41].

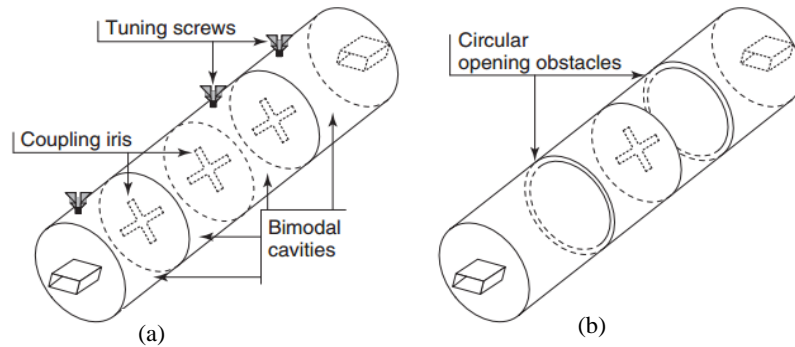


**Figure 2.19.** Circular cavity filters (a) with tuning screws and coupling iris (b) with opening obstacles [31].

Also, the rectangular cavities are employed in the implementation of these filters. Small evanescent mode waveguide sections are used to fine tune the coupling factor between the cavities as shown in Figure 2.20. It is possible to obtain realizable coupling factor by adjusting the dimensions of evanescent-mode waveguide. In order to have the same resonant frequency for the fundamental mode and another mode the cavity dimensions must be increased. Instead of tuning screws, coupling tuning can be achieved with small cuts in the rectangular waveguide. The inductive-type irises are used to keep constant the height of the cavity [42].

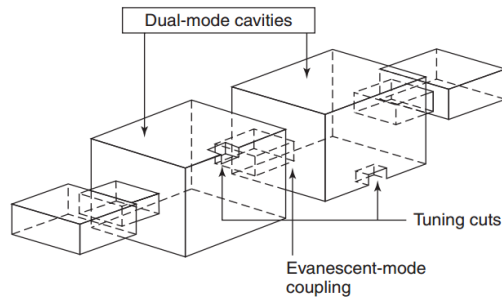


**Figure 2.20.** Bimodal rectangular cavities with small cuts [31].

The design of the dual-mode filter with inductive irises and tuning screws is presented and modal combinations in rectangular waveguide resonator is formulated in [43]. Effects of changing the width-length ratio of the resonator on the position of the transmission zeros are presented with fourth-order dual mode filter in Ku band. Similarly, all-inductive dual-mode filter, shown in Figure 2.21, is conceived in [44] by determining the coupling matrix of the filter and evaluating the polynomial expression of the scattering parameters.

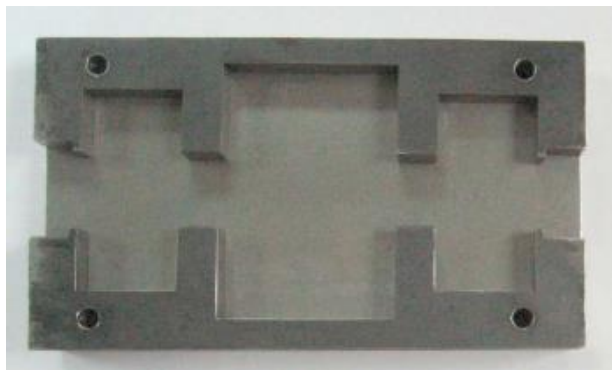


**Figure 2.21.** Dual-mode band-pass filter in [44].

The author of [45] and [46] focus on the synthesis and design procedure for the wideband inductive-coupled waveguide filters. Prototype synthesis is firstly

accomplished with extracting the impedance inverter model of the filter and then physical lengths of the filter is iteratively optimized by means of the CAD tools and space-mapping methods.

In [47], multimode waveguide filter is synthesized and a synthesis procedure is proposed based on using thick irises. The way of the construction of the multimode network model of the waveguide filter is mentioned with the analysis of the quality factor of the filter.

In [48], circuit equivalent models for the discontinuities such as inductive and capacitive irises placed in the rectangular waveguide are presented with a framework for the coupled-cavity filters. Impedance inverters are expressed in terms the scattering parameters and direct-coupled filters are designed with quarter and half-wave resonators.

In [49], dual-mode iris-coupled circular waveguide filters and parallel comb-line bandpass filters are investigated and equivalent circuit models for them are proposed with circuit parameter expressions and derivation of the related formulae .

In [50], coupled irises in cavity filter are characterized as L-C resonators. Polynomial expressions for the L-C value are established as polynomials. Iris-coupled filters are designed after the optimization of the circuit parameters using numerical an EM optimization tools.

### **2.2.3. Dielectric Resonator Filters**

The dielectric resonator filters are based on the cylindrical or rectangular resonators. The dielectric resonators are put inside the cavity to prevent the radiation losses. Following  $TE_{0n}$  mode,  $TM_{0m}$  mode or a hybrid  $TEM_{nm}$  mode can be excited at this stage. The fundamental mode relies on the diameter and resonator height ratio. Different placements of the dielectric resonators inside the cavity are illustrated in Figure 2.22. The cavity is circular or rectangular. Inter-resonator couplings are

determined by approximate methods based on magnetic moments proposed in [51]. Traditional iris and evanescent mode waveguide sections are also used to adjust coupling level between cavities. However, large temperature variations within resonators are taken place due to the fact that the dielectric resonator is of low thermal conductivity and this causes degradation in filter response. To solve this problem, metallic planes are inserted the dielectrics or resonators with complex geometry are employed such as octagonal resonators [52]. Also, it is difficult to stay the dielectric resonator at intended places, especially for satellite applications, where vibrations occur [52].

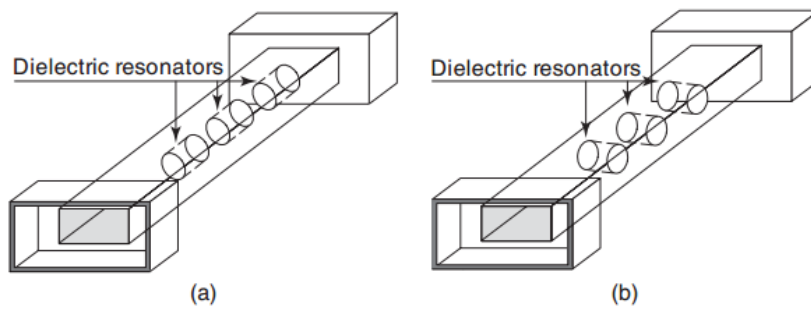


**Figure 2.22.** Dielectric resonator filters (a) axially positioned (b) laterally positioned resonators [31].

In [53], investigations on spurious mode reduction in dielectric resonators are presented. The performance of the dielectric filters with rectangular, circular and drilled circular resonators are compared with each other in terms of spurious rejection.

In [54], coupling mechanism for the ring dielectric resonator loaded six-pole cavity filter is focused and coupling matrix are obtained by considering the mixed mode analysis of the dielectric resonator loaded filters using mode matching method.

### 2.2.4. E-Plane Filters

E-plane filters are composed of dielectric plates with mostly metallized surfaces put in the plane of waveguide electric field as shown in Figure 2.23.a. To obtain desired bandpass filtering response, metallization is employed to form coupled half-wavelength resonators as shown in Figure 2.23.b. Also, the dielectric substrate can be removed to get higher Q factor of the filter, then the filter consists of a metallic sheet put between the two parts of the waveguide [31], as shown in Figure 2.24.a. By placing two metallic sheets in parallel as shown in Figure 2.24.b, the stopband rejection can be improved. By changing the distance between metallic sheets and waveguide walls, the inductive coupling is provided.

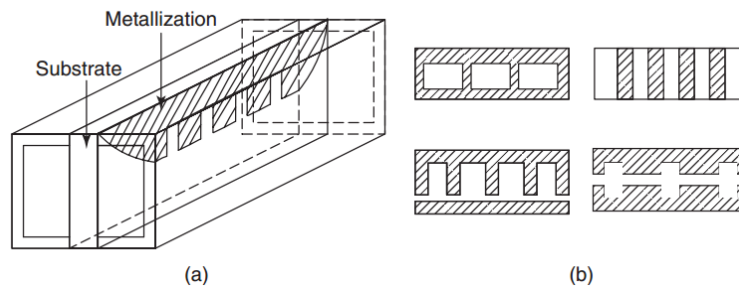


**Figure 2.23.** E-plane filter (a) filter structure (b) metallization types [31].

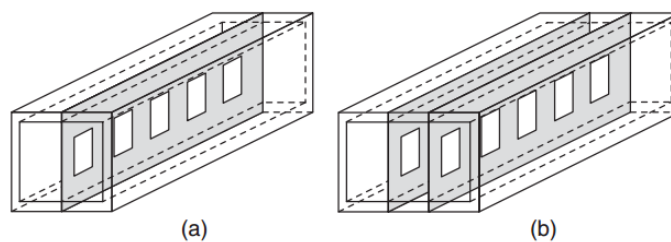


**Figure 2.24.** E-plane filters with metallic inserts (a) one insert (b) two parallel inserts [31].

Also, it possible to control the filter's electrical response by patterning the E-plane metal fins using this filtering technology. Standard E-plane rectangular waveguide filters have narrow stopband characteristic with moderate attenuation. To cope with such drawbacks, instead of increasing the number of the resonators that is unsuitable for satellite applications due to bulkiness, periodic E-plane filters are designed with reactive-loaded rectangular waveguide resonator by means of appropriate obstacles in form of ridges periodically [55], as shown in Figure 2.25.

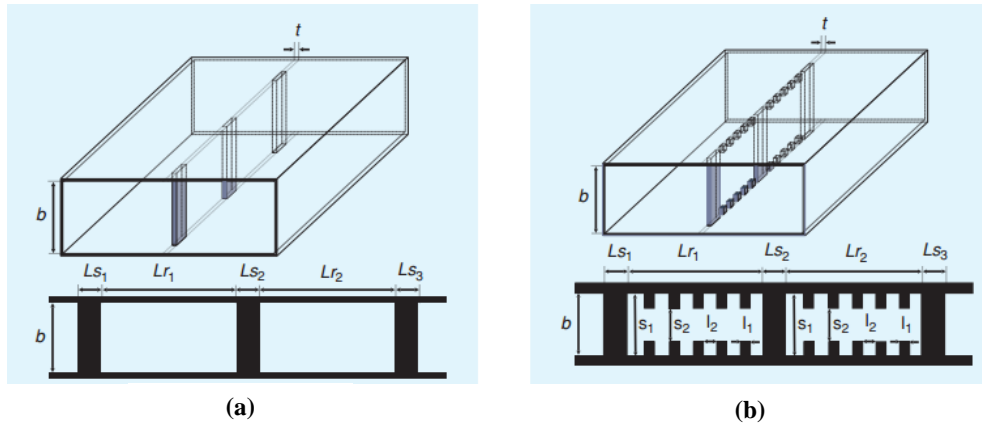


**Figure 2.25.**Periodically loaded E-plane waveguide filters [55].

In [56] and [57], loaded and unloaded quality factor of the E-plane filter are calculated for the various shape of the inserted metal and field distribution on metal is analyzed via EM simulation tools. Also, size reduction effect of the periodically loaded E-plane filter as shown in Figure 2.26 is investigated and effect of periodicity on filter characteristic is searched. In a similar work, the authors of [38] focus on the length reduction of the filter using ridged waveguide sections.

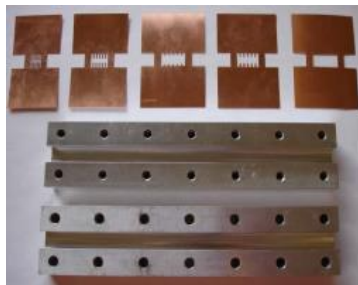


**Figure 2.26.** Fabricated E-plane resonator in [56].



Size reduction and the miniaturization of the multiplexer including cavity filters are of great importance due to the fact that the launch cost of a satellite is straightforwardly corresponding the aggregate mass of the payload system [3]. Also, being easy to integrate it to the system is another crucial factor in terms of compactness. However, works on the miniaturization of the WG filters are rarely encountered in the literature since standard WGs are used for the filter designs. Micromachining techniques are mostly applied for the fabrication of the size-reduced component.

The author of [58] conceives a novel X-band cavity filter by carrying out micromachining process. It consists of the vertically and horizontally integrated cavities with shielding silicon wafers. Coupling slots are exploited to interconnect cavity resonators together with all necessary transitions. Similarly, K-band linear phase cavity filter is designed using KOH wet etching with silicon wafer in [59]. Length of the coupling slots are determined by using the fourth order polynomials and EM simulation tools. Coupling coefficients of two cross-coupled cavities are extracted.

In [60], Ka-band high Q vertically integrated cavity filter is designed as shown in Figure 2.27 using micromachined coupling layers. Temperature sensitivity of the filter is investigated using Monte Carlo Analysis. Coupling slots and wafer dimensions are calculated with numerical calculations and simulations.

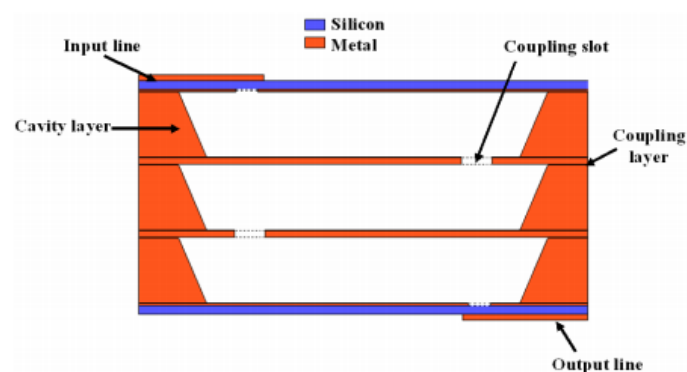


**Figure 2.27.** Micromachined cavity filter in [60].

In [61], design procedure of quartz-loaded waveguide filter in X-band illustrated in Figure 2.28 is presented with coupling-matrix theory. Inter-resonator coupling coefficients are extracted and iris aperture sizes are found via coupling matrix calculation. Also, a new figure of merit is introduced for the comparison of the compactness and performance of the other filters.

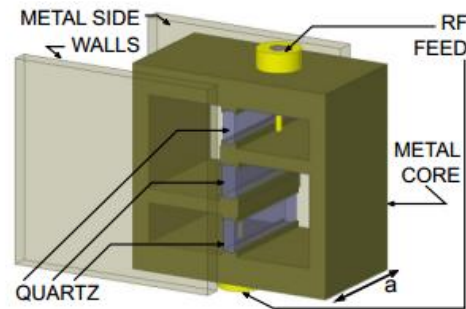


**Figure 2.28.** Quartz-loaded WG filter proposed in [61].

After delving prior works and implementations in the literature, a comparison between the highlighted especially similar ones and this study in terms of some distinctive features such as quality factor will give an idea about the position and contribution of this thesis to the literature.

Iris-coupled circular waveguide filter in [41] is of 0.9 % fractional bandwidth and its Q factor is 110. Correlation between higher modes ought to be well-adjusted to fulfill the specifications. A narrowband iris-coupled circular waveguide filter in X-band whose Q factor is 388 and fractional bandwidth is 0.25% is implemented in [13].

Dual-mode inductively coupled waveguide filter is designed in [16] for the contiguous channel multiplexer in X-band. Fractional bandwidth is 0.3% and the quality factor is 305. Since dual-mode operation is used, the filter structure and multiplexer are far from compactness.

The loaded quality factor of the dual mode waveguide filter implemented with standard WR75 in [43] is about 74, fractional bandwidth is 1.35 % for the operation. Interactions between modes in cavity are used for controlling the filter response. So, the filter is composed of different-sized resonator sections and this increases the bulkiness of the structure. Inductively coupled waveguide filter implemented with standard WR75 in [46] is of single mode operation and 2 % fractional bandwidth. The Q factor of it is 45. As a wideband filtering example of the all-inductive waveguide filter, the loaded quality factor of the filter is 5 and fractional bandwidth is 20% in [45].

In [56], narrowband rectangular waveguide filters with periodically loaded E-plane metal-fins are assessed in terms of the loaded and unloaded quality factor. Loaded Q factor is varied from 70 to 140 by changing the meandered distance of the metal fins. Also, effect of the periodically loading on size reduction is analyzed. But, the proposed filter structure is very difficult to implement in multiplexers due to the lack of adjustability and tunability.

Considering the direct coupled filters, whose quality factor is in the range of 360-370 and fractional bandwidth is 0.3 %, are achieved to conceive in this study quickly and practically, very stringent filter specifications are rarely seen in the literature. Circular waveguides are mostly used to meet those requirements. But, they are of complicated design procedure and bulky structure.

In [14], EM cosimulation technique is proposed for the diplexer together with waveguide filter design. The proposed method in this thesis is of distinctively advantageous sides whereas design approach for waveguide filter is similar. Parameterized full-wave model for inductive septum coupling generated by EM solver is used for the characterization of the waveguide filter for wideband applications. Resonator lengths are equally taken as half wavelength. This brings a geometrical restriction and a handicap for the length reduction purposes and compactness. Considering the proposed one, resonator lengths may be reduced by properly adjusting the width and the gap distance of inductive iris. Moreover,

lumped-element model of the inductive iris is constructed for the whole structure and parameters are achieved at the end of the fast optimization. It is valid for the narrowband applications.

In [45], wideband circuit prototype is presented and related derivations and formulations for the inductive waveguide filters are thoroughly explained. Circuit prototype is composed of impedance inverters and frequency dependent transmission lines. In order to achieve desired filtering function, all inverter constants and some self-defined parameters ought to be calculated and optimized iteratively. This method is more convenient for the wideband applications. In our study, it is possible to achieve desired filter response without any need of iteration cycle. Also, inverter constants are calculated for direct extraction of the initial dimensions of the irises and resonators by exploiting the analytical design curves in [62]. Sole important parameter for the characterization is the variation in phase and amplitude of the  $S_{21}$ . So, the proposed method provides an opportunity to conceive the miniaturized and inductively-coupled waveguide filter with fast local optimization using computer-aided design tools. There is no restriction on width, gap distance of the iris and resonator lengths. Hence, compact and narrowband waveguide filters may be designed quickly.

### **2.3. Review of the Prior Studies on Influence of Conductor Surface Roughness on Microwave Structures**

Conductor surface roughness effect may become a significant limiting phenomenon and have deteriorating impact on power absorption and insertion loss features of the radio-frequency (RF) structures such as waveguides, microstrip and coaxial lines. It also brings out major limitations on slow wave structures and RF cavities [63]. Assessment of the power absorption due to the cylindrical defects and bumps on flat surface is provided in [63]. Scattered fields from cylindrical bumps and trenches on flat conductor are computed employing higher order integral solutions. Enhancements factor for power absorption to account for the relation between power

absorption and conductor surface roughness was firstly proposed by Morgan in [64]. It can be defined as the ratio of the power dissipation due to eddy currents in rough conductor and power dissipation in smooth conductor.

Power absorption analysis for the conductor roughness effect is based on the representation of the surface roughness as periodic structures such as periodic grooves, hemispheres and snowballs. Power absorption derivation is only valid for prescribed shape of the roughness [65]. Later, Hammerstad-Jensen modified the Morgan's formula by considering only effect of grooves on power absorption as shown in Figure 2.29

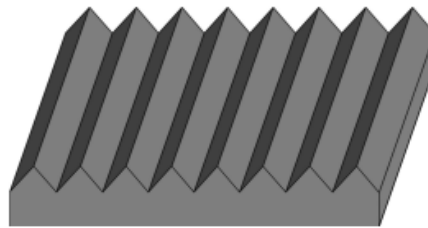


**Figure 2.29.** Morgan-Jensen model [65].

In [66], conductor surface roughness is modeled as hemispherical discontinuity for transmission lines. A transmission line modeling methodology based on the three-dimensional hemispherical approach for accurate prediction of the data response is proposed. Also, Lukic and Filipovic utilized 3-D modeling approach by simulating cubic and pyramidal-shaped roughness profiles and derived analytical equations for correction factor in [67]. Authors of [68] compares the additional power dissipation in conductor because of the surface roughness with smooth conductor and predicts the power loss in conductor using generalized impedance boundary condition. They concludes that conductor surface roughness increases power dissipation drastically and it ought to be considered meticulously for more accurate design. Also, frequency-dependent ohmic losses of interconnects in conductor due to the surface roughness is investigated in [69] and interaction of the incident field with corrugated conductor surface is analyzed by exploiting asymptotic approach.

In [70], spherical snowball model for conductor surface roughness is proposed. Power absorption due to scattering from snowball-shaped nodules on flat surface, as illustrated in Figure 2.30 is calculated by neglecting second order effects. Magnetic and electric fields are computed considering power absorption due to those irregularities. Comparing computed wave losses with measurement results up to 50 GHz, snowball model gives the most accurate and consistent consequences by taking many parameters such as radius of sphere per hexagonal surface area, distribution of the nodules and material properties into account [65]. Also, Huray model with cubic closed-packaging approach is applied for the various numbers of the equal hemispheres in a certain cross section and shows the validity and accuracy of the method providing measured and simulated results. Therefore, Huray's spherical snowball model for surface roughness is preferred to analyze the effect of the surface roughness on filtering response in this thesis.

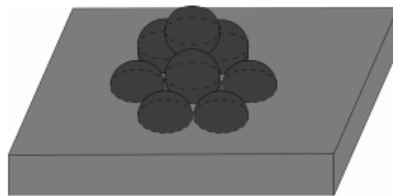


**Figure 2.30.** Snowball model [65].

The authors of [71] proposes modified Hammerstad correction coefficient with identification of the surface roughness by means of generalized modal scattering parameters and propose roughness model for transmission lines. It is concluded that conductor surface roughness brings about the increment of the reactance of the line and power dissipation due to the grooves on rough conductor.

In [72], effect of the surface roughness is investigated for stripline by presenting computational results and specific conductor profiles are analyzed using Hammerstad-Jensen empirical formula.

Filament model consisting of resistances and mutual inductances for the surface roughness is proposed in [73]. It is analyzed for pyramid and ellipsoid shaped

roughness profiles considering the frequency dependence of the skin effect model. The surface roughness increases the resistance and inductance of the cross sectional area of the line and skin effect model is used to calculate the components of the filament model.

In [74], the impact of the random rough surfaces on power dissipation in conductor is investigated at microwave frequencies. Numerical approaches such as analytical perturbation method and method moments using periodic Green's function are employed to compute the power absorption ratio of the rough conductor. Influence of the root means square (RMS) height of the roughness on power loss is analyzed.

The authors of [75] study the impact of the conductor roughness on wave propagation in parallel plate waveguide. Coherent wave propagation and power absorption ratio along waveguide is computed using double Sommerfeld integral and the results are compared with that of several methods. It is illustrated that coherent wave decaying and power dissipation on rough conductor are much higher than smooth conductor.

Delving into the studies on modeling conductor surface roughness and waveguide filter structures, none of them dwells on a design framework for the miniaturized and narrowband direct-coupled filter by taking surface roughness effect into account efficiently. Major contribution of this thesis is development and validation of the systematic design methodology considering conductor roughness effect for compact and highly selective direct-coupled waveguide filter employing in multiplexer configurations as channel filter in satellite payload system.





## CHAPTER III

### CHANNEL FILTER DESIGN

#### 3.1. Generalized Design Methodology

Microwave filter design procedure which is explored in [1] and [13] with all steps of that generalized approach is given in Figure 3.1 as flow chart diagram. Taking those into consideration, the waveguide filter design studies are shaped and accomplished. The explanations of each step for filter design procedure are thoroughly mentioned as follows:

- 1.) Determining the desired filter specifications which are usually varied depending on the requirements of the systems is the first step of the design procedure. The electrical parameters such as center frequency, insertion loss, bandwidth, return loss, stop band attenuation are clearly described and possible bottlenecks for the achievement are evaluated. Also, mechanical requirements are determined considering the physical constraints of the systems about maximum weight, volume and length. Generally, a compromise amongst electrical and mechanical prerequisites should be made for obtaining the physically feasible structure together with satisfying the requirements [1]. Therefore, physical feasibility, system requirements and design constraints usually give shape the final filter specifications. Comparison between different technologies for realization is presented in Table 3.1.

**Table 3.1.** Comparison between different realization technologies [76]

<b>Realization Technology</b>	<b>Size</b>	<b>Loss</b>	<b>Bandwidth</b>	<b>Spurious</b>	<b>Power Handling</b>
<i>Rectangular Waveguide</i>	medium/large	low	small	medium	very high
<i>Ridge Waveguide</i>	small	medium	medium/large	very good	high
<i>Circular Waveguide</i>	medium/large	low	small	medium	very high
<i>Coaxial TEM Lines</i>	small	medium	small/medium	good	medium
<i>Planar Structure</i>	very small	high	medium/large	good	very low
<i>Dielectric Loaded</i>	small/medium	very low	very small	very poor	low

2.) The type of filter and fabrication technology should be properly chosen considering the desired filter response. Butterworth, Chebyshev, Bessel, Quasi-elliptic, and Elliptic are mostly exploited types of the filter. Chebyshev filter type is preferred for this study in order to meet sharp skirt response in passband and high rejection at adjacent channel.

3.) After the selection of the filter topology, synthesis procedure of the ideal circuit prototype is initiated to determine the lumped elements performing the desired filter response. On the other hand, some transformations and identities such as Kuroda identities and transformations from low-pass prototype are indispensable to have lumped-element features of the filter [1] .

4.) By exploiting the synthesized circuit prototype, the initial dimensions for filter structure are obtained. One should pay particular attention to the consistency of the initial filter response with the synthesized circuit response. Because for the generation of the initial dimensions, the physical dimensions are mapped with synthesized circuit equivalent by using commensurate network transformations,

classical formulas or full wave numerical techniques. A hybrid procedure including full-wave and circuit level characterizations are proposed in the following sections.

5.) After initial dimensions are obtained, full wave optimization procedure is applied to determine the optimum values for desired filter performance. In order to improve the filter response, tuning procedure is required to extract final filter dimensions.

6.) Experimental set-up is constructed to compare measurement results with the expectations. By comparing the electrical performance parameters such as insertion loss, return loss, bandwidth; some modifications on filter structure can be made before the final version of it.

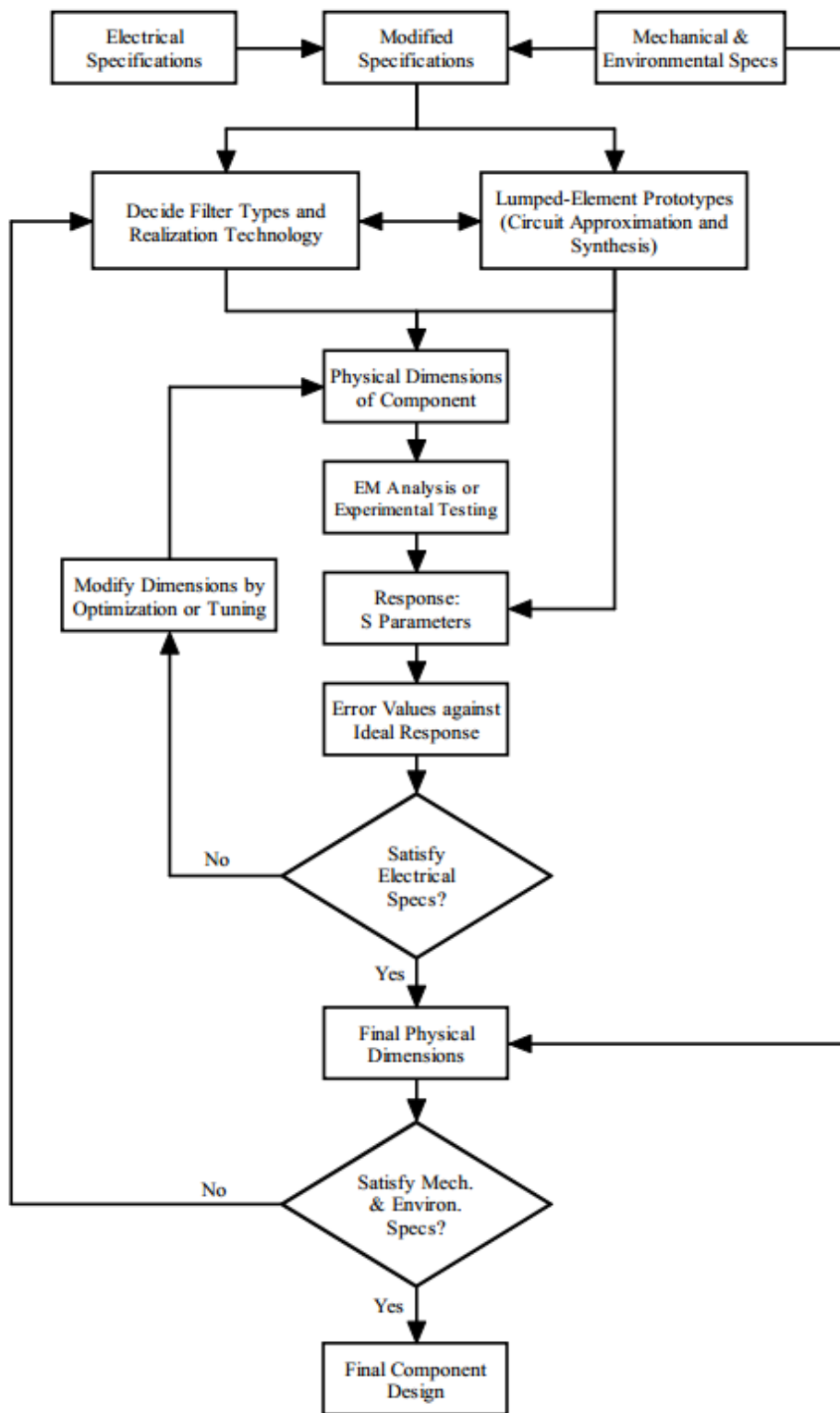


**Figure 3.1.** Filter design procedure [1]

### 3.2. Calculation of the Filter Order

Depending on the filter specifications such as passband ripple, stop band attenuation, return loss in passband and skirt selectivity, calculation of the relevant degree of filter is critical for conceiving the efficient filter structure satisfying the filter requirements. In order to fulfill the filter specifications listed below, the following calculation method in [77] is carried out.

- Center frequency,  $f_c$ : 17 GHz  $\rightarrow \omega_c = 2\pi f_c = 106.82 \times 10^9$  rad/s
- Lower band-edge frequency,  $f_1$ : 16.977 GHz  $\rightarrow \omega_1 = 2\pi f_1 = 106.675 \times 10^9$  rad/s
- Higher band-edge frequency,  $f_2$ : 17.023 GHz  $\rightarrow \omega_2 = 2\pi f_2 = 106.964 \times 10^9$  rad/s
- 3-dB bandwidth,  $f_{3dB}$ : 46 MHz
- 1-dB bandwidth: 40 MHz
- Passband ripple: 0.01 dB
- Desired rejection: 30 dB @  $f=17.046$  GHz  $\rightarrow \omega = 2\pi f = 107.10 \times 10^9$  rad/s

$$\omega_0 = \sqrt{\omega_1 \omega_2}$$

$$\omega' = \frac{\omega_0}{\omega_2 - \omega_1} \left( \frac{\omega}{\omega_0} - \frac{\omega_0}{\omega} \right) = 1.932$$

$$\left| \frac{\omega'}{\omega_1'} \right| - 1 = 0.932$$

where  $\omega_1'$  is normalized frequency variable and it is always equal to 1.00.

Evaluating the calculated parameters with analytical curves in [77], order of the filter is determined as *eight* for satisfying all of the prescribed design specifications desirably and ideal transmission, reflection responses calculated numerically are illustrated in Figure 3.2.

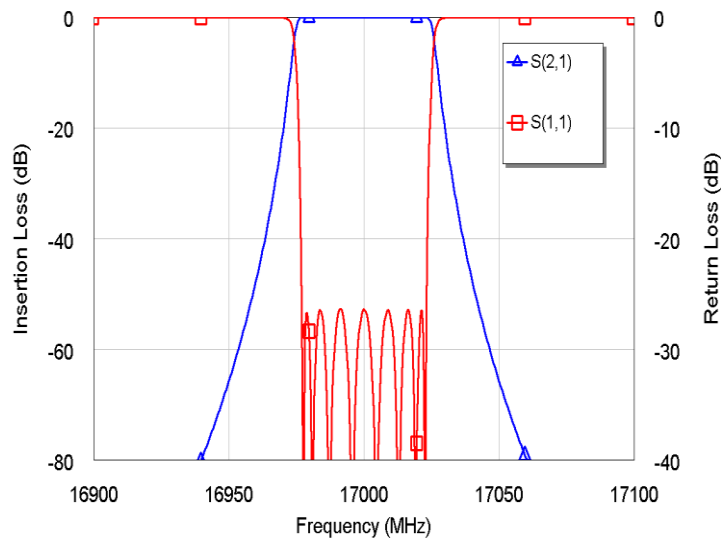


**Figure 3.2.** Ideal filter response.

### 3.3. Developing a design framework for miniaturized waveguide channel filter

One of the main goals of this study is to miniaturize the waveguide dimensions to get rid of the bulkiness of the waveguide while performing the desired filter characteristics in Ku band. However, some trade-offs between filter response and waveguide dimensions and also some restrictions are available. So, it is also intended to determine limitations on the waveguide in order to achieve narrow band pass filtering response. For that purpose, a systematic and practical design procedure for direct-coupled waveguide filters are developed with computer-aided optimization tools and framework is thoroughly described by presenting all findings and computations.

#### 3.3.1. Design of the Direct-Coupled Waveguide Filter

Direct-coupled filters are mainly composed of waveguide cavities or inductive, capacitive coupled TEM transmission lines by series capacitance or shunt inductance [78]. The equivalent circuit of the direct coupled iris waveguide filter,

shown in Figure 3.3.a, is illustrated in Figure 3.3.b. An iris placed in a waveguide can be modeled as shunt inductance, assuming that the thickness of the iris is very small compared to the guided wavelength ( $\frac{t}{\lambda_g} < 0.011$ )[62]. A design methodology which provides the direct acquisition of the initial design parameters of the filter is investigated and hence an efficient and practical one is developed.

Starting from numerical calculations using empirical formulations, design procedure for direct coupled iris waveguide filter is explained stage by stage and simulation results are presented accordingly. Also, direct coupled filter structure is divided into subsections in order to extract the circuit model of the each section and corresponding circuit equivalent model is achieved. Furthermore, the details about the proposed optimization procedure for the compact waveguide filter are mentioned together with numerical results.

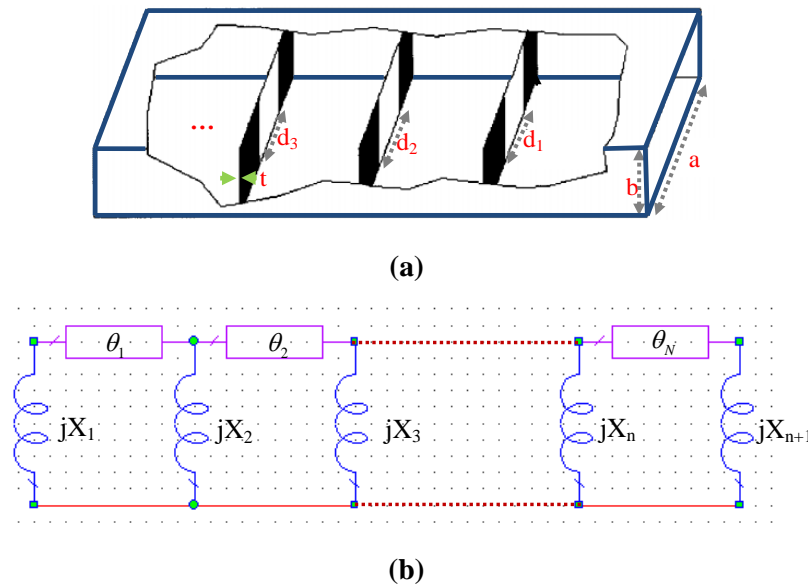


**Figure 3.3** (a) Direct-coupled filter, (b) equivalent circuit of n section coupled filter.

The design procedure for the direct-coupled filter is mainly based on three steps:

I. *Determine the Lowpass prototype constants*

The design procedure commences with determining ‘ $g$ ’ values for low pass prototype of Chebyshev filter specifications, shown in Figure 3.4 . The low pass prototype ‘ $g$ ’ parameters calculated as in [62] for desired filter specifications are written as:

$$g_0=1, g_1=0.8072, g_2=1.4130, g_3=1.7824, g_4=1.6833, g_5=1.8529, g_6=1.6193, g_7=1.5554, g_8=0.7333, g_9=1.1007$$

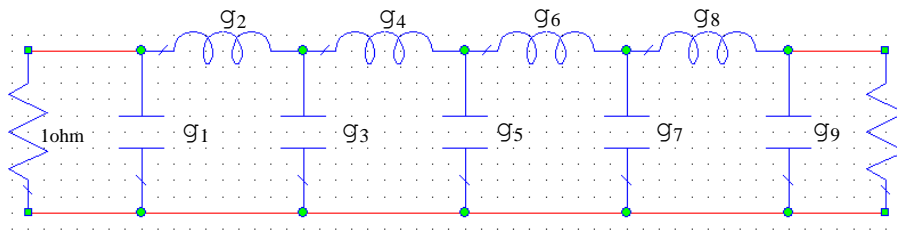


**Figure 3.4.** Low pass prototype with ‘ $g$ ’ constants.

Analytical transmission and reflection curves for the corresponding band pass prototype are illustrated in Figure 3.2. Analytical calculations and derivations are continued on the basis of those relevant LP prototype constants.

II. *Calculate lengths of the resonators and iris dimensions*

Conceiving compact filter geometry is main goal and novel side of this study. The aim for the miniaturization is to achieve a WG filter whose cross section becomes considerably reduced such as at least quarter of the WR62 standard waveguide ( $a=15.8$  mm,  $b=7.9$  mm) employed in payload systems. So, the width and height of it is adjusted gradually considering that goal by acquiring appropriate cut off condition of the waveguide. As a result, width and height of the waveguide are



determined as 10 mm and 3mm, respectively and cross section area of the filter is reduced to 24% of the standard WR62 filter. It makes the entire payload network lighter and hence lowers the launching cost which is straightforwardly corresponding to the overall weight of the system especially for satellite communication networks [3]. In order to calculate the values of the resonator's lengths and iris dimensions analytically, related formulations are derived below.

The characteristic impedance and propagation constant of a waveguide section can be expressed as in (3.1) and (3.2).

$$Z_{ch} = \frac{\eta \lambda_g}{\lambda_{g0}} = \frac{\eta}{\left[1 - \left(\frac{\omega_c}{\omega}\right)^2\right]^{\frac{1}{2}}} \quad (3.1)$$

$$\beta = \frac{2\pi}{\lambda_g} = \frac{\omega}{v} \left[1 - \left(\frac{\omega_c}{\omega}\right)^2\right]^{\frac{1}{2}} \quad (3.2)$$

The characteristic impedance is not significant since all the elements in waveguide filter are normalized with respect to terminating impedance [49]. So, it can be neglected for the filter calculations. ABCD matrix of the waveguide section is written as in (3.3).

$$[ABCD]_{line} = \begin{bmatrix} \cos \theta & jZ_{ch} \sin \theta \\ jY_{ch} \sin \theta & \cos \theta \end{bmatrix} \quad (3.3)$$

where  $\theta = \beta l = \frac{2\pi l}{\lambda_g} = \frac{\pi \lambda_{g0}}{\lambda_g}$

Length of the waveguide section is taken as  $l = \frac{\lambda_{g0}}{2}$  for derivations. ABCD matrix of an iris placed in waveguide and represented as shunt inductor is written as in (3.4) [62]-[49].

$$[ABCD]_{iris} = \begin{bmatrix} 1 & 0 \\ -jB \frac{\lambda_g}{\lambda_{g0}} & 1 \end{bmatrix} \quad (3.4)$$

The electrical length of the waveguide section is expressed as in (3.5).

$$\varphi = \varphi_0 \frac{\lambda_{g0}}{\lambda_g} \quad (3.5)$$

Assuming that the iris is placed at the midpoint of the waveguide section, ABCD matrix of the overall section is derived as follows in [78]-[39]:

$$\begin{aligned} \begin{bmatrix} A & B \\ C & D \end{bmatrix}_{overall} &= \begin{bmatrix} \cos \varphi/2 & j \sin \varphi/2 \\ j \sin \varphi/2 & \cos \varphi/2 \end{bmatrix} \begin{bmatrix} 1 & 0 \\ -jB \frac{\lambda_g}{\lambda_{g0}} & 1 \end{bmatrix} \begin{bmatrix} \cos \varphi/2 & j \sin \varphi/2 \\ j \sin \varphi/2 & \cos \varphi/2 \end{bmatrix} \\ &= \begin{bmatrix} \cos \frac{\varphi}{2} + B \frac{\lambda_g}{\lambda_{g0}} \sin \frac{\varphi}{2} & j \sin \frac{\varphi}{2} \\ j \sin \frac{\varphi}{2} - jB \frac{\lambda_g}{\lambda_{g0}} \cos \frac{\varphi}{2} & \cos \frac{\varphi}{2} \end{bmatrix} \begin{bmatrix} \cos \frac{\varphi}{2} & j \sin \frac{\varphi}{2} \\ j \sin \frac{\varphi}{2} & \cos \frac{\varphi}{2} \end{bmatrix} \\ &= \begin{bmatrix} \cos^2 \frac{\varphi}{2} - \sin^2 \frac{\varphi}{2} + B \frac{\lambda_g}{\lambda_{g0}} \sin \frac{\varphi}{2} \cos \frac{\varphi}{2} & j \left[ 2 \sin \frac{\varphi}{2} \cos \frac{\varphi}{2} + B \frac{\lambda_g}{\lambda_{g0}} \sin^2 \frac{\varphi}{2} \right] \\ j \left[ 2 \sin \frac{\varphi}{2} \cos \frac{\varphi}{2} - B \frac{\lambda_g}{\lambda_{g0}} \cos^2 \frac{\varphi}{2} \right] & \cos^2 \frac{\varphi}{2} - \sin^2 \frac{\varphi}{2} + B \frac{\lambda_g}{\lambda_{g0}} \sin \frac{\varphi}{2} \cos \frac{\varphi}{2} \end{bmatrix} \\ &= \begin{bmatrix} \cos \varphi + B \frac{\lambda_g}{2\lambda_{g0}} \sin \varphi & j \left[ \sin \varphi + B \frac{\lambda_g}{\lambda_{g0}} \sin^2 \frac{\varphi}{2} \right] \\ j \left[ \sin \varphi - B \frac{\lambda_g}{\lambda_{g0}} \cos^2 \frac{\varphi}{2} \right] & \cos \varphi + B \frac{\lambda_g}{2\lambda_{g0}} \sin \varphi \end{bmatrix} \end{aligned} \quad (3.6)$$

Equating (3.6) with the ABCD matrix and inverter is expressed as in (3.7).

$$[ABCD]_{inverter} = \begin{bmatrix} 0 & -j \frac{\lambda_{g0}}{J\lambda_g} \\ -j \frac{J\lambda_g}{\lambda_{g0}} & 0 \end{bmatrix} \quad (3.7)$$

where J is the characteristic admittance when  $\lambda_g = \lambda_{g0}$ .

$$\begin{aligned} [ABCD]_{inverter} &= [ABCD]_{overall} \\ \begin{bmatrix} 0 & -j \frac{\lambda_{g0}}{J\lambda_g} \\ -j \frac{J\lambda_g}{\lambda_{g0}} & 0 \end{bmatrix} &= \begin{bmatrix} \cos \varphi + B \frac{\lambda_g}{2\lambda_{g0}} \sin \varphi & j \left[ \sin \varphi + B \frac{\lambda_g}{\lambda_{g0}} \sin^2 \frac{\varphi}{2} \right] \\ j \left[ \sin \varphi - B \frac{\lambda_g}{\lambda_{g0}} \cos^2 \frac{\varphi}{2} \right] & \cos \varphi + B \frac{\lambda_g}{2\lambda_{g0}} \sin \varphi \end{bmatrix} \end{aligned}$$

$$\cos \varphi + B \frac{\lambda_g}{2\lambda_{g0}} \sin \varphi = 0$$

Hence,  $\varphi_0 = -\tan^{-1}\left(\frac{2}{B}\right) = -\tan^{-1}(2X)$ .

Subtracting parameter 'C' from parameter 'B' of [ABCD] both at left and right hand side of the matrix, relationship between impedance, admittance inverter and impedance value of iris is derived as in (3.8), (3.9), (3.10).

$$J - \frac{1}{J} = B \left[ \sin^2 \frac{\varphi}{2} + \cos^2 \frac{\varphi}{2} \right] = B \quad (3.8)$$

$$\frac{1}{K} - K = \frac{1}{X} \quad (3.9)$$

$$X = \frac{K}{1-K^2} \quad (3.10)$$

Taking  $Z_{ch}$  into account,(3.10) can be rewritten as(3.11). The direct-coupled filter can be treated with the impedance inverter concept [78]. Thus, impedance inverter representation of the iris WG filter with related parameter illustration is shown in Figure 3.5.

$$\frac{X}{Z_{ch}} = \frac{\frac{K}{Z_{ch}}}{1 - \left(\frac{K}{Z_{ch}}\right)^2} \quad (3.11)$$

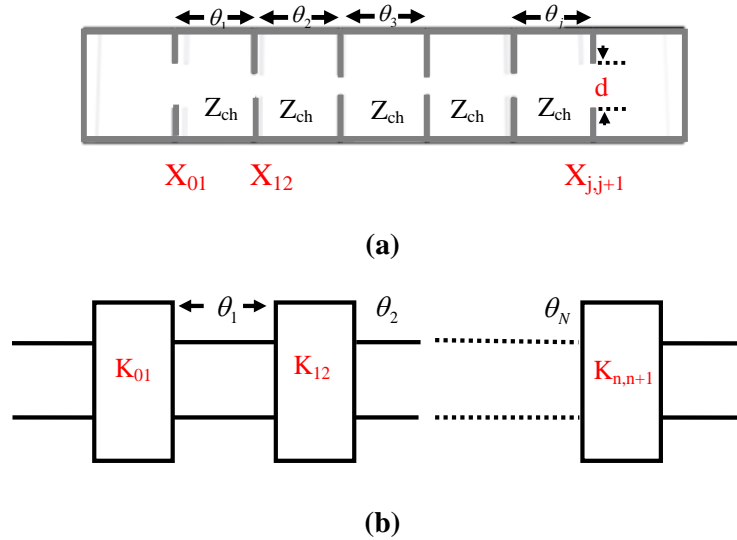


**Figure 3.5.** (a) Iris filter scheme, (b) impedance inverter representation of iris filter.

Considering the existence of the ‘j+1’ iris sections in waveguide filter as shown in Figure, the relationship between each irises is expressed as in (3.12).

$$\frac{X_{j,j+1}}{Z_{ch}} = \frac{\frac{K_{j,j+1}}{Z_{ch}}}{1 - \left(\frac{K_{j,j+1}}{Z_{ch}}\right)^2} \quad (3.12)$$

Electrical and physical lengths between each iris can be calculated from (3.13) and (3.14), respectively.

$$\theta_j = \pi - \frac{1}{2} \left[ \tan^{-1} \frac{2X_{j-1,j}}{Z_0} + \tan^{-1} \frac{2X_{j,j+1}}{Z_0} \right] \quad (3.13)$$

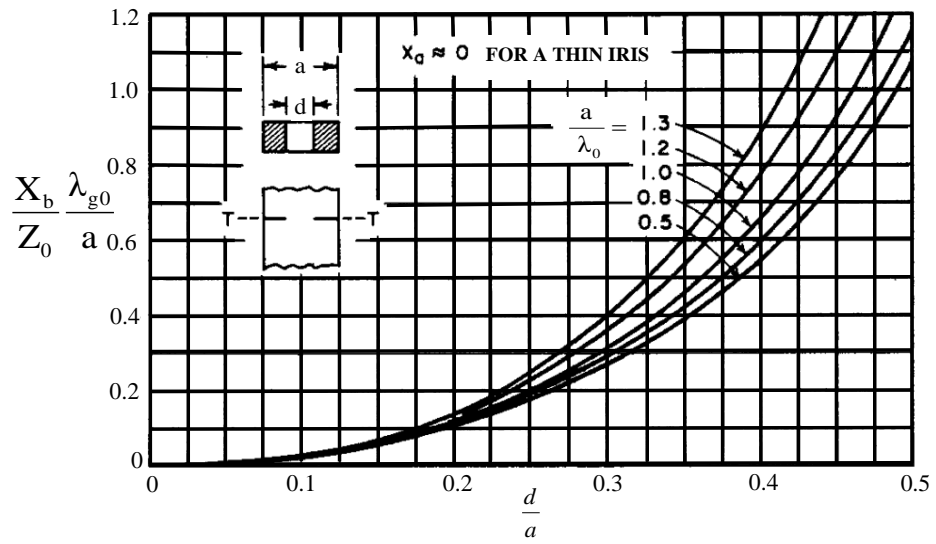
$$L_j = \frac{\theta_j \lambda_{g0}}{2\pi} \quad (3.14)$$

At the stage of initial length determination of the filter, the guide wavelengths at two band edges and center frequency are calculated as:  $\lambda_{g1}=37.7$  mm,  $\lambda_{g2}=37.3$  mm,  $\lambda_{g3}=37.5$  mm.

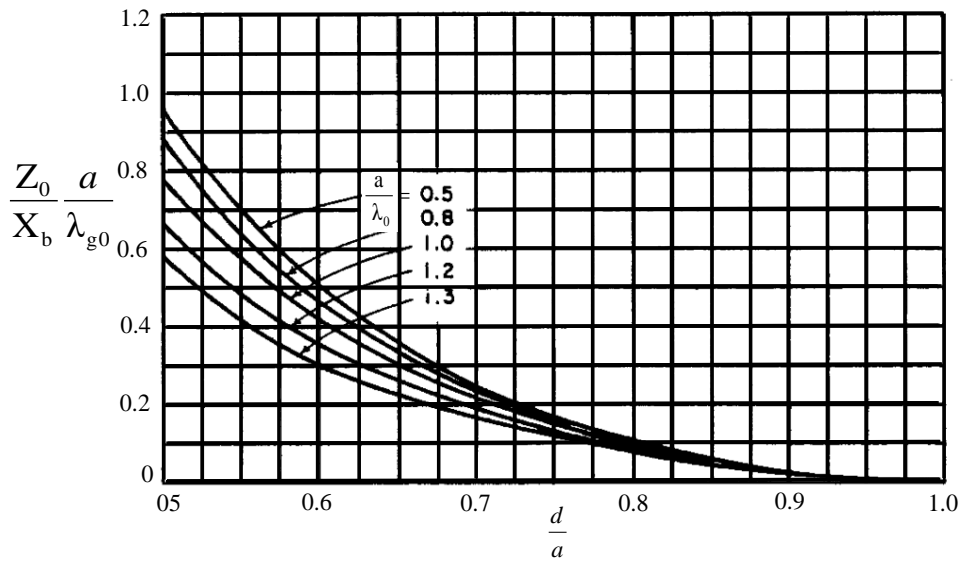
$\omega_\lambda = \frac{\lambda_{g1} - \lambda_{g2}}{\lambda_{g0}} = 0.0106$  where  $\omega_\lambda$  is the guided wavelength fractional bandwidth.

$$\frac{K_{n,n+1}}{Z_{ch}} = \sqrt{\frac{\pi \omega_\lambda}{2g_n g_{n+1} \omega'_1}} \quad (3.15)$$

Impedance inverter value (K), slope parameter of shunt reactance (X) and electrical length between each iris (L) are calculated by using (3.10), (3.11), (3.13) and (3.14). The curves in [62], shown in Figure 3.6, are exploited to determine proper the iris gap distance ‘d’ values by virtue of calculated parameter values. Iris thickness,  $t=0.2$  mm, are considered as zero thickness. The initial values of each iris widths are approximately calculated by determining the corresponding points on the curves. The values of the calculated parameters are listed in Table 3.2. This approach provides an opportunity to acquire the initial parameters values directly without any circuit transformations. At the end of the circuit model extraction, filter structure is quickly optimized and physical parameters are achieved practically.



(a)



(b)

**Figure 3.6.** Circuit parameters of symmetrical inductive iris [62].

**Table 3.2.** Calculated design parameters

LP prototype constant	Value	Reactance slope	Value ( $\Omega$ )	Inverter constant	Value
$g_1$	0.8072	$X_{01}$	0.3287	$K_{01}$	0.2068
$g_2$	1.4130	$X_{12}$	0.2550	$K_{12}$	0.1740
$g_3$	1.7824	$X_{23}$	0.1502	$K_{23}$	0.1171
$g_4$	1.6833	$X_{34}$	0.1346	$K_{34}$	0.1073
$g_5$	1.8529	$X_{45}$	0.1314	$X_{45}$	0.1052
$g_6$	1.6193	$X_{56}$	0.1346	$K_{56}$	0.1073
$g_7$	1.5554	$X_{67}$	0.1502	$K_{67}$	0.1171
$g_8$	0.7333	$X_{78}$	0.2550	$K_{78}$	0.1740
$g_9$	1.1007	$X_{89}$	0.3287	$K_{89}$	0.2068

Initial lengths and dimensions, listed in Table 3.3 can be calculated easily. Those provide a good starting point for the faster design of the direct-coupled filter and physical dimensions are obtained quickly at the end of local optimization process.

**Table 3.3.** Calculated lengths and distances

Electrical length of resonator	Value (rad)	Physical length of resonator	Value (mm)	Gap distance	Value (mm)
$\theta_1$	2.61	$L_1$	15.6	$d_1=d_9$	5.5
$\theta_2$	2.75	$L_2$	16.5	$d_2$	4.9
$\theta_3$	2.86	$L_3$	17.1	$d_3$	4.1
$\theta_4$	2.88	$L_4$	17.2	$d_4$	5.5
$\theta_5$	2.88	$L_5$	17.2	$d_5$	3.8
$\theta_6$	2.86	$L_6$	17.1	$d_6$	4.3
$\theta_7$	2.76	$L_7$	16.5	$d_7$	4.4
$\theta_8$	2.61	$L_8$	15.6	$d_8$	4.8

### III. Simulate the filter structure and optimize the lengths with distances

Direct-coupled filter structure is conceived as the channel filter section of the multiplexer by tuning the related design parameters, as shown in Figure 3.7. By virtue of the equivalent circuit models and transformations in [77], tuned circuit model is firstly optimized to have the channel filter, whose center frequency is 17 GHz, and 1-dB bandwidth is 40 MHz, and then full-wave analysis of it with optimized lengths is accomplished.

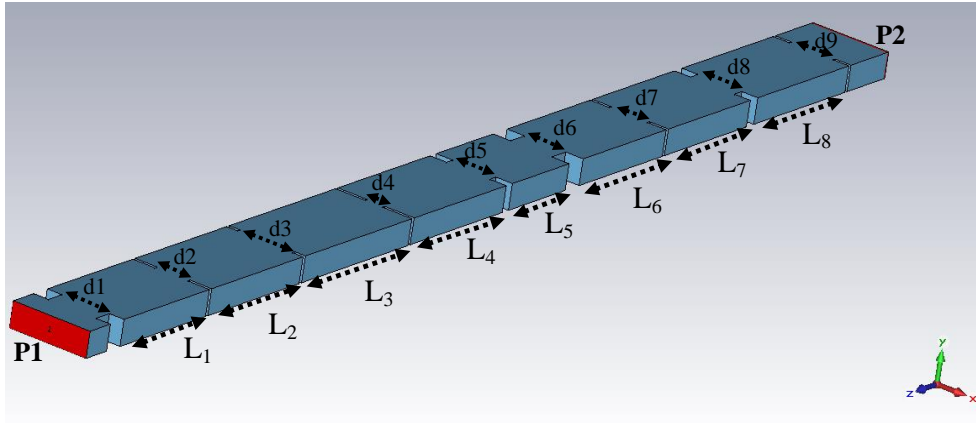


**Figure 3.7.** View of the direct-coupled filter.

Firstly, the iris filter structure are simulated with analytically calculated parameter values in Table 3.3 and scattering parameter curves, as shown in Figure 3.8, are observed without any optimization. Since the iris widths and resonator lengths are calculated approximately by means of appropriate curves in Figure 3.6 and obtained values with analytical formulations, fine-tuning and optimization of the parameters are inevitably necessary for suppressing unwanted responses existing at 17.3 and 17.4 GHz and obtain final filter dimensions with desired filtering response. For this purpose, the circuit equivalent model for each coupling irises are extracted to construct direct coupled filter structure. After obtaining the circuit model of the filter, investigation of the influence of the each resonator lengths and irises on filter response becomes much easier to fulfill filter specifications. Then, by considering filter response of the circuit model as initial point for optimization, direct-coupled filter structure is constructed after fine-tuning of the related parameters.

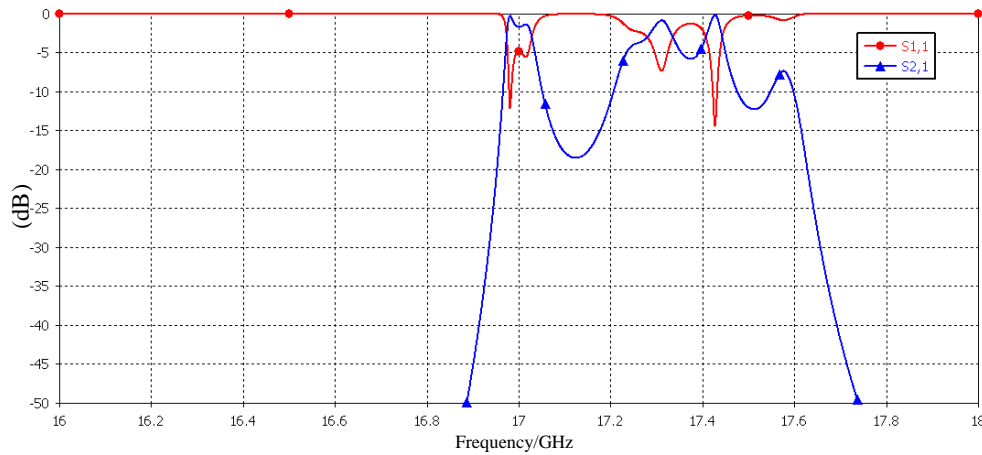


**Figure 3.8.** S-parameters for analytically calculated parameters without optimization

### 3.3.2. Construction of Circuit Equivalent Model

Frequency response of the cavity bandpass filters are degraded undesirably due to the frequency dependent characteristic of the coupling iris. In [77] and [62], T network comprising shunted inductance (L) and two series capacitance (C) lumped components are presented for the equivalent circuit of the coupling iris. Furthermore,  $\pi$  network comprising two shunted L and series C are proposed in [79]. In order to match magnitude and phase variations at the frequency response of the electromagnetic (EM) simulation with that of the circuit model, T- network is exploited and equivalent circuit model of the direct-coupled filter are constructed. In order to characterize inductive iris section of the waveguide and determine the shunt and series reactance in the circuit model shown in Figure 3.9, firstly full wave response is computed in CST Microwave Studio (MWS) to obtain S parameters. Secondly, equivalent T-network model is formed in CST Design Studio (DS) and finally magnitude and phase variation of  $S_{21}$  obtained from full-wave computation are fitted with that of the circuit model. The procedure is carried out for the channel filter operating at 17 GHz and consequences and findings are presented in detail for that single channel.



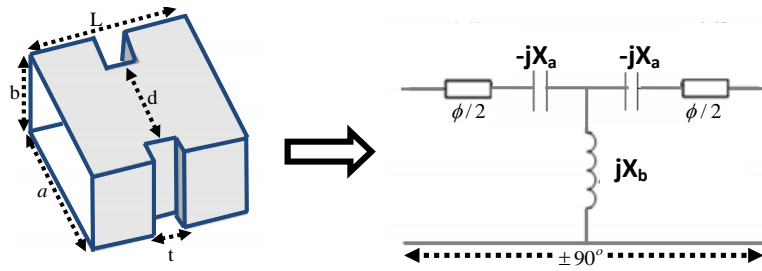


**Figure 3.9.** Inductive iris and its representation as impedance inverter

Effect of the iris aperture width on shunt and series reactance is investigated thoroughly and corresponding inductance and capacitance values are listed in Table 3.4 as iris thickness is equal to 0.4 mm, 0.6 mm and in Table 3.5 as 't' is equal to 0.8 mm, 0.9 mm whilst length of WG section is equal to quarter of the guided wavelength. Inductance variation with respect to changing gap distance is illustrated in Figure 3.10. Also, amplitude and phase variation of iris section in circuit and full-wave simulator for various sizes are depicted as Figure 3.11 and Figure 3.12. As iris thickness is increased, equal inductance decreases due to the fact that length of the iris surface becomes longer. Hence, the maximum achievable value for the shunt inductance decreases.

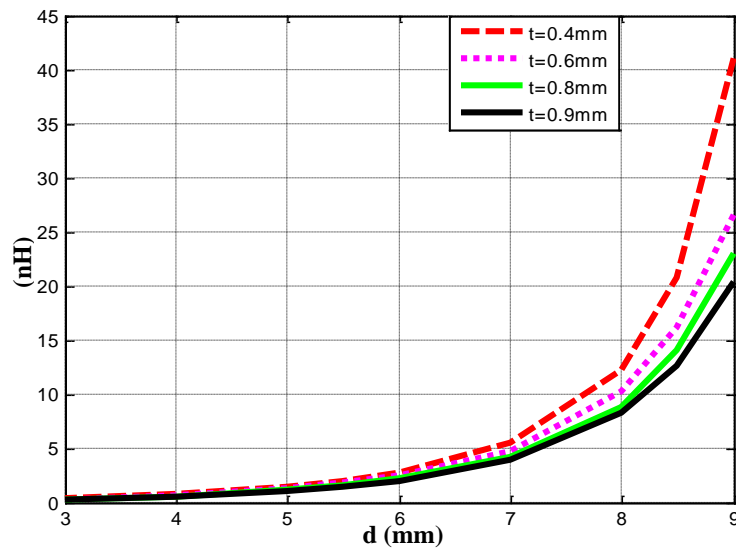


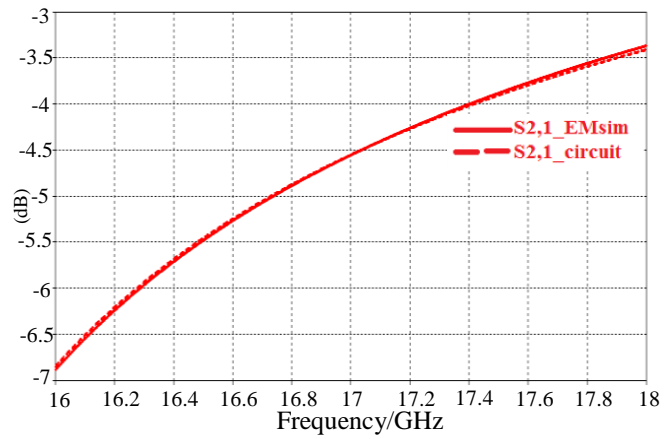
**Figure 3.10.** Inductance variation curves with respect to changing gap distance.

**Table 3.4.** Effect of iris aperture on circuit parameters for  $t=0.4$  mm and  $t=0.6$  mm

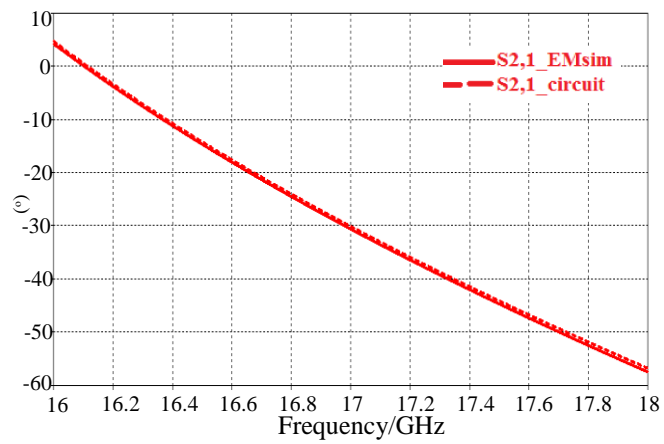
<b>d (mm)</b>	<b>t=0.4 mm</b>		<b>t=0.6 mm</b>	
	<b>L<sub>sh</sub> (nH)</b>	<b>C<sub>series</sub> (pF)</b>	<b>L<sub>sh</sub> (nH)</b>	<b>C<sub>series</sub> (pF)</b>
<b>9.0</b>	40.93	1.69	26.50	0.26
<b>8.5</b>	20.65	1.70	16.12	0.29
<b>8.0</b>	12.14	1.73	10.16	0.30
<b>7.0</b>	5.41	1.81	4.70	0.31
<b>6.0</b>	2.74	1.82	2.38	0.32
<b>5.5</b>	1.97	1.83	1.71	0.32
<b>5.0</b>	1.42	1.83	1.23	0.33
<b>4.0</b>	0.70	1.93	0.60	0.34
<b>3.0</b>	0.29	1.95	0.24	0.34

**Table 3.5.** Effect of iris aperture on circuit parameters for  $t=0.8$  mm and  $t=0.9$  mm

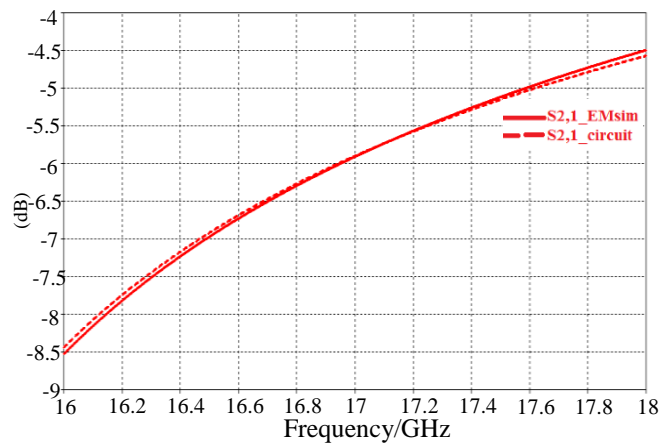
<b>d (mm)</b>	<b>t=0.8 mm</b>		<b>t=0.9 mm</b>	
	<b>L<sub>sh</sub> (nH)</b>	<b>C<sub>series</sub> (pF)</b>	<b>L<sub>sh</sub> (nH)</b>	<b>C<sub>series</sub> (pF)</b>
<b>9.0</b>	22.99	0.23	20.26	0.25
<b>8.5</b>	14.03	0.25	12.62	0.26
<b>8.0</b>	8.80	0.25	8.20	0.27
<b>7.0</b>	4.17	0.27	3.86	0.28
<b>6.0</b>	2.12	0.30	1.94	0.30
<b>5.5</b>	1.52	0.31	1.37	0.30
<b>5.0</b>	1.07	0.32	0.96	0.31
<b>4.0</b>	0.51	0.33	0.44	0.32
<b>3.0</b>	0.19	0.33	0.16	0.32



(a) Amplitude of  $S_{21}$  as  $t=0.4$  mm

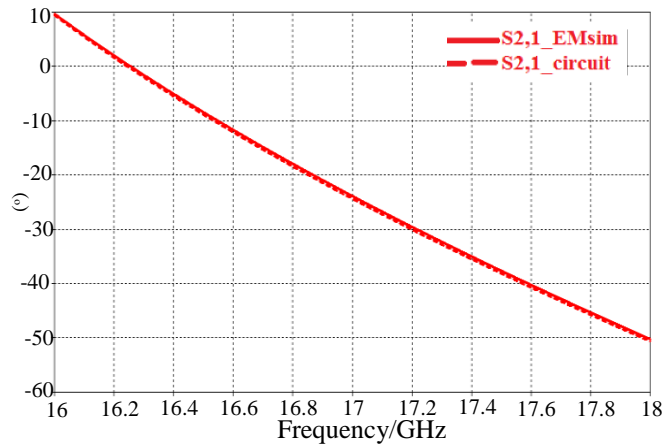


(b) Phase of  $S_{21}$  as  $t=0.4$  mm

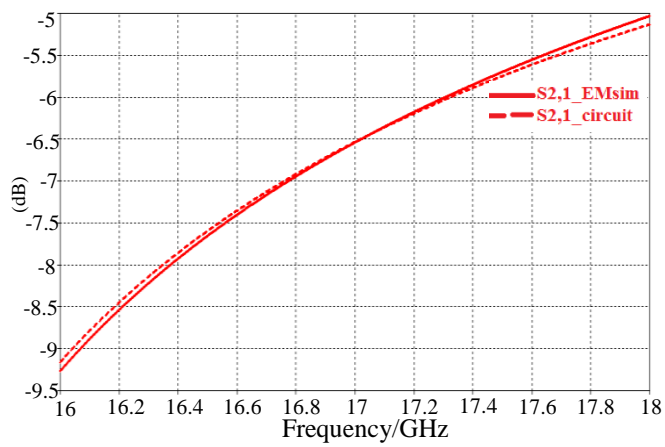


(c) Amplitude of  $S_{21}$  as  $t=0.8$  mm

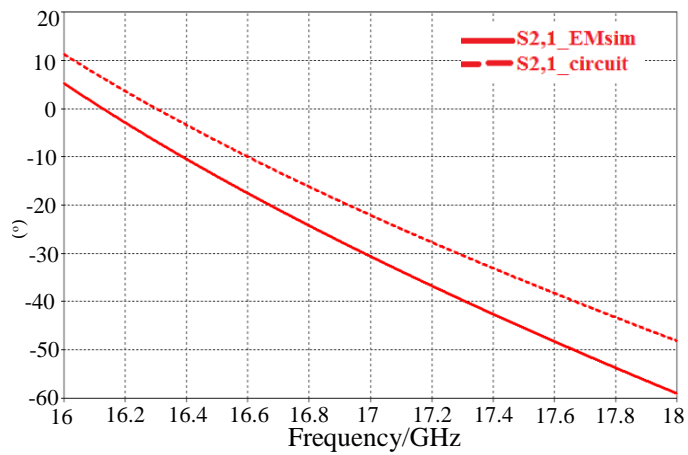
**Figure 3.11.**  $S_{21}$  curves as  $d=6$  mm in full-wave and circuit level (dashed line: full-wave simulation result, solid line: circuit simulation result).



(a) Phase of S<sub>21</sub> as t=0.8mm



(b) Amplitude of S<sub>21</sub> as t=1.0 mm



(c) Phase of S<sub>21</sub> as t=1.0 mm

**Figure 3.12.** S<sub>21</sub> curves as d=6 mm in full-wave and circuit level (dashed line: full-wave simulation result, solid line: circuit simulation result).

In the phase variation of  $S_{21}$ , when 'd' is taken as 6 mm,  $10^\circ$  phase difference is observed as shown in Figure 3.12.c whilst iris thickness is larger than 1mm. Hence, T network model becomes invalid for the thicker iris aperture size. Alternatively,  $\pi$ -network, shown in Figure 3.13, is exploited to achieve better phase agreement and characterize aperture thickness effect accurately. Better phase agreement is achieved whilst iris aperture thickness is larger than 1mm by using  $\pi$ -network model, as shown in Figure 3.14.

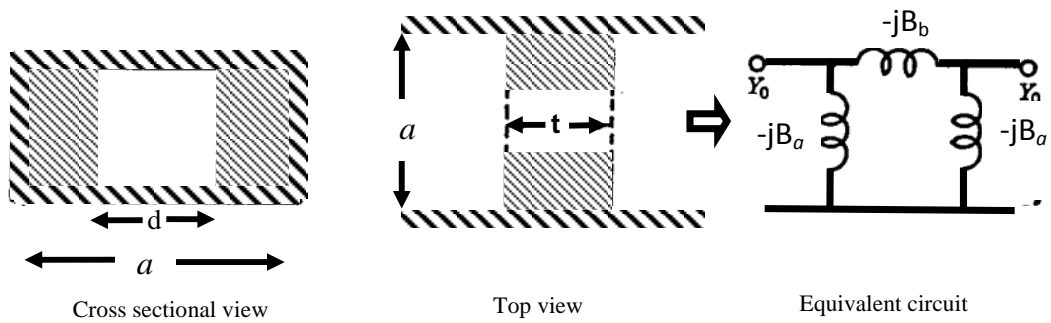


**Figure 3.13.** Inductive iris and its representation for larger iris thickness.

Effect of the iris aperture thickness on shunt and series reactance is investigated and corresponding inductance variations are illustrated in Figure 3.15 with respect to changing gap distance. Also, acquired values are listed in Table 3.6 whilst length of WG section is equal to quarter of the guided wavelength.

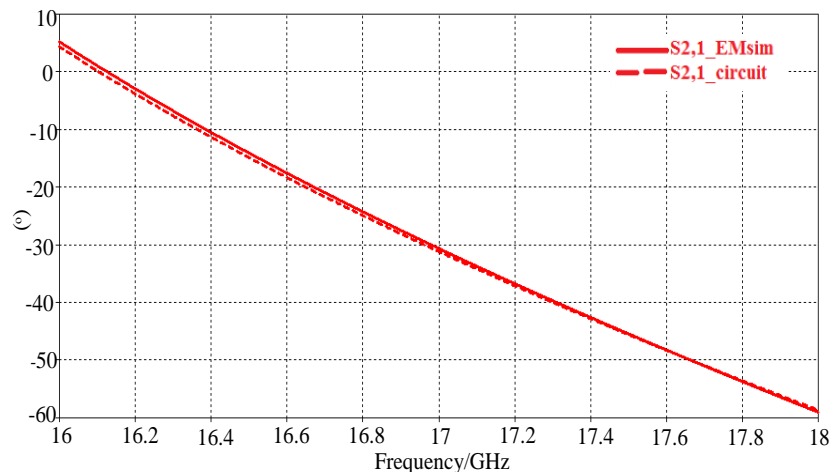


**Figure 3.14.** Phase of  $S_{21}$  as  $d=6\text{mm}$  and  $t=1\text{mm}$  in full-wave and circuit level.

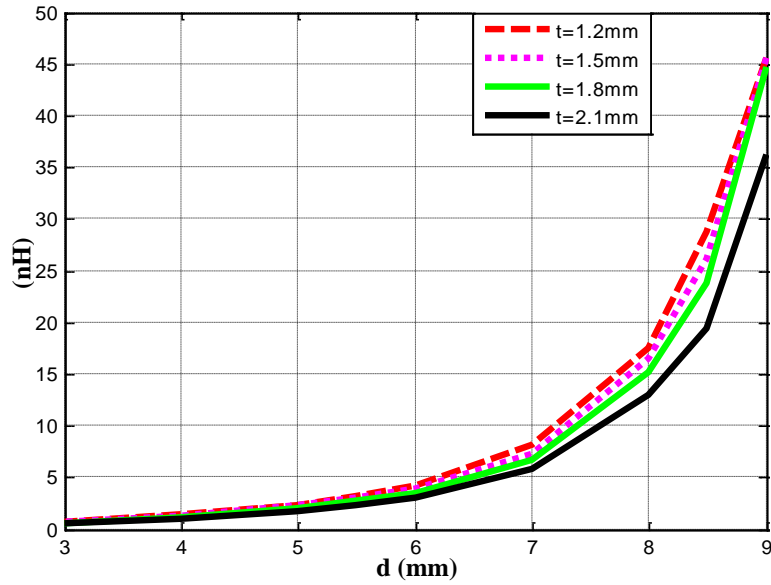


**Figure 3.15.** Shunt inductance variation curves with respect to changing gap distance.

**Table 3.6.** Effect of iris aperture on circuit parameters for different thickness values

d (mm)	t=1.2 mm		t=1.5 mm		t=1.8 mm	
	L <sub>sh</sub> (nH)	L <sub>series</sub> (nH)	L <sub>sh</sub> (nH)	L <sub>series</sub> (nH)	L <sub>sh</sub> (nH)	L <sub>series</sub> (nH)
9.0	45.59	0.11	45.58	0.17	44.72	0.30
8.5	28.69	0.20	26.10	0.47	23.77	0.53
8.0	17.51	0.37	16.38	0.80	15.16	0.87
7.0	8.08	0.70	7.27	1.02	6.62	1.10
6.0	4.16	0.89	3.89	1.50	3.49	1.56
5.5	3.10	1.14	2.93	1.78	2.65	1.89
5.0	2.26	1.25	2.26	2.20	2.01	2.24
4.0	1.34	1.88	1.26	2.47	1.13	2.68
3.0	0.70	2.23	0.65	2.93	0.57	3.12

The circuit model of the channel filter may be shaped by exploiting the T and  $\pi$  equivalent of the irises placed in the rectangular cavity in order to optimize and tune the filter response. The circuit model of the filter, shown in Figure 3.7, is composed of the hollow waveguide sections whose cut off frequencies are 15 GHz and T and  $\pi$  model of the irises, as shown in Figure 3.16.a. It is possible to tune L-C component values with tuning property of CST DS. By observing the effect of the variations of L-C components on filter characteristic, 3D filter structure can be modified properly until the desired filter performance is obtained. Optimized filter response is illustrated in Figure 3.16.b which is of 40 MHz bandwidth, sharp skirt selectivity and low insertion loss in passband. The lengths of the transmission lines are listed in Table 3.7. Values of the capacitances in series are given in Table 3.8 whilst those of the inductances are given in Table 3.9.

**Table 3.7.** Lengths ( in millimeters) of the transmission lines

<i>Par.</i>	TL1	TL2	TL3	TL4	TL5	TL6	TL7	TL8	TL9	TL10
<i>Val.</i>	6.04	15.56	17.14	20.33	18.19	17.86	18.10	16.87	18.65	17.93

**Table 3.8.** Values of the capacitances in series

<i>Parameters</i>	C1	C2	C3	C4	C5
<i>Value (pF)</i>	1.55	0.74	1.91	1.81	1.00

**Table 3.9.** Values of the inductances (in nH) in parallel and series

<i>Par.</i>	L <sub>1</sub>	L <sub>11</sub>	L <sub>2</sub>	L <sub>3</sub>	L <sub>4</sub>	L <sub>5</sub>	L <sub>51</sub>	L <sub>6</sub>	L <sub>61</sub>	L <sub>7</sub>	L <sub>8</sub>	L <sub>81</sub>	L <sub>9</sub>
<i>Val.</i>	5.26	1.69	0.53	4.51	0.22	0.69	4.59	3.51	1.36	3.32	7.99	1.77	3.65

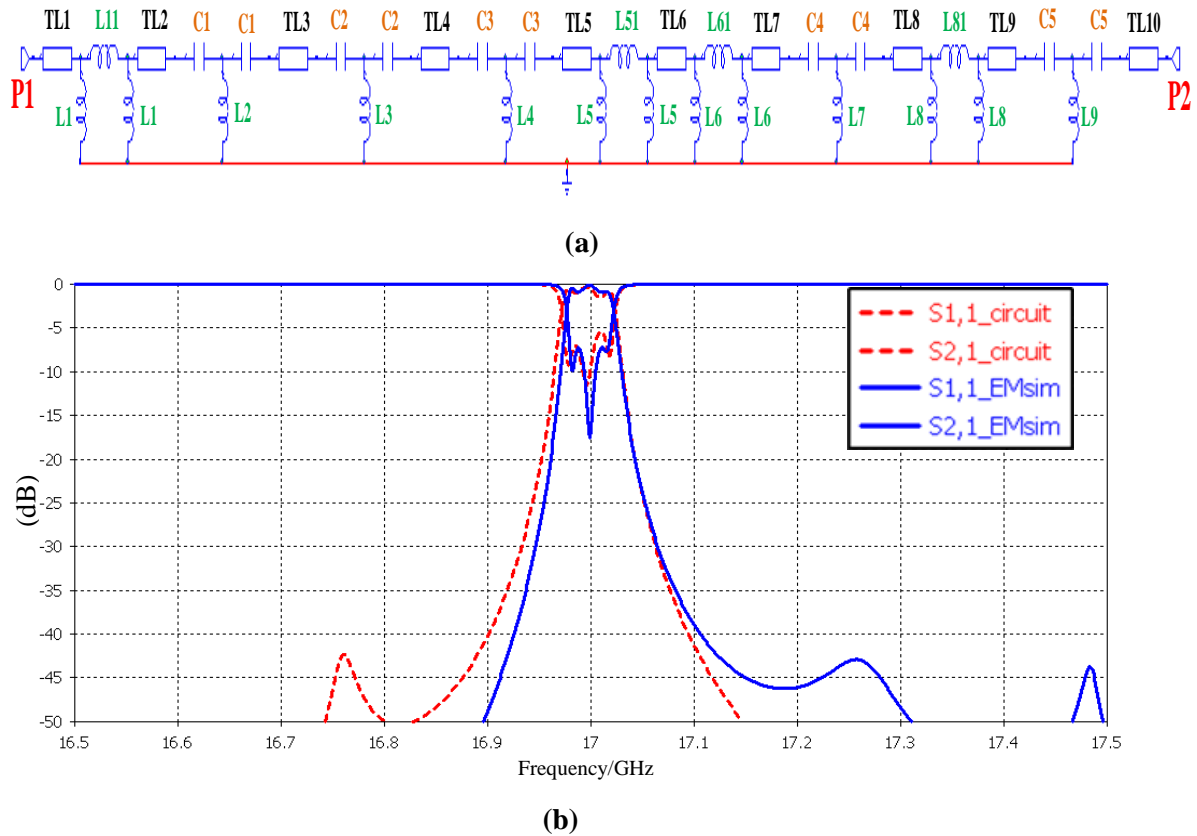


**Figure 3.16.** (a) Circuit schematic, (b) filter response of the direct-coupled filter (Dashed red: results in circuit simulation, solid blue: results in full-wave simulation).

Once certain filter structure is obtained at the end of all steps, it is easier and quicker to construct the adjacent channels. By scaling the lengths and distances appropriately with respect to the center frequency, channel filters operating various bandwidths can be generated efficiently and very fast. In order to inspect the usefulness of the scaling, the channel filter whose center frequency is 16.954 GHz is conceived from scratch and passband responses are compared with each other as shown in Figure 3.17. By exploiting the electrical scaling property of the structure, it is possible to have a desired filtering response instead of carrying out the design procedure from scratch with almost the same performance. And, this shows that the



channel filter structure obtained from scaling have the optimum filter performance that can be achieved from scratch.

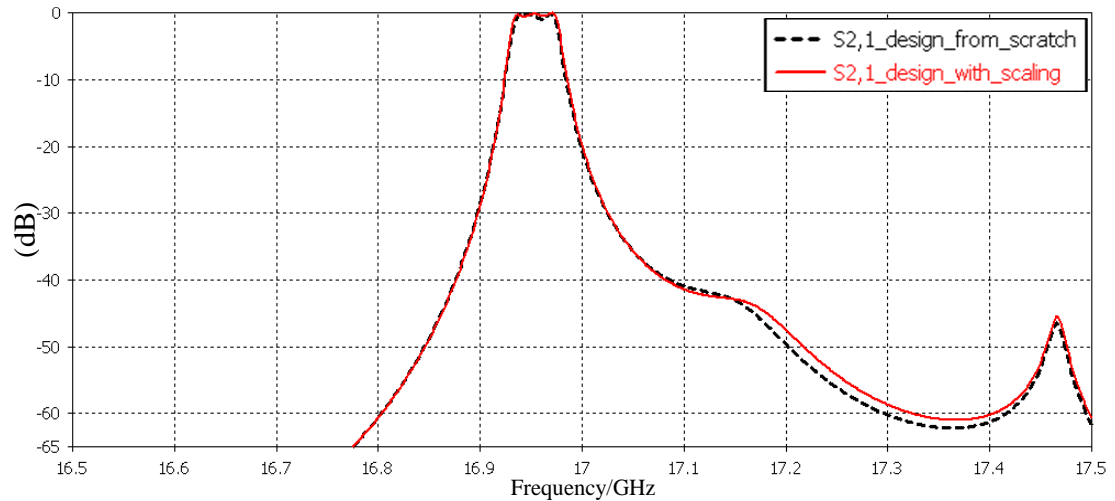
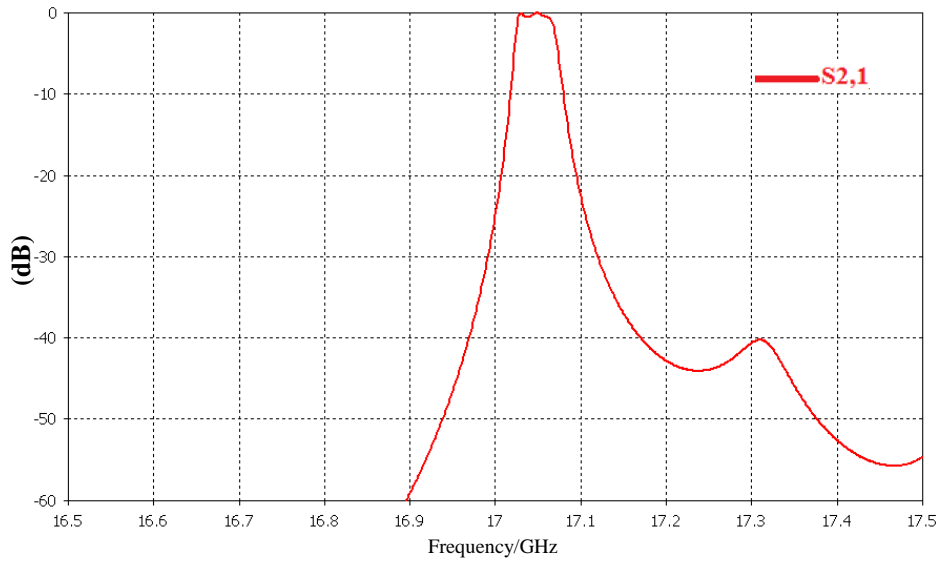
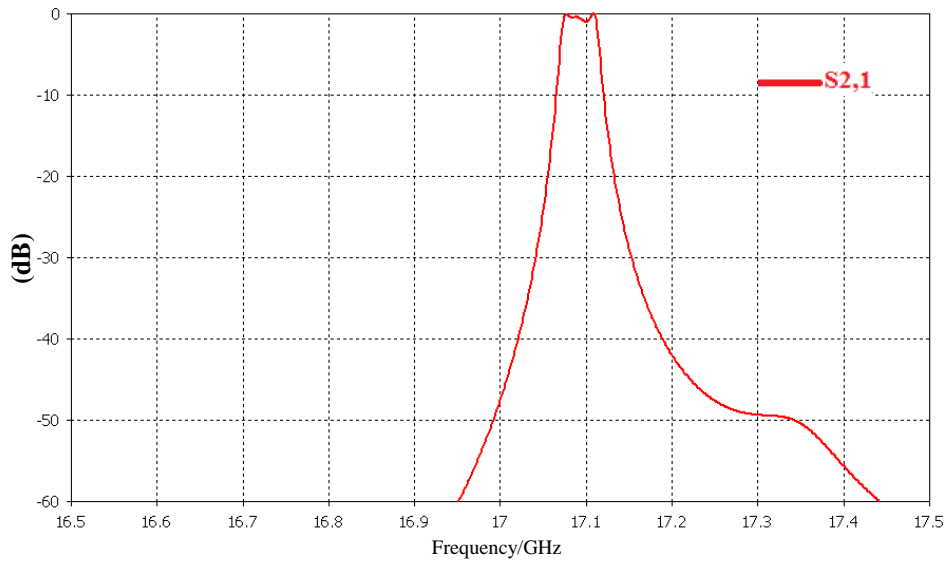


**Figure 3.17.** Comparison of the passband responses at  $f_{\text{center}} : 16.954$  GHz (dashed black: passband response of the design from scratch, solid red: passband response with scaling)

Passband responses of the channel filters at different operating bandwidths after a quick fine-tuning effort are illustrated in Figure 3.18 and Figure 3.19 . As a result, narrowband and selective channel filters are conceived to connect the manifold section of the six-channel contiguous band multiplexer. Numerical values as a result of the full-wave simulations for design parameters are listed in Table 3.10.

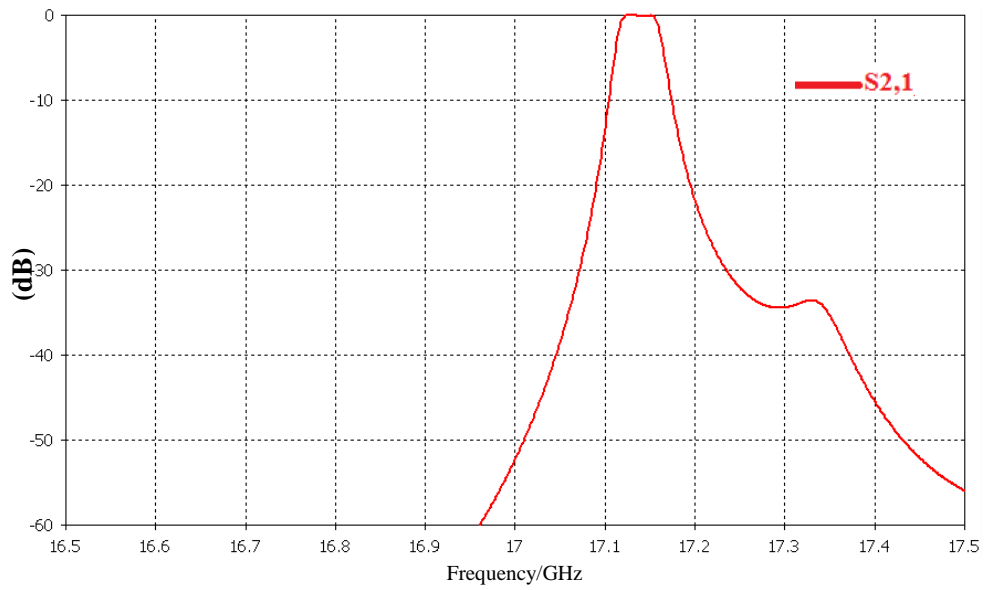


(a)  $f_{\text{center}} : 17.046 \text{ GHz}$

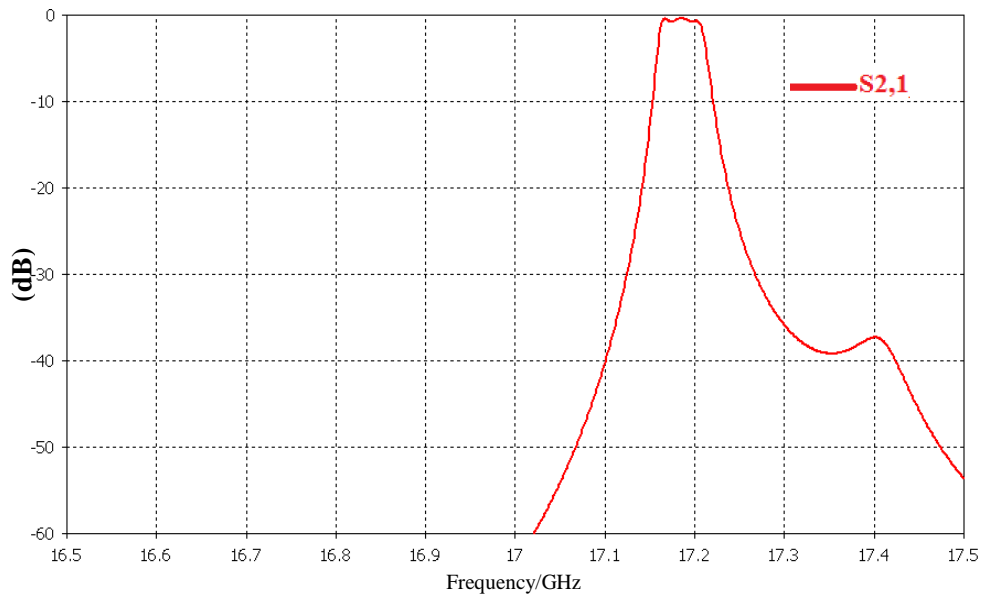


(b)  $f_{\text{center}} : 17.092 \text{ GHz}$

**Figure 3.18.** Passband responses of the filters at different center frequencies.



(a)  $f_{\text{center}} : 17.138 \text{ GHz}$



(b)  $f_{\text{center}} : 17.184 \text{ GHz}$

**Figure 3.19.** Passband responses of the filters at different center frequencies.

**Table 3.10.** Parameter values (in millimeters) for the channel filters

	<i>Ch# 1</i>	<i>Ch# 2</i>	<i>Ch# 3</i>	<i>Ch# 4</i>	<i>Ch# 5</i>	<i>Ch# 6</i>
<b>f<sub>center</sub> (GHz)</b>	16.954	17.000	17.046	17.092	17.138	17.184
<b>L1</b>	15.560	15.189	15.000	14.630	14.536	14.261
<b>L2</b>	16.719	16.306	16.260	16.039	15.708	15.518
<b>L3</b>	19.406	19.133	18.370	18.243	18.122	18.095
<b>L4</b>	16.876	16.703	16.375	16.358	16.067	15.866
<b>L5</b>	10.171	10.031	9.751	9.561	9.843	9.624
<b>L6</b>	15.138	15.130	14.856	14.675	14.596	14.330
<b>L7</b>	15.177	15.100	15.010	14.690	14.516	14.347
<b>L8</b>	17.017	16.920	16.900	16.865	16.269	16.078
<b>d1</b>	6.218	6.218	6.210	6.417	6.313	6.154
<b>d2</b>	4.068	4.289	4.413	4.089	4.017	4.077
<b>d3</b>	7.861	7.230	7.050	6.664	7.160	7.790
<b>d4</b>	2.371	2.314	2.372	2.278	2.526	2.290
<b>d5</b>	5.761	5.700	5.810	5.581	5.645	5.701
<b>d6</b>	5.566	5.421	5.361	5.417	5.350	5.450
<b>d7</b>	5.170	5.000	5.000	5.109	5.002	4.999
<b>d8</b>	5.899	5.696	5.826	5.658	5.981	5.701
<b>d9</b>	5.807	5.754	5.794	5.517	5.739	5.688
<b>t1</b>	1.153	2.396	2.386	2.210	2.396	2.390
<b>t2</b>	0.405	0.400	0.400	0.400	0.400	0.401
<b>t3</b>	0.475	0.450	0.450	0.400	0.450	0.451
<b>t4</b>	0.452	0.400	0.400	0.400	0.400	0.400
<b>t5</b>	1.137	1.111	1.210	0.965	0.400	1.109
<b>t6</b>	2.858	2.557	2.557	2.896	2.557	2.625
<b>t7</b>	0.413	0.400	0.400	0.407	0.400	0.400
<b>t8</b>	1.499	1.377	1.047	1.002	1.377	1.362
<b>t9</b>	0.426	0.400	0.400	0.731	0.400	0.402

## CHAPTER IV

### MANIFOLD-COUPLED MULTIPLEXER DESIGN

#### 4.1. Multiplexer Design Studies with the Analysis of Various Approaches

Different design methodologies are investigated and example multiplexer structures are conceived for the illustration. Also, a systematic framework for the design of the contiguous band multiplexer is developed and each stage of the design procedure is thoroughly performed with related information and consequences.

##### 4.1.1. Design of the Manifold via Short-Circuited Method

The manifold-coupled multiplexing, shown in Figure 4.1 is considered as the optimum approach as far as insertion loss and compactness are concerned. The utilization of the manifold structure interconnecting the channel filter is of great importance for the improvement of the multiplexer performance [4]. In manifold structure, transmission line is short-circuited at one end and the other end is the common port. The connection the channel filters to the manifold line is set through E or H-plane T-junctions. The length between channel filters and the one between each channel filters to manifold junction should be determined meticulously in order to compensate for the channel interaction effects and mismatching effects for individual channels [28].

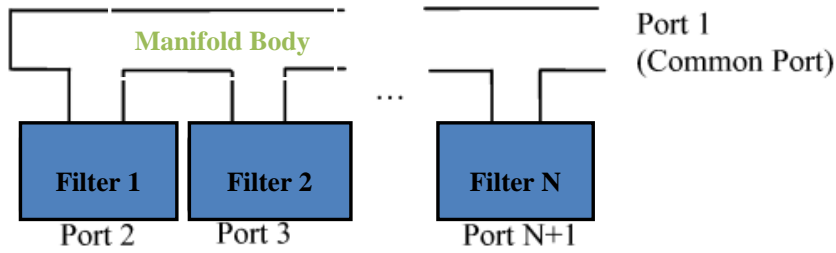


**Figure 4.1.**Manifold-coupled multiplexer.

The manifold body also brings an extra reflection zero into the passband of the multiplexer due to the resonant behavior of the E or H-plane T-junction [28], [30]. For a multiplexer design, the manifold with H-plane T-junction is analyzed and waveguide triplexer employing H-plane T-junctions is conceived.

#### 4.1.1.1. Analysis of Waveguide T- Junctions

The waveguide T-junctions can be modeled as a combination of the series or shunt transmission line sections. The equivalent circuit of H-plane T-junction is two short-circuited waveguide in parallel whilst that of E-plane T-junction is two short-circuited waveguide in series, as illustrated in Figure 4.2.

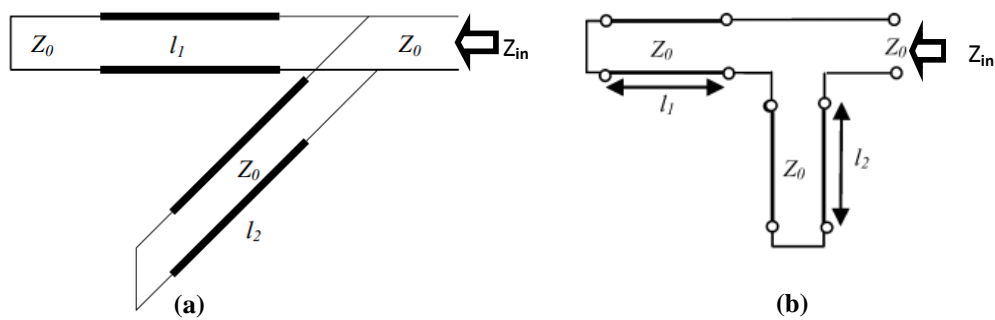


**Figure 4.2.**(a) Parallel connection, (b) series connection of two short-circuited waveguide [28].

Considering equivalent circuit of the H-plane T-junction in Figure 4.2.a, the impedance seen at common port can be expressed as:

$$Z_{in} = (jZ_0 \tan \beta l_1) \parallel (jZ_0 \tan \beta l_2) \quad (4.1)$$

where  $Z_0$  is the characteristic impedance,  $\beta$  is the propagation constant,  $l_1$  and  $l_2$  are the waveguide lengths, respectively. At resonance,  $Y_{in}=0$  or  $l_1 + l_2 = k\lambda_g/2$ , where  $k=1,2,3\dots$  and  $\lambda_g$  is the guided wavelength. The reflection coefficient at common port can be calculated as [30]:

$$S_{11} = |S_{11}| \angle \phi = \frac{Z_{in} - Z_0}{Z_{in} + Z_0} = \frac{j \tan \beta l_1 \tan \beta l_2 - (\tan \beta l_1 + \tan \beta l_2)}{j \tan \beta l_1 \tan \beta l_2 + (\tan \beta l_1 + \tan \beta l_2)} \quad (4.2)$$

$$\phi = -2 \cot^{-1} \left( \frac{(\tan \beta l_1 + \tan \beta l_2)}{\tan \beta l_1 \tan \beta l_2} \right) = -2 \cot^{-1} (\cot \beta l_1 + \cot \beta l_2) \quad (4.3)$$

The group delay  $\tau$  can be calculated as:

$$\tau = -\frac{\partial \phi}{\partial \omega} \quad (4.4)$$

Let  $y = (\cot \beta l_1 + \cot \beta l_2)$  and  $\tau(f)$  is expressed as:

$$\tau(f) = \frac{-\partial(2 \cot^{-1} y)}{\partial \omega} = -\frac{1}{\pi} \frac{1}{1+y^2} \frac{\partial y}{\partial f} \quad (4.5)$$

While  $y=0$  at resonance, it corresponds to group delay at the center frequency [28].

$$\text{Since } \lambda_0 = \frac{c}{f} \text{ and } \lambda_g = \lambda_0 / \sqrt{1 - \left(\frac{\lambda_0}{2a}\right)^2}.$$

Eqn. (4.5) can be written as:

$$\tau(f_0) = \frac{-\partial(2 \cot^{-1} y)}{\partial \omega} = -\frac{1}{\pi} \left( \frac{l_1}{\sin^2 \beta l_1} + \frac{l_2}{\sin^2 \beta l_2} \right) \frac{2\pi f \lambda_g}{c^2} \quad (4.6)$$

At resonance frequency,  $l_1 + l_2 = k\lambda_g/2$  or  $\beta(l_1 + l_2) = k\pi$ . Depending on the “k” values, the cases can be expressed as:

If k is odd,  $\beta l_1 = \pi + \theta$  and  $\beta l_2 = k\pi - \beta l_1$ .

If k is even,  $\beta l_1 = k\pi/2 + \theta$  and  $\beta l_2 = k\pi - \theta$ .

(4.6) can be simplified as [30]:

$$\tau(f_0) = \frac{kf_0\lambda_g^2}{c^2 \sin^2 \theta} \quad (4.7)$$

The coupling value R can be expressed as [28]:

$$R = \frac{2}{\pi(BW)} \frac{1}{\tau(f_0)} \quad (4.8)$$

where BW is the channel filter bandwidth. Once the required coupling value or group delay value together with resonance frequency, it is possible to find out the short-circuited waveguide length  $l_1$ .

#### 4.1.1.2. Manifold Design Steps

Three-channel contiguous band multiplexer is composed of narrowband channel filters whose center frequencies are 16.954 GHz, 17 GHz, 17.046 GHz, respectively, each with 40 MHz 1-dB bandwidth. The manifold design steps can be summarized as mentioned in [28], [29]:

- 1) In order to have good initial values for the lengths of manifold, all channel filters are replaced with short circuits in manifold structure, as shown in Figure 4.3.a, due to the fact that they act as short circuit in their out of bands. The lengths between channel filters and the lengths between each channel filters to manifold body are optimized to adjust group delay in the passband of each channel filters by using the circuit model in CST DS. The group delay response



of the common port after optimization process is shown in Figure 4.3.b. Three resonances at channel filters' center frequencies are clearly observed.

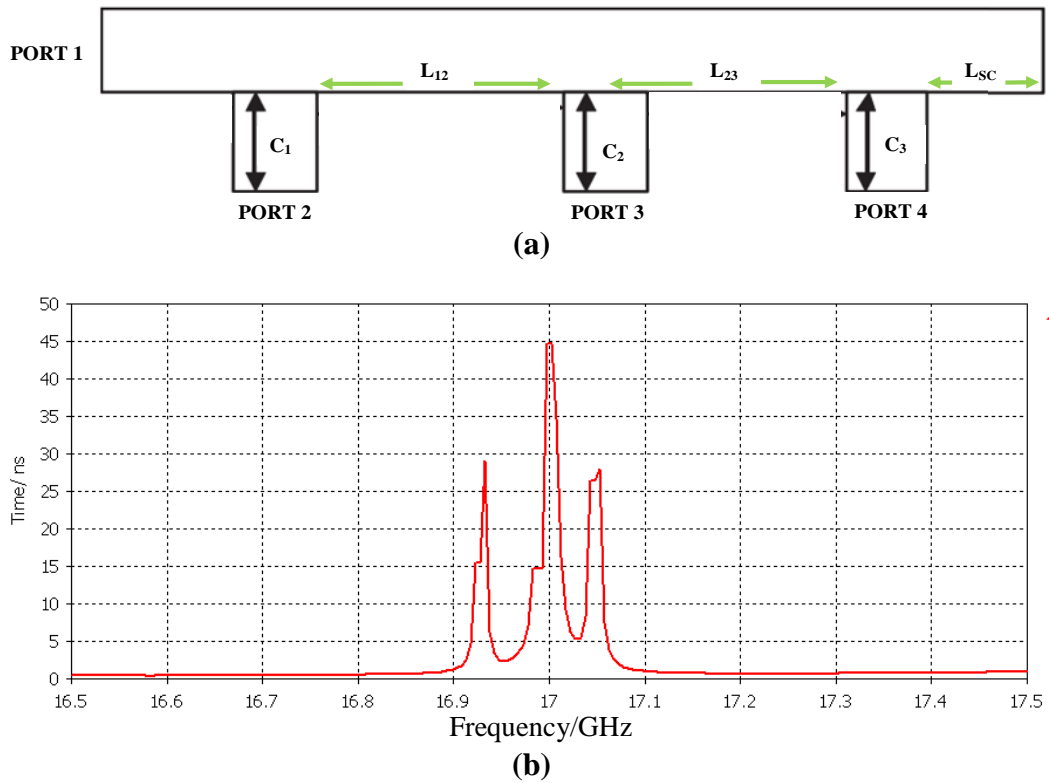


**Figure 4.3.** (a) Three-channel multiplexer with short circuits (b) Group delay response of the common port with short circuits for three-channel multiplexer.

- 2) After checking the physical realizability of computed lengths, channel filters are inserted into the manifold.
- 3) All distances between channel filters and the channel filters to manifold are optimized to achieve desired multiplexer specifications after replacing the short circuits with channel filters as illustrated in Figure 4.4.a. Common port return loss and transmission characteristics of each channel are shown in Figure 4.4.b,c. After optimization of the distances, they are computed as:  $L_{12}=36.43$  mm,  $L_{23}=16.3$  mm,  $L_{sc}=21.6$  mm,  $C_1=16.1$  mm,  $C_2=16.8$  mm,  $C_3=24.6$  mm.

The common port reflection gets worse at some frequencies and that mismatching deteriorates the passband flatness of the channel filters. Still, multiplexing with H-plane manifold seems to be a good candidate for the design when the common port mismatching effect is vanished.

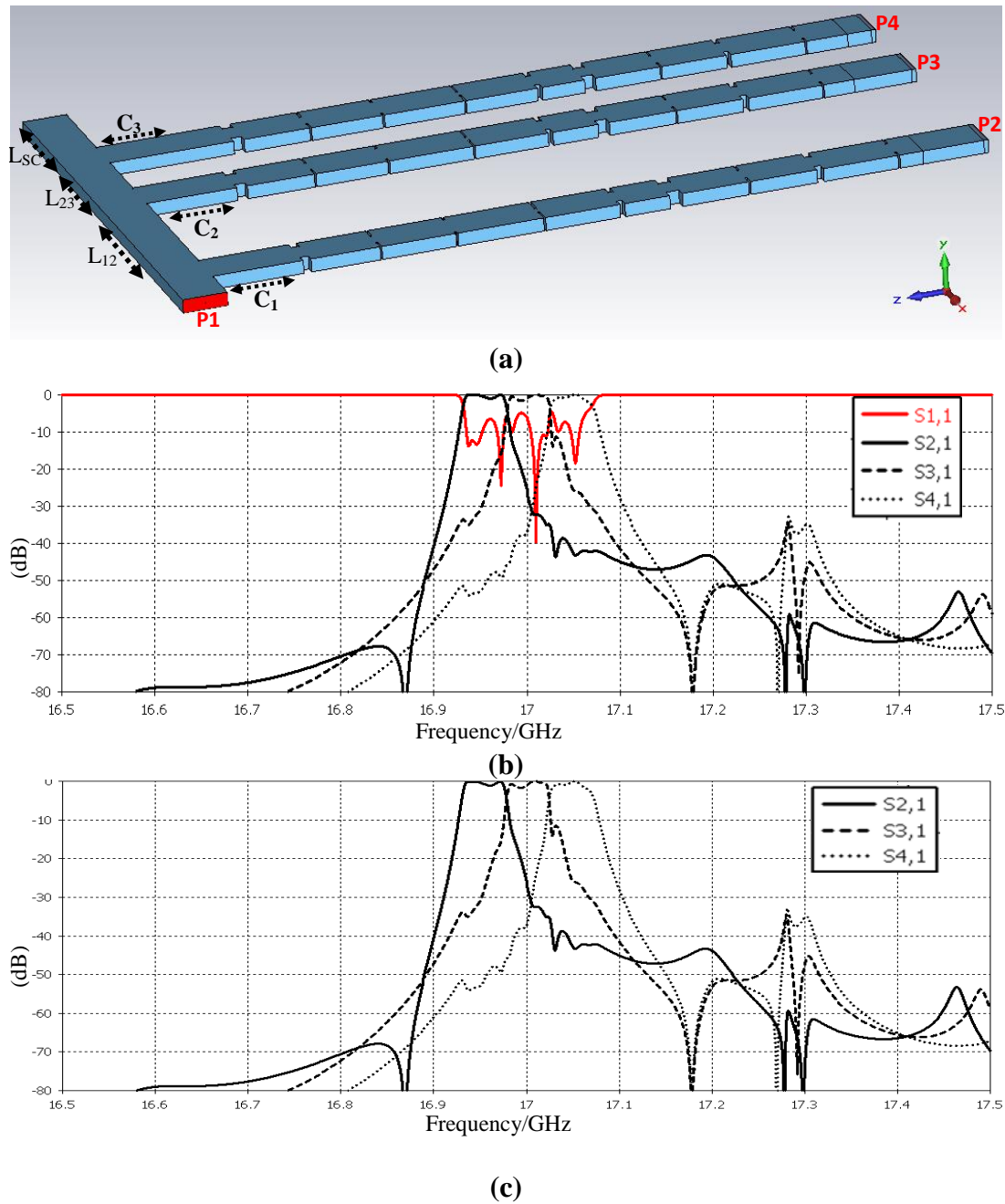


**Figure 4.4.** (a) View of three-band contiguous band multiplexer, (b) S-parameter results for the contiguous band MUX, (c) Transmission characteristic of each band.

This method is based on the observation of the group delay response at channels' center frequencies and the assumption of the short-circuited out of band response of the channel filters. For an illustration of the method, a waveguide triplexer is conceived step by step. However, multiplexer design may be too complex and cumbersome for the multi-channel implementations since the adjusting the group delay at certain frequencies may become very difficult. Also, derivations for forming the coupling matrix are necessary.

#### **4.1.2. Design of the Manifold with E-plane T-junctions**

Multi-furcated E-plane dividers are commonly employed for contiguous band multiplexer design since they are of wideband and low insertion loss characteristics and enable the design of very compact multiplexer [22]. The quadri-furcated E-plane divider is investigated and designed to construct compact and low-loss multiplexer network with four contiguous channels. Two different multiplexer structures with furcated E-plane divider are simulated and checked out whether desired electrical requirements can be fulfilled or not.

##### **4.1.2.1. Modified E-plane Manifold Design**

A design framework for the contiguous band E-plane manifold design is investigated to multiplex channel filters with minimum degradation on insertion loss and passband characteristics. For that purpose, triple band multiplexer with E-plane manifold structure is firstly designed, as shown in Figure 4.5.a. Since the full wave response of the channel filters have been calculated before, they are replaced by transmission and reflection coefficients and full-wave response of the multiplexer are optimized by tuning parameters of the E-plane manifold in CST DS, as depicted in Figure 4.5.b. This drastically reduces the computational effort to obtain length parameters [9]. Transmission and reflection responses are shown in Figure 4.5.c.

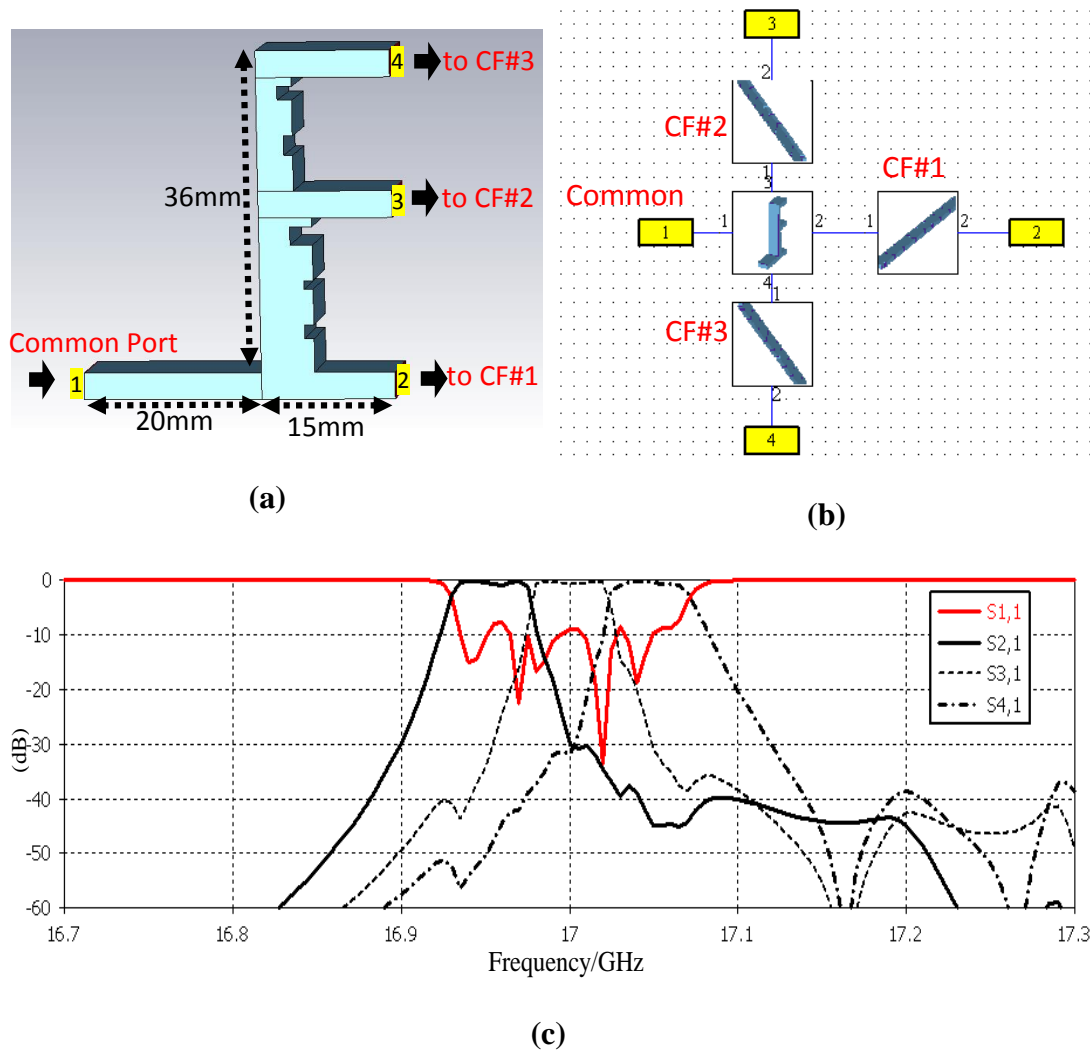


**Figure 4.5.** (a) Modified E-plane manifold, (b) Triple band multiplexer with filter-loaded manifold, (c) Transmission and reflection response

In multiplexer structure, the central frequencies for the channel filters CF#1, CF#2 and CF#3 are 16.954 GHz, 17 GHz and 17.046 GHz, respectively. All channels are of 40 MHz 1 dB bandwidth. Return loss at common port is above 10-dB. The contiguous band multiplexing can be performed by using some ridges at manifold arms to adjust the reactive loading effects of the adjacent channels without extra short-circuited section. Similarly, another triplexer structure is designed as shown in Figure 4.6. Common port return loss and passband transmission response of the

triplexer is illustrated in Figure 4.6.c. The central frequencies for the channel filters CF#4, CF#5 and CF#6 are 17.092 GHz, 17.138 GHz and 17.184 GHz, respectively.

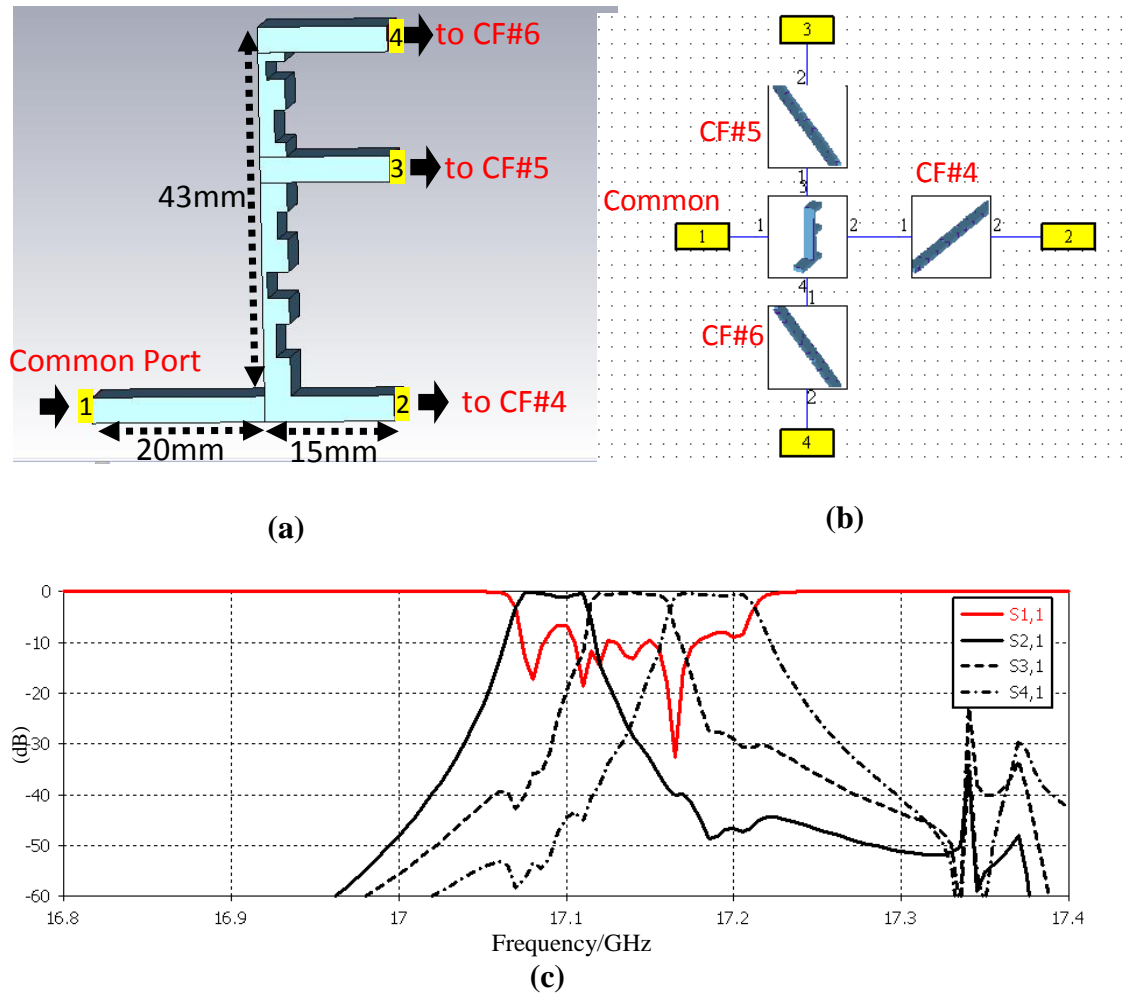


**Figure 4.6.** (a) Modified E-plane manifold, (b) Triple band multiplexer with filter-loaded manifold, (c) Transmission and reflection response

As number of the channels is increased, the structure becomes too complex and difficult to handle computationally. Hence, developing a systematic procedure for the multiplexer design is extremely hard and impractical.

## **4.2. Development of Design Framework for the Contiguous Band Multiplexer**

Novel design procedure is introduced for the design of H-plane contiguous band manifold-coupled multiplexer using optimization tools. A systematic methodology is based on the design of channel filters using circuit model extraction and H-plane manifold network with optimization process. The multiplexer is firstly analyzed in circuit level using a circuit-based solver and relevant lengths between channel filters and the lengths between each channel filters to manifold junction are determined meticulously to compensate for the channel interaction effects and mismatching effects for individual channels. Then, full-wave model is constructed and simulated using corresponding length values. This method has been applied for the design of six-channel contiguous band waveguide multiplexer. The achieved results obviously indicate the efficiency and validity of the proposed method.

### **4.2.1. Design Procedure of the H-Plane Manifold Coupled Multiplexer**

The channel filters may be multiplexed into the manifold through H-plane T-junctions. The channel filters are arranged in ascending order of center frequency from the short-circuited end. Rather than simulating the entire multiplexer structure in a full-wave simulator, discrete components are separated from the structure and each one is computed and performed individually [14]. For illustration of the design procedure, a six-channel multiplexer, operating in 16.95-17.18 GHz having eight-pole channel filters of 40 MHz 1-dB bandwidth spaced 46 MHz between each other has been conceived step by step. In order to obtain distance between channel filters and distance between each channel filters to manifold junction, as shown in Figure 4.7, a systematic design procedure is developed. It is mainly based on three steps.

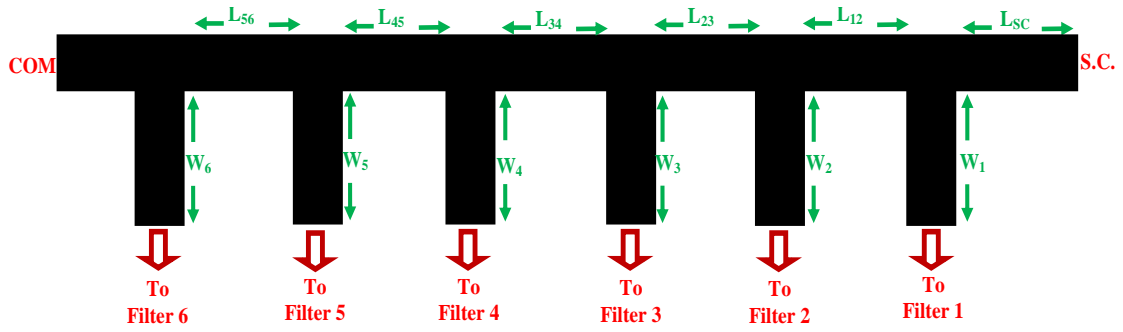


**Figure 4.7.** Layout of six-channel H-plane manifold

*Step 1.* The multiplexer network is designed using ideal transmission lines, H-plane T-junctions and channel filter blocks in circuit-based simulator as shown in Figure 4.8.

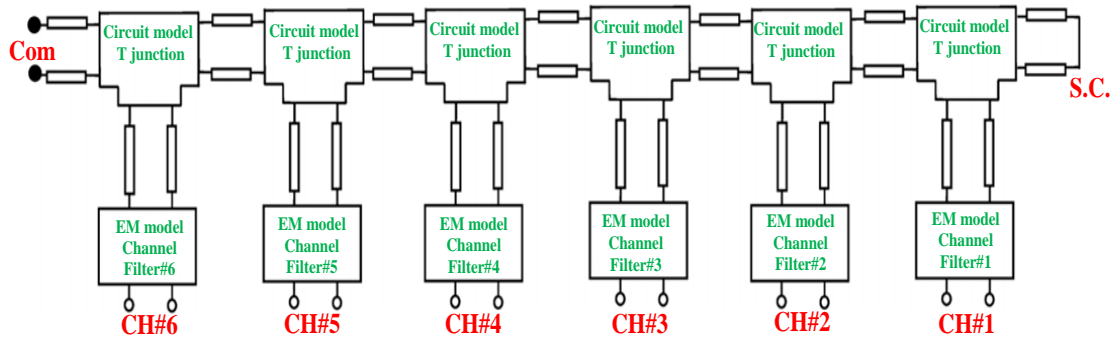


**Figure 4.8.** Circuit model of multiplexer with ideal transmission lines

As an initial point of the design, length between channel filters and length between each channel filter to manifold junction are taken as half of the guided wavelength [4]. It is assumed that the connection of the filters is of considerable influence on the field within the manifold in small input coupling cases. However, the coupling irises have a stronger effect in manifold field distribution.

As seen in Figure 4.9.a, optimal values of the manifold lengths should be determined to couple the required energy to the channel filters. For the efficient and faster optimization, all parameters are taken into consideration simultaneously in circuit level which takes shorter computation time compared to full-wave one and the

optimal values are computed for the circuit model. After parameter optimization process, channel transmission of the multiplexer is illustrated in Figure 4.9.b. Desired channel transmission performance is observed except small discrepancies and ripples in passband. Isolation between adjacent channels is above 25 dB at adjacent channel's center frequency.

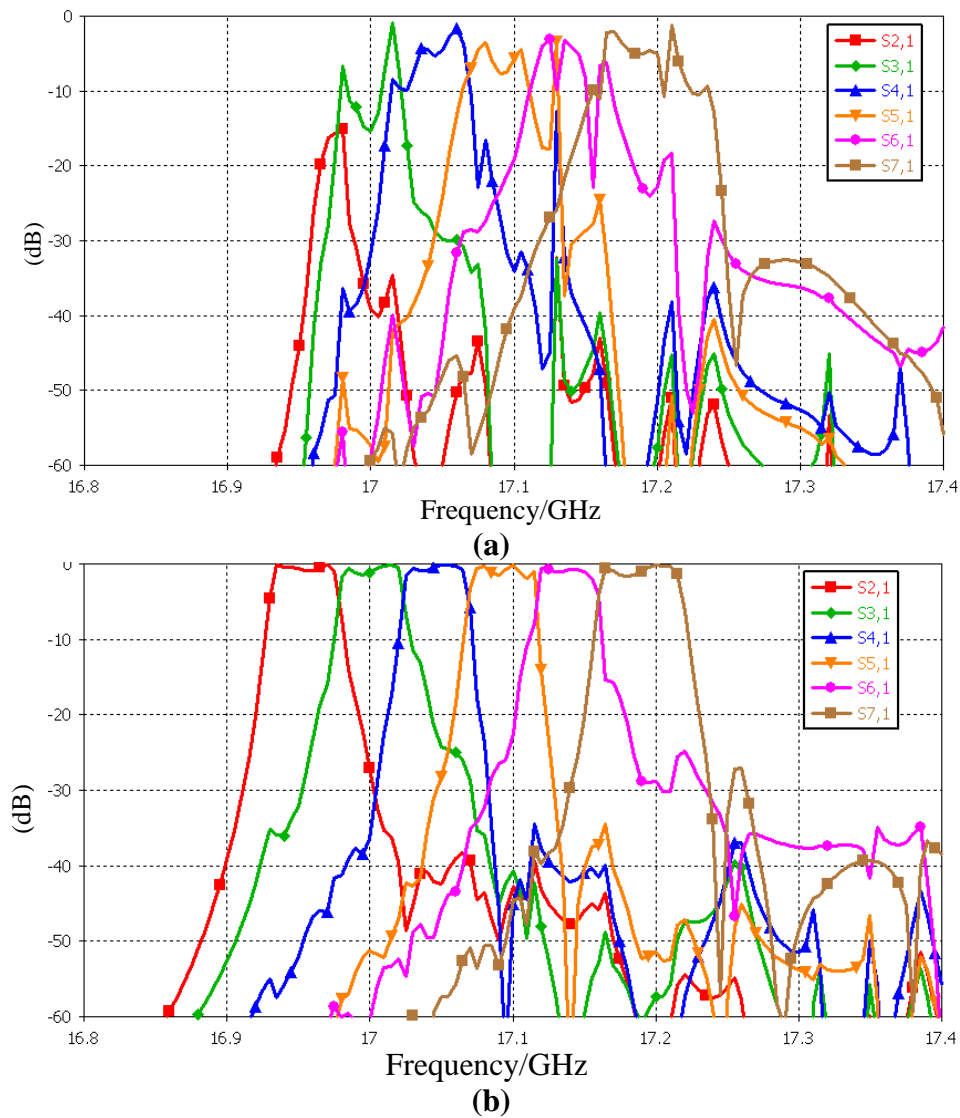


**Figure 4.9.** Channel transmission for the circuit model of MUX (a) before, (b) after optimization process.

**Step 2.** Ideal transmission lines and H-plane T-junctions are replaced with full wave equivalent blocks, as shown in Figure 4.10, obtained from full-wave simulator.



When model with equivalent blocks is placed, each block is individually simulated in full-wave solver, and S parameter blocks are interacted with each other in circuit-based solver. Simulation run-time and computer effort are reduced drastically in comparison with single full-wave simulation. Whilst full-wave simulation takes nearly two hours, circuit-based simulation takes about ten minutes.

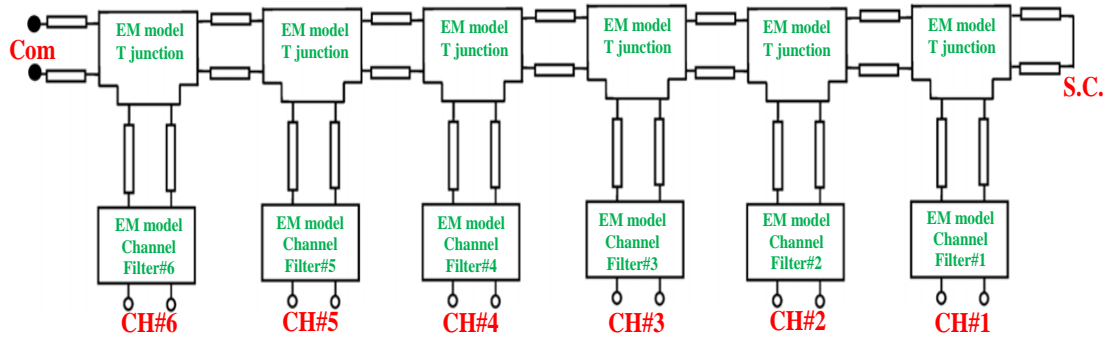


**Figure 4.10.** Circuit model of multiplexer with full-wave equivalent blocks.

The channel transmission of the six-channel contiguous band multiplexer is illustrated in Figure 4.11 after the optimization process by exploiting efficient numerical optimization tools.

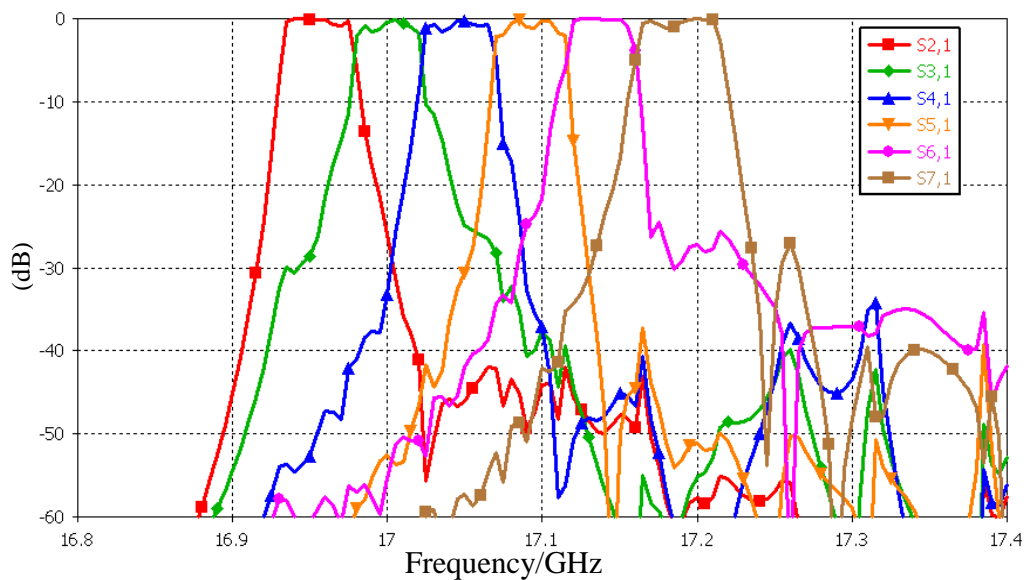


**Figure 4.11.** Channel transmission of the MUX with full-wave equivalent blocks.

**Step 3.** Length values acquired from circuit optimization procedure provides a good initial point while conceiving actual full-wave structure of the multiplexer. 3-D view of the six-channel multiplexer is illustrated in Figure 4.12. In order to compensate for the inter-channel reactive loading effects, metal posts are placed at the input of the channels and loading effect of H-plane T- junctions is tuned by inserting the reactive tuning elements. Hence, desired multiplexer response is achieved with lower common port return loss.

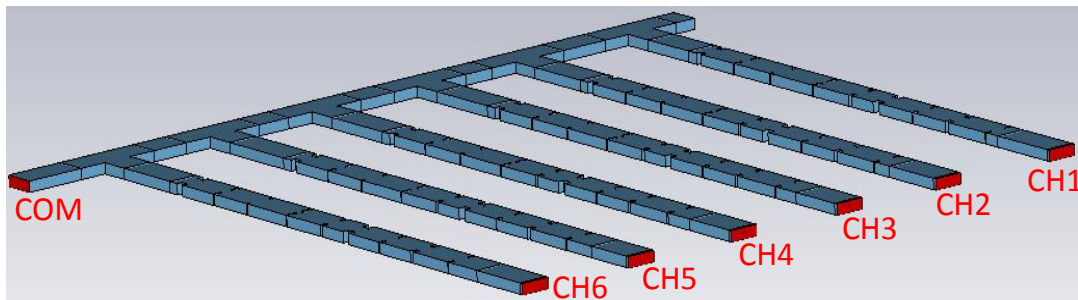


**Figure 4.12.** Three-dimensional view of six-channel multiplexer.

In order to remove the discrepancies in full-wave design, final fine-tuning process is required to get the desired multiplexer response, as shown in Figure 4.13.a. Channel to channel isolation is above 25 dB, return loss is about 10 dB nearly whole band with 0.8 dB passband ripples, as shown in Figure 4.13.b which is of curves of passband responses of the channels with more detail.

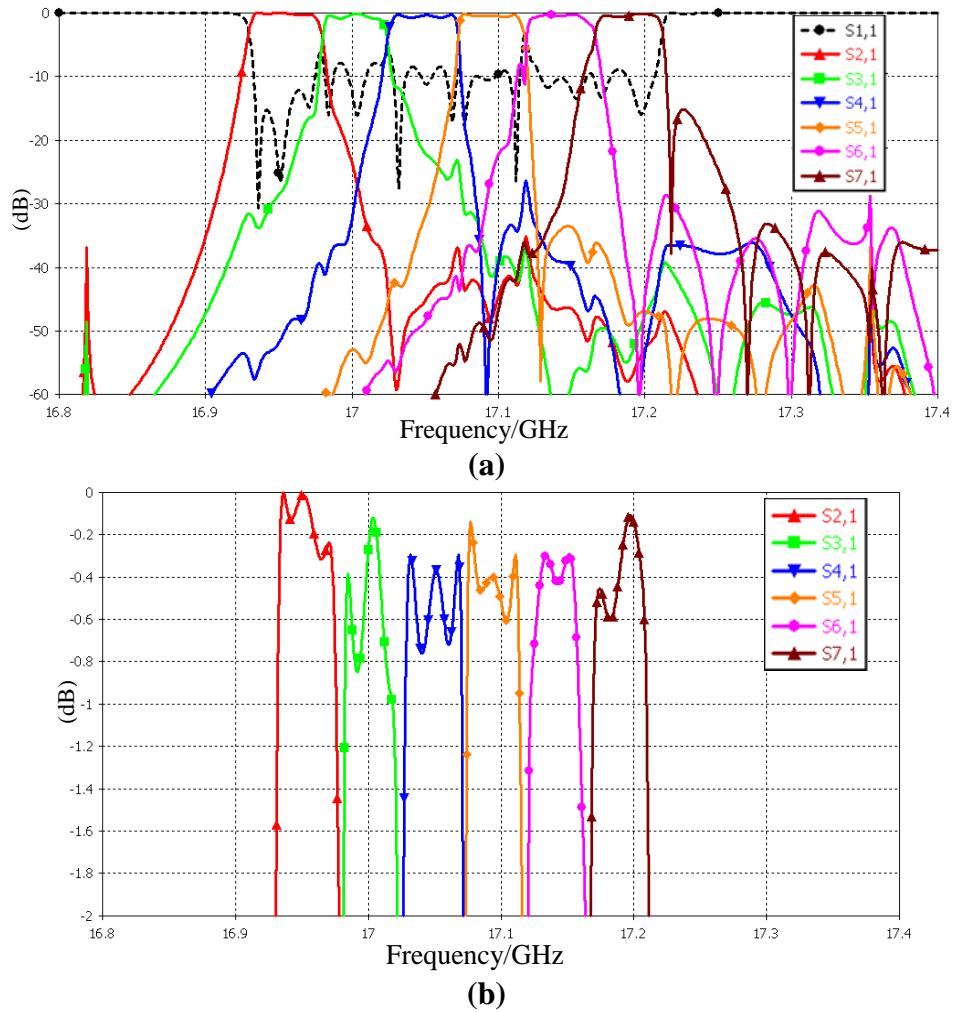


**Figure 4.13.** (a) Channel transmission of the multiplexer, (b) passband of the channels.

Corresponding physical dimensions of the manifold junction after the optimization of the circuit model, hybrid circuit-EM model and full-wave model are given in Table 4.1 and Table 4.2. Parameter values are in good agreement with each other as expected except small differences for some parameters.

**Table 4.1.** Gap distance values (in millimeters) for H-plane manifold

	<i>W1</i>	<i>W2</i>	<i>W3</i>	<i>W4</i>	<i>W5</i>	<i>W6</i>
<b>Circuit</b>	19.02	21.29	26.11	24.99	21.93	21.57
<b>Hybrid</b>	19.24	21.73	24.17	23.99	25.88	21.93
<b>Full-wave</b>	16.10	21.47	25.60	24.49	27.16	24.87

**Table 4.2.** Resonator length values (in millimeters) for H-plane manifold

	<i>L12</i>	<i>L23</i>	<i>L34</i>	<i>L45</i>	<i>L56</i>	<i>Lsc</i>
<b>Circuit</b>	13.69	11.11	13.31	15.37	10.06	7.60
<b>Hybrid</b>	17.84	12.10	12.13	12.47	12.61	8.30
<b>Full-wave</b>	17.37	15.15	12.60	10.49	11.90	7.69

Bandwidth of the channel filters for the prescribed and achieved designs are listed in Table 4.3. Though bandwidth deviations are observed, desired filtering and rejection operations are performed for the implementation.

**Table 4.3.** Channel performances of the multiplexer

<b>Channel Numbers</b>	<b>Prescribed BW<sub>IL&lt;1 dB</sub> Specifications</b>	<b>Achieved BW<sub>IL&lt;1 dB</sub> Specifications</b>
# 1	16.934-16.974 (40 MHz)	16.933-16.975 (42 MHz)
#2	16.980-17.020 (40 MHz)	16.981-17.019 (38 MHz)
#3	17.026-17.066 (40 MHz)	17.028-17.069 (41 MHz)
#4	17.072-17.112 (40 MHz)	17.074-17.114 (40 MHz)
#5	17.118-17.158 (40 MHz)	17.122-17.159 (37 MHz)
#6	17.166-17.206 (40 MHz)	17.169-17.209 (40 MHz)
Ch. to ch. isolation (dB)	>25	>25

During the optimization process, 12 variables are involved in intensive computation simultaneously. Furthermore, the first three inductive iris elements of each filter is optimized sequentially for the improvement of the multiplexer's response in each

channel. They are of well consistency with each other except small differences due to the effect of H-plane T-junction, and also different from half of the guided wavelength since there exists unknown loading effects of the input irises on the adjacent transmission lines [16]. Input coupling irises have stronger effect along the manifold. Because of that, it is needed to optimize the distances between channel filters and manifold junctions meticulously. Otherwise, the required coupling energy may not be achieved for the channel filters [11]. Furthermore, contiguous band six-channel multiplexer employing standard WR75 waveguide ( $a=19.05\text{mm}$ ,  $b=9.525\text{mm}$ ) are implemented in X-band so as to inspect the validity and adaptability of the proposed design methodology. For that purpose, a six-channel waveguide multiplexer which is operating in 11-12 GHz having five-pole channel filters of 80 MHz 1-dB bandwidth spaced 160 MHz between each other is designed as illustrated in Figure 4.14.

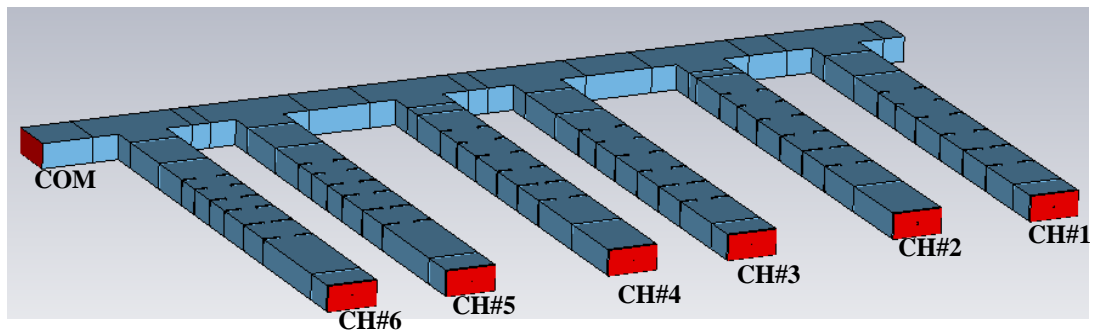


**Figure 4.14.** Three-dimensional view of six-channel multiplexer in X-band.

Starting from the synthesis of the channel filters, six-channel contiguous band multiplexer is constructed by applying the proposed design methodology. Tuned circuit model is firstly conceived for the channel filter whose center frequency is 11.32 GHz and 1-dB bandwidth 80 MHz and then full-wave simulation with obtained lengths are run. Scattering parameter curves of the filter for the circuitual and full-wave computations are illustrated in Figure 4.15. Both results are well-consistent with each other. Also, all design parameters are listed in Table 4.4.

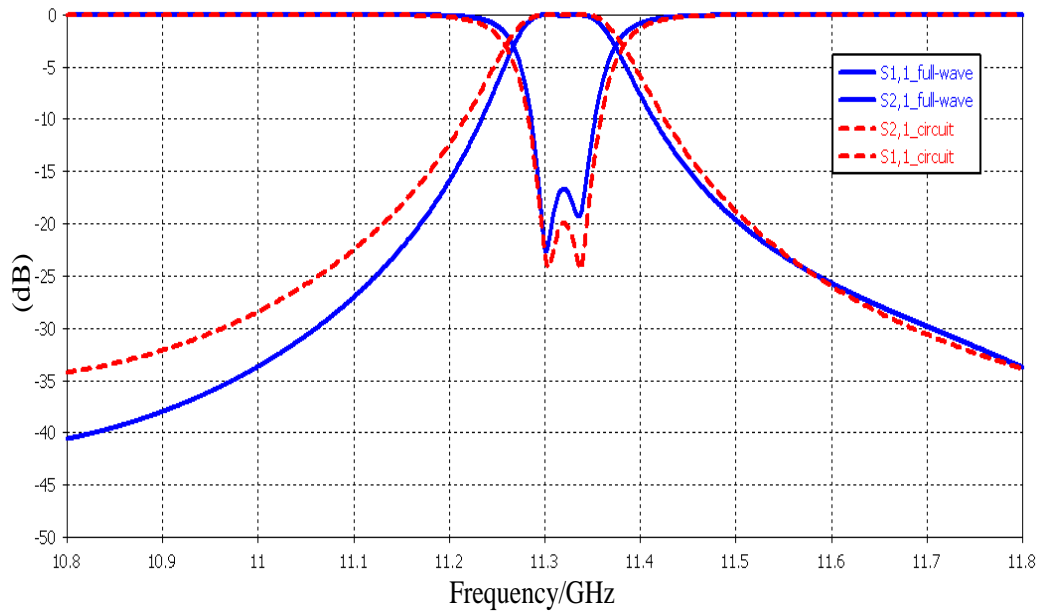


**Figure 4.15.** Transmission and reflection response of the filter.

**Table 4.4.** Parameter values (in millimeters) for the six fifth-order channel filter

	<i>Ch# 1</i>	<i>Ch#2</i>	<i>Ch#3</i>	<i>Ch# 4</i>	<i>Ch#5</i>	<i>Ch# 6</i>
$f_{\text{center}}$	11.0 GHz	11.16 GHz	11.32 GHz	11.48 GHz	11.64 GHz	11.80 GHz
<b>L1</b>	13.911	13.855	13.759	13.495	10.844	10.577
<b>L2</b>	16.130	15.900	15.850	15.413	12.769	12.432
<b>L3</b>	19.537	18.827	17.880	17.375	12.340	11.936
<b>L4</b>	18.078	17.646	17.144	16.720	16.413	16.074
<b>L5</b>	18.289	17.862	17.357	16.947	16.527	16.100
<b>d1</b>	10.865	11.034	10.731	10.348	8.499	8.439
<b>d2</b>	12.796	12.325	11.965	11.649	9.379	9.282
<b>d3</b>	9.150	8.716	8.670	8.602	6.393	6.044
<b>d4</b>	8.050	7.850	7.836	7.630	6.108	5.808
<b>d5</b>	3.250	3.250	3.322	3.234	2.941	2.913
<b>d6</b>	6.570	6.269	6.186	5.944	5.922	6.011

Transmission responses of each channel are illustrated in Figure 4.16 at the end of the *Step1*. Desired multiplexing scheme is achieved by using ideal component in circuit model.

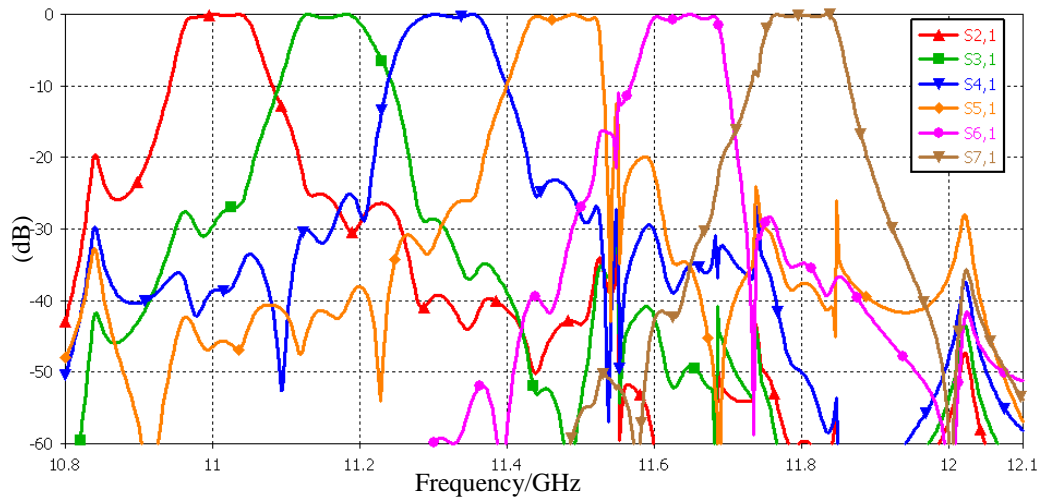


**Figure 4.16.** Channel transmission of the multiplexer (Step1).

At the end of the *Step2*, ideal models are replaced with the full-wave ones and passband response of the multiplexer is illustrated in Figure 4.17. Small changes occur comparing with the circuit models.

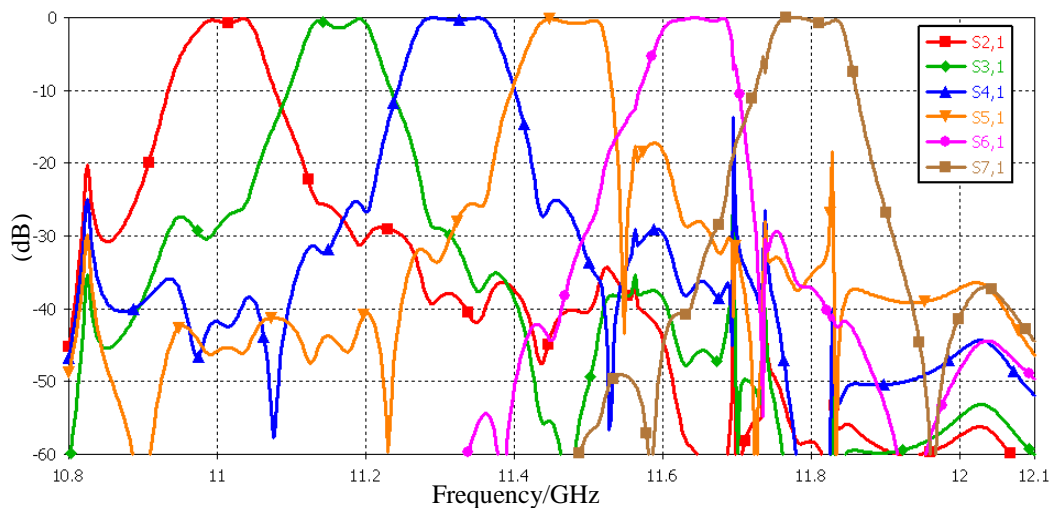


**Figure 4.17.** Channel transmission of the multiplexer (Step2).

At the end of the *Step3*, transmission responses of each channel are illustrated in Figure 4.17. Since interaction effects between channel filters are in higher level in comparison with the miniaturized one, the performance of the second and fourth channels are deteriorated and ripples in passband increases.

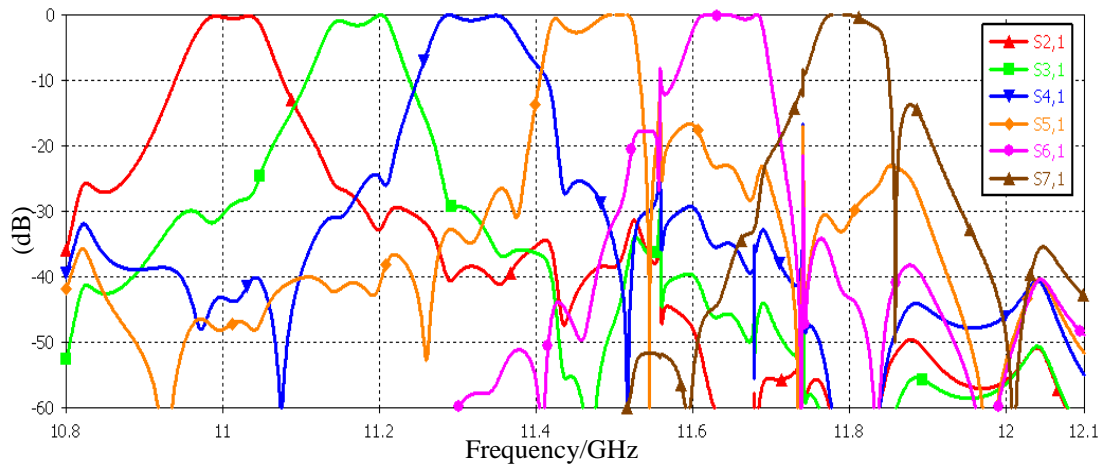


**Figure 4.18.** Channel transmission of the multiplexer (Step3).

**Table 4.5.** Gap distance values (in millimeters) for H-plane manifold

	<i>W1</i>	<i>W2</i>	<i>W3</i>	<i>W4</i>	<i>W5</i>	<i>W6</i>
<b>Circuit</b>	24.51	5.31	23.38	7.47	24.85	23.77
<b>Hybrid</b>	24.75	5.46	24.36	9.42	24.07	24.98
<b>Full-wave</b>	26.37	6.50	25.50	8.81	26.51	26.52

**Table 4.6.** Resonator length values (in millimeters) for H-plane manifold

	<i>L12</i>	<i>L23</i>	<i>L34</i>	<i>L45</i>	<i>L56</i>	<i>Lsc</i>
<b>Circuit</b>	14.52	23.69	11.42	20.51	8.65	9.41
<b>Hybrid</b>	14.74	25.81	8.74	24.16	7.42	8.60
<b>Full-wave</b>	15.19	26.95	6.21	25.25	6.32	8.37



## **CHAPTER V**

### **ANALYSIS OF THE SURFACE ROUGHNESS EFFECT ON FILTERING PERFORMANCE AND EXPERIMENTAL ACTIVITIES**

The surface roughness effect on narrowband and highly-selective waveguide filters are analyzed and consequences, achievements are presented comprehensively together with realization procedure and experimental results of the channel filter in this section. A novel design procedure involving the surface roughness effect is explained with full wave and circuit level modeling analysis of the roughness effect. Also, surface roughness profile of the waveguide filter walls are measured via surface profilometer and design procedure is modified properly by taking it into account. Computed and measured scattering parameter results are compared with each other. The scattering parameters of a two-port waveguide filter is measured with the network analyzer in which senses the incident and reflected waves at all ports by carrying out the Thru-Reflect-Line (TRL) calibration. Defining the correct reference plane is extremely crucial for the measurement accuracy and deleterious effects of the transitions and cable sections on the performance of filter under test (FUT) must be removed by characterizing the appropriate standards for the measurement [80]. The TRL calibration is mostly preferred for two-port calibration so as to exclude systematic effects and measure the S-parameters of the FUT solely.

## 5.1.TRL Calibration Procedure

TRL calibration procedure is illustrated in Figure 5.1 with all stages of it. R1 and R2 denote the reference planes of the FUT whilst P1 and P2 denote the measurement planes in Figure 5.1.a. The properties of the Thru-Reflect-Line standards can be summarized as follows [80]:

- Thru is of zero lengths and generally achieved by connection of two error boxes directly, as shown in Figure 5.1.b. For the case of its non-zero length, it must be of different length from Line.
- For the Reflect standard, it can be used any appropriate element having high reflector property, as shown in Figure 5.1.c.
- Line must have the same characteristic impedance and propagation constant with the Thru standard, as shown in Figure 5.1.d. For the sake of more accurate measurement, the length of the line is chosen within quarter of the wavelength. There must the phase difference between Line and Thru ranging from  $20^\circ$  to  $160^\circ$ . For wideband measurements, it entails different line lengths to fulfill that phase requirements.

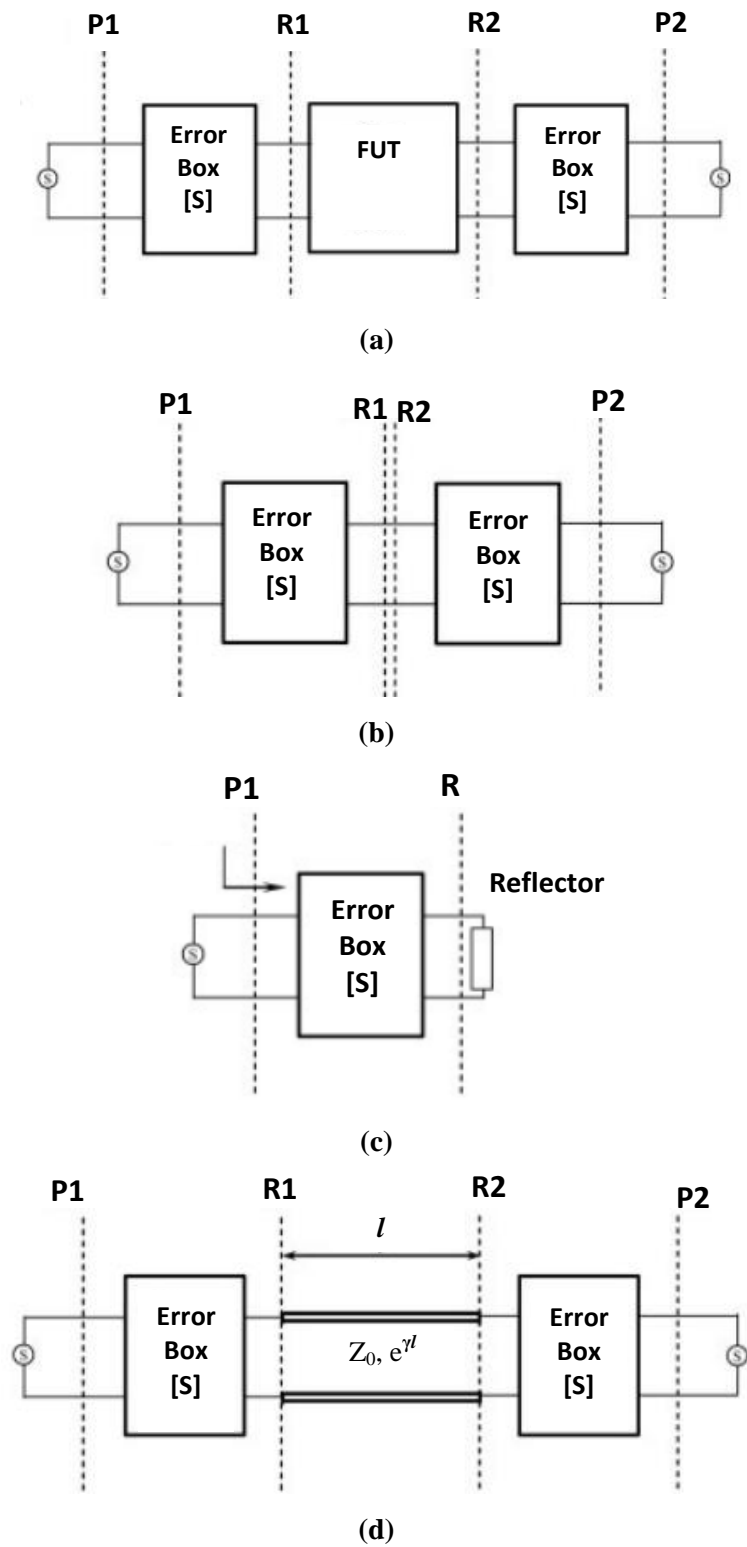


**Figure 5.1.** TRL calibration procedure (a) Error model with DUT for TRL calibration, (b) Thru connection, (c) Reflect connection, (d) Line connection

In order to achieve the FUT performance, shown in Figure 5.1.a, error boxes defined at both sides of the FUT are characterized and error-corrected results are acquired at the end of excluding error inclusions [81]. The S-parameter matrices of Thru [ $S^T$ ], Reflect [ $S^R$ ] and Line [ $S^L$ ] are written and related parameters are defined as follows:

$$S^T = \begin{bmatrix} S_{11}^T & S_{12}^T \\ S_{21}^T & S_{22}^T \end{bmatrix} \quad S^R = \begin{bmatrix} S_{11}^R & S_{12}^R \\ S_{21}^R & S_{22}^R \end{bmatrix} \quad S^L = \begin{bmatrix} S_{11}^L & S_{12}^L \\ S_{21}^L & S_{22}^L \end{bmatrix}$$

Considering the signal flow graph of the Line, each matrix element of the [ $S^T$ ], [ $S^R$ ] and [ $S^L$ ] can be obtained as follows:

$$S_{11}^R = S_{11} + \frac{S_{12}^2 \Gamma_L}{1 - S_{22} \Gamma_L}$$

$$S_{11}^T = S_{11} + \frac{S_{22} S_{12}^2 \Gamma_L e^{-2\gamma l_1}}{1 - S_{22} e^{-2\gamma l_1}}$$

$$S_{12}^T = \frac{S_{12}^2 \Gamma_L e^{-\gamma l_1}}{1 - S_{22}^2 e^{-2\gamma l_1}}$$

$$S_{11}^L = S_{11} + \frac{S_{22} S_{12}^2 \Gamma_L e^{-2\gamma l}}{1 - S_{22} e^{-2\gamma l}}$$

$$S_{12}^L = \frac{S_{12}^2 \Gamma_L e^{-\gamma l}}{1 - S_{22}^2 e^{-2\gamma l}}$$

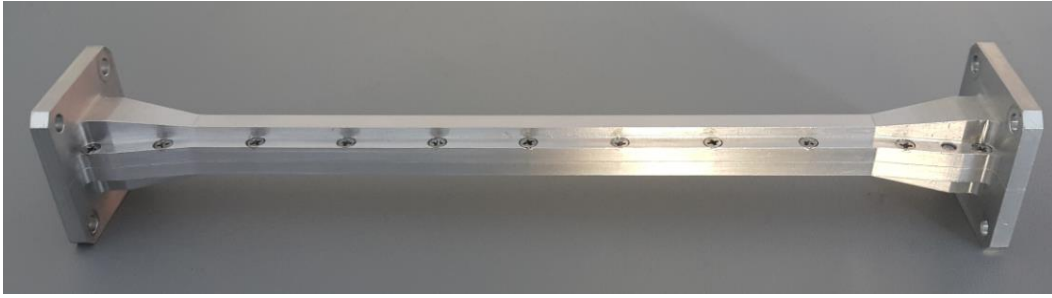
Where  $\gamma$  represents propagation constant,  $l$  and  $l_1$  are lengths of Line and Thru. [ $S$ ] matrix is obtained by solving these five equations simultaneous and [ $S$ ] matrix is completely known.

$$S = \begin{bmatrix} S_{11} & S_{12} \\ S_{21} & S_{22} \end{bmatrix}$$

Once S-parameters of error boxes are known, it is possible to have the S-parameters of the FUT by applying straightforward matrix operations after measuring the S-parameter at P1 and P2 point in Figure 5.1.a.

## 5.2. Analysis of the Surface Roughness Effect with Realization and Measurement of the Channel Filter

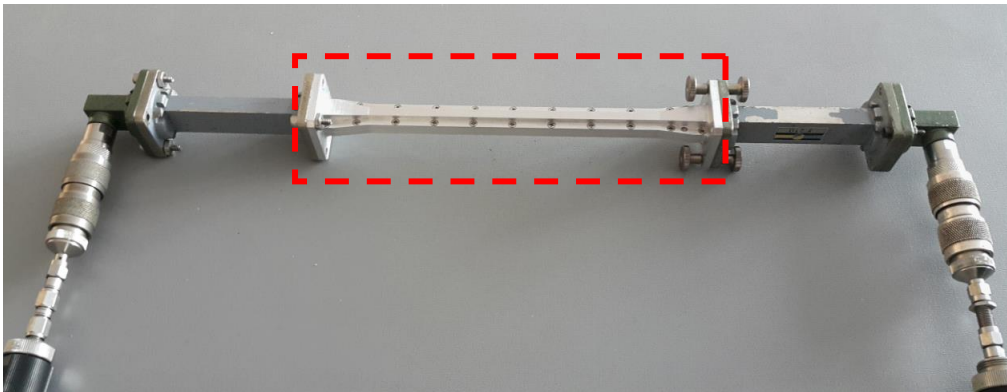
The channel filter was fabricated in aluminum with smooth transition sections at input and output of the filter so as to mate with the standard WR62 adapter ( $a=15.8$  mm,  $b=7.9$  mm) for the ease of measurement, as illustrated in Figure 5.2.a. Vertical-cut view of it, whose total length is 130mm, is also illustrated in Figure 5.2.b. TRL (Thru, Reflect, Line) calibrated measurement setup for the S-parameters of the filter is also shown in Figure 5.2.c. Measured and computed S-parameters for the filter are illustrated in Figure 5.3. Taking the measurement results into consideration, 23 MHz shift in frequency is encountered together with 4.2 dB insertion loss, which is unexpectedly high in comparison with simulation result while trend of the channel bandwidth and skirt selectivity is in good agreement with each other. Due to the long fabrication duration since it entails sensitive milling process, theoretical reasons for the unexpected shift in measurement is investigated considering that this case is stemming from fabrication imperfections and irregularities on conductor surfaces. In order to understand the discrepancy and account for the reason why insertion loss of measured filter is much higher than expected one, effect of the surface roughness of the waveguide walls on filtering performance is analyzed by applying Huray's approximation for the surface roughness based on hemispherical snowball model for the channel filter. Furthermore, a new circuit equivalent for the representation of the surface roughness of the narrowband waveguide filters is developed.



(a)



(b)



(c)

**Figure 5.2.**(a) Perspective, (b) Vertical-cut view of the fabricated channel filter, (c) Illustration of TRL measurement setup with fabricated filter.

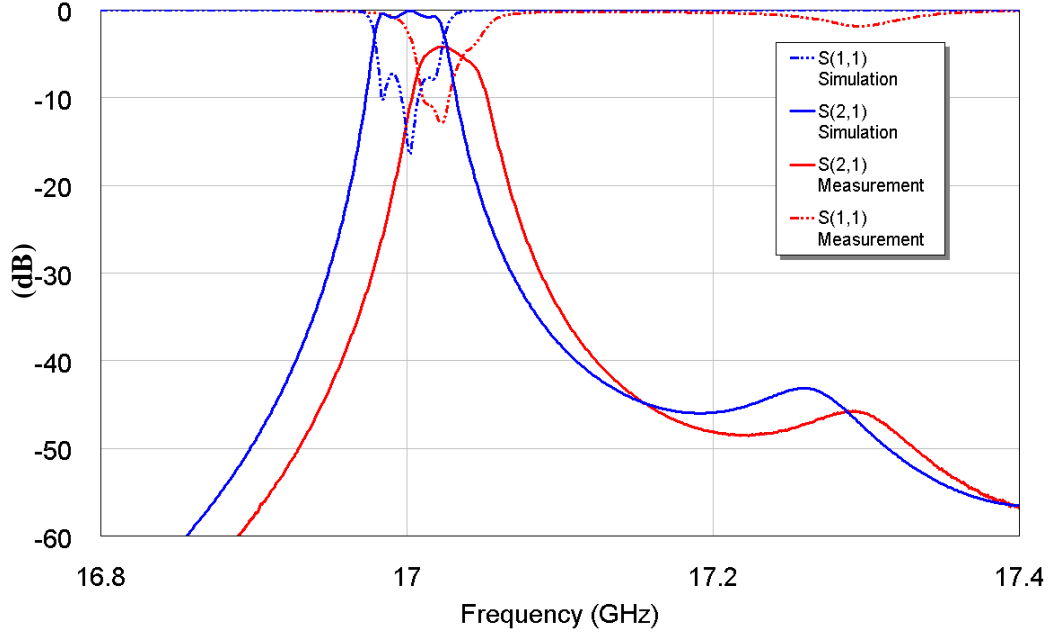


**Figure 5.3.** Measured and simulated S-parameters for the channel filter.

Influence of the rough surface on power absorption at microwave frequencies is evaluated and explanatory formulations are presented for the Huray approach in [82]-[83]. It assumes that surface roughness may be characterized as spherical snowballs on flat conductor surface and it increases power absorption, insertion loss considerably compared to the smooth surface case. Analytical model formulation for surface roughness is derived as follows in (5.1) [82].

$$H_{rough}(f) = \frac{P_{rough}}{P_{smooth}} = 1 + \frac{3}{2} \sum_1^n \frac{N_i 4\pi a_i^2}{A_{hex}} \left[ 1 + \frac{\delta(f)}{a_i} + \frac{\delta(f)^2}{2a_i^2} \right]^{-1} \quad (5.1)$$

$P_{rough}$  is power loss for  $A_{hex}$ , area of rough surface,  $P_{smooth}$  is power loss for ideal smooth surface and  $\delta$  is skin depth. Huray model states that there may be  $n$  spherical bumps and  $N_i$  spheres whose radius is  $a_i$  in each rough area  $A_{hex}$ .

Approximate calculation of the correction factor for the power loss due to the spherical nodules ( $K_{SR}$ ) is expressed as (5.2) [82] :

$$K_{SR}(f) \approx 1 + 84 \left[ \frac{\pi r^2}{A_{flat}} \right] \left[ 1 + \frac{\delta(f)}{a_i} + \frac{\delta(f)^2}{2a_i^2} \right]^{-1} \quad (5.2)$$

Stack-up snowball model for the surface roughness is illustrated in Figure 5.4.

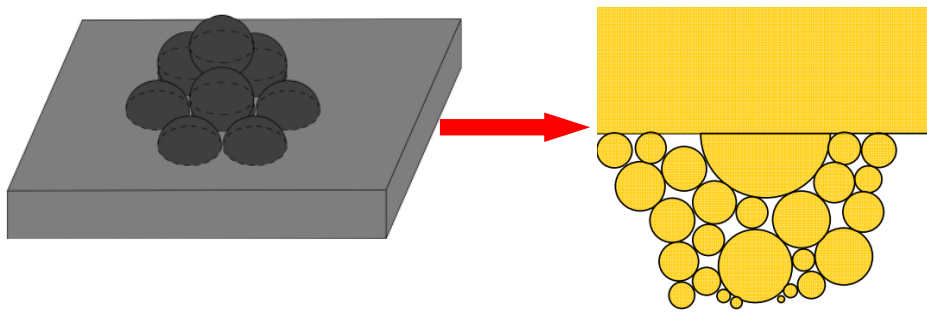


**Figure 5.4.** Snowball model for surface irregularities in cross section [65].

Moreover, the spherical nodules on flat conductor surface increase the reactance of the structure and causes drastic deterioration on passband response [71]. Therefore,  $R_{rough}$ , representing the cause of power loss, and  $L_{rough}$ , representing the cause of the reactance increment, are inserted into the circuit model of the channel filter and compound conductor walls including Huray model are superseded with smooth ones, as illustrated in Figure 5.5.a.



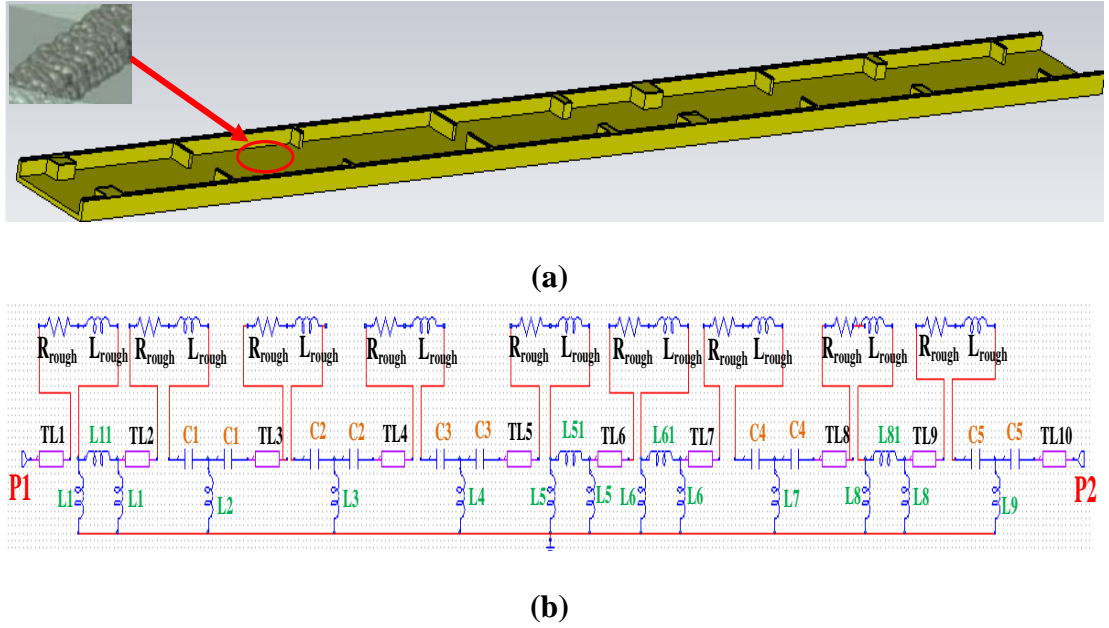


**Figure 5.5.** (a) Cut-view of the channel filter with rough surfaces, (b) circuit schematic of the channel filter including  $R_{\text{rough}}$  and  $L_{\text{rough}}$ .

Effect of the surface roughness on single channel performance is investigated by changing the radius of the spherical snowballs in hexagonal cross section using macros tool in CST MWS for Huray roughness model. In circuit model of smooth filter as given in Figure 5.5.b,  $R_{\text{rough}}$ , representing power loss and  $L_{\text{rough}}$ , representing reactive component are inserted and corresponding  $R_{\text{rough}}-L_{\text{rough}}$  values are determined by comparing the transmission and reflection curves in circuit level computation via CST DS with the full-wave one. Considering the surface roughness effect causing frequency shift and degradation in measured transmission characteristic, it is concentrated on improving the filter response by re-adjusting the design parameters such as resonator lengths and iris gap distances with the existence of surface roughness values determined. As radius of the sphere is 0.5um,  $R_{\text{rough}}$  and  $L_{\text{rough}}$  are determined as 2.2ohm and 27pH, as shown in Figure 5.6.a. As radius of the sphere is 1um,  $R_{\text{rough}}$  and  $L_{\text{rough}}$  are determined as 2.5ohm and 40pH, respectively, as shown in Figure 5.6.b. As radius of the sphere is 2um,  $R_{\text{rough}}$  is 3.9ohm and  $L_{\text{rough}}$  is 47pH, as illustrated in Figure 5.6.c. It is obviously seen that they are in good agreement with each other.

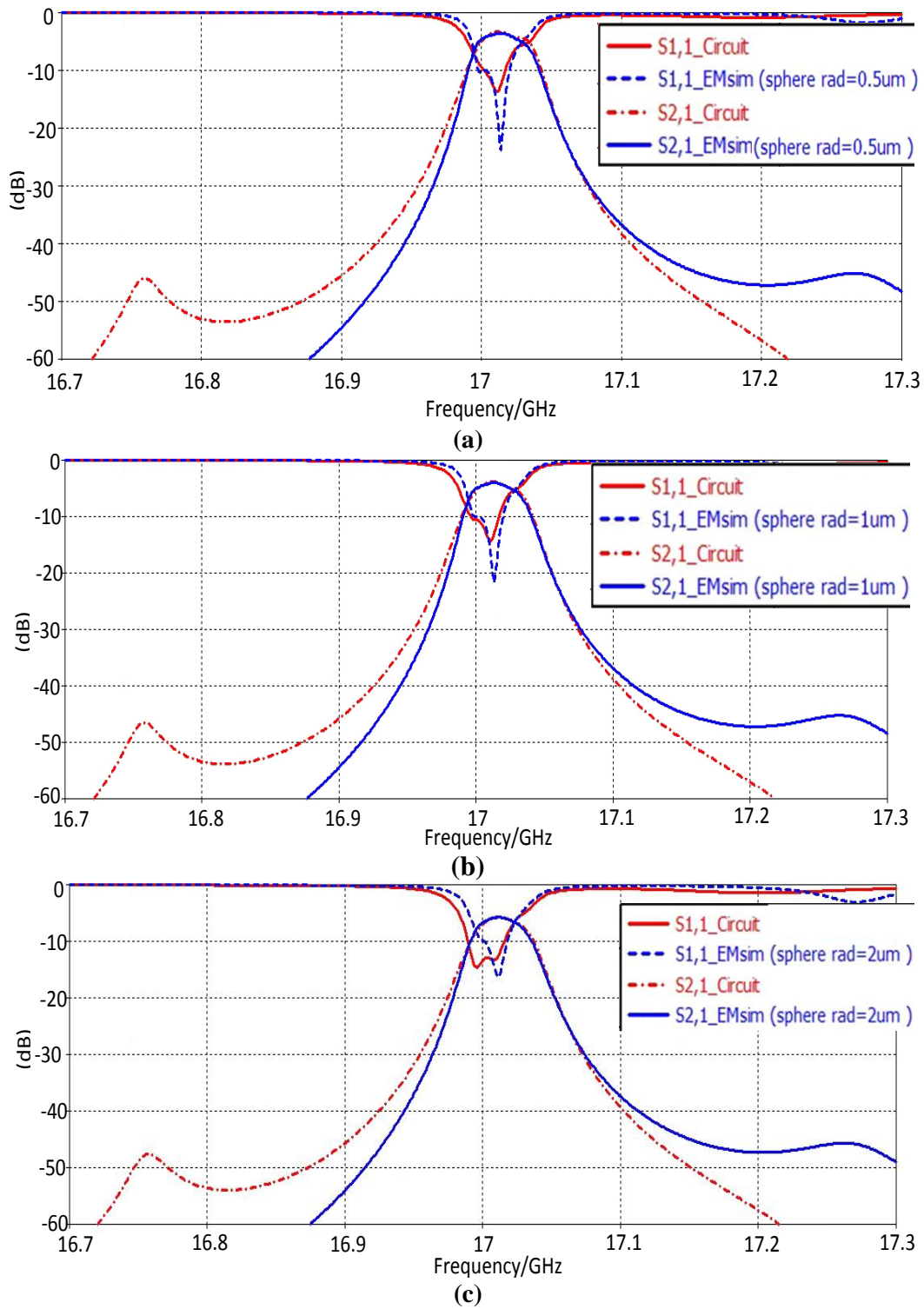


**Figure 5.6.** Transmission and rejection characteristics of the channel filter in circuit level and full-wave simulator for (a) radius of spherical roughness: 0.5um, (b) radius of spherical roughness: 1um, (c) radius of spherical roughness: 2um

The filter response is firstly optimized in circuit level and then by exploiting determined parameters giving optimum results full-wave response is computed. Then, gap distances, iris thicknesses and resonator lengths are fine-tuned as  $R_{\text{rough}}=2.67\text{ohm}$  and  $L_{\text{rough}}=43\text{ pH}$ , as shown in Figure 5.7.a. Optimized results are illustrated in Figure 5.7.b. Insertion loss in passband of the filter is obtained as 2.35 dB and 23 MHz shift in center frequency is vanished by adjusting the center frequency as 17 GHz.

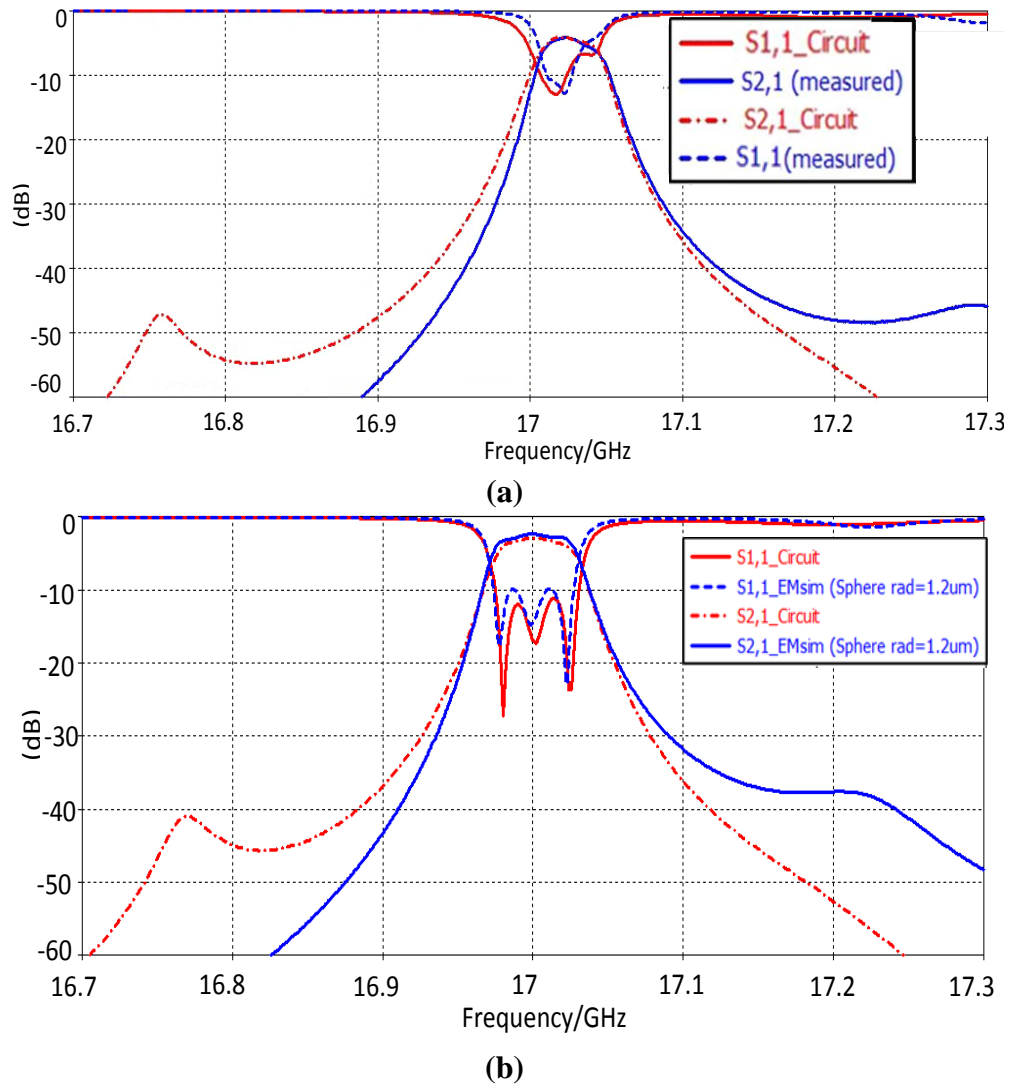


**Figure 5.7.**(a) Measured and simulated response with surface roughness, (b) Optimized transmission and rejection characteristics of the channel filter in circuit level and full-wave EM simulation in the existence of surface roughness

Considering measured surface roughness values listed in Table 5.1, it is clearly seen that determined surface roughness value is very close to roughness profile measurements of the conductor surface.

**Table 5.1.** Measured surface roughness values at randomly selected points on walls

<i>Measured Surface Roughness Values (in <math>\mu\text{m}</math>) at Random Points</i>						
<b>WALLS</b>	<b>Point#1</b>	<b>Point#2</b>	<b>Point#3</b>	<b>Point#4</b>	<b>Point#5</b>	<b>Point#6</b>
<b>Top</b>	1.25	1.35	1.30	1.55	1.44	1.38
<b>Bottom</b>	1.19	1.27	1.28	1.39	1.42	1.27
<b>Left Side</b>	0.79	0.88	0.92	0.44	0.45	0.48
<b>Right Side</b>	0.77	0.38	0.84	0.42	0.39	0.47

In order to illustrate the validity of the design procedure involving surface roughness effect, one more channel filter is conceived and realized by applying the proposed design procedure. First of all, surface roughness profile of the conductor surface of the material is measured as shown in Figure 5.8 and sphere radius for the spherical nodules on conductor surface is taken as 0.5 $\mu\text{m}$  at design stage. Resonator lengths and gap distances of the iris are optimized with respect to this roughness value

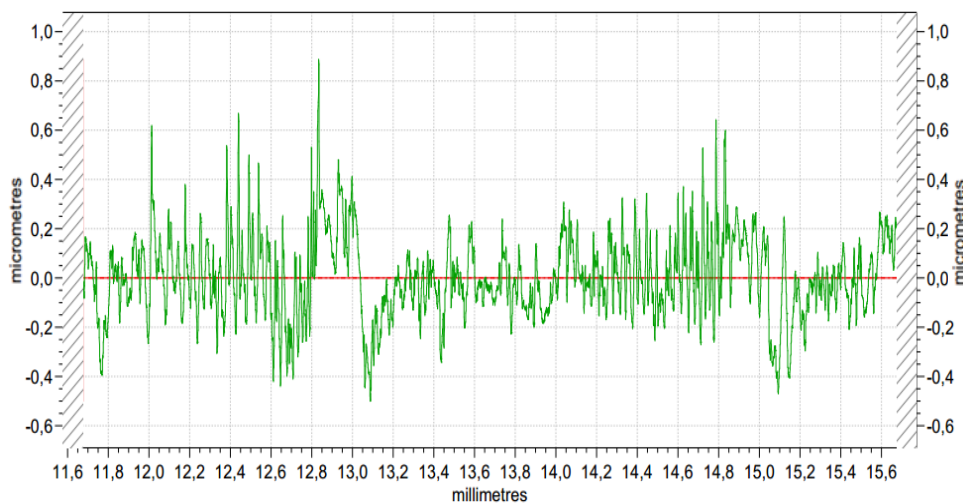


**Figure 5.8.** Measured Surface roughness profile of the material

Measured and simulated filter responses are in good agreement with each other, as shown in Figure 5.9. Measured insertion loss in passband is about 2.6 dB and return loss curve is below 10 dB level.

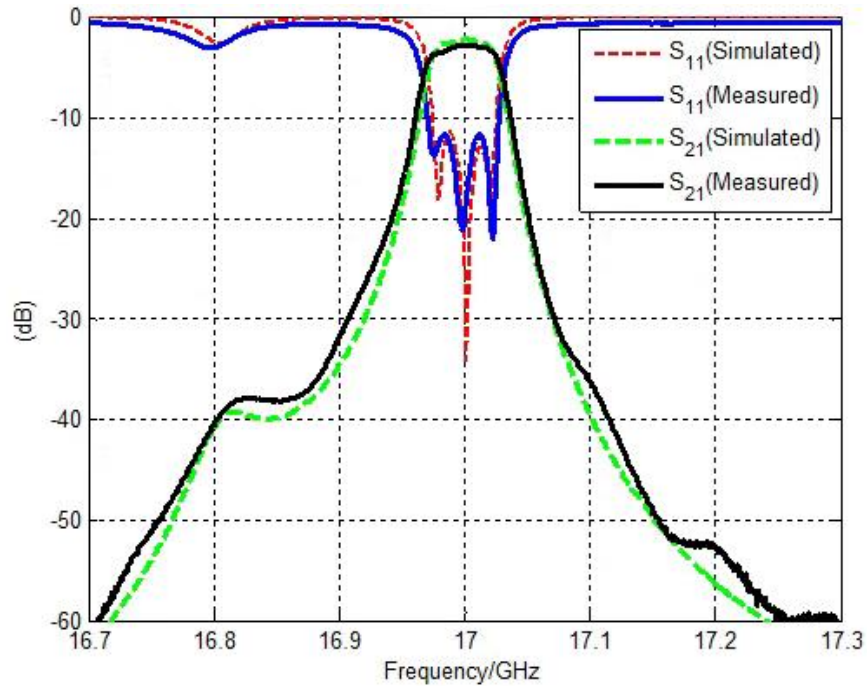


**Figure 5.9.** Transmission and reflection response of the channel filter

In order to characterize the effect of the sphere radius of the spherical nodules on conductor surface, corresponding exponential expression to the variation of the computed insertion in passband is investigated. For that purpose, curve-fitted exponential equation is defined as  $y = A + Be^{\frac{-\text{sphere radius}}{c}}$  where sphere radius is the RMS value for the radius of the spherical nodules on conductor surface and A, B, C are constant. Sphere radius varies between 0 and 3 $\mu\text{m}$  and corresponding values for those constants are determined as: A=0.485, B=0.394, C=0.426. Computed and fitted curves for the insertion in passband of the optimized channel filter are shown in Figure 5.10.

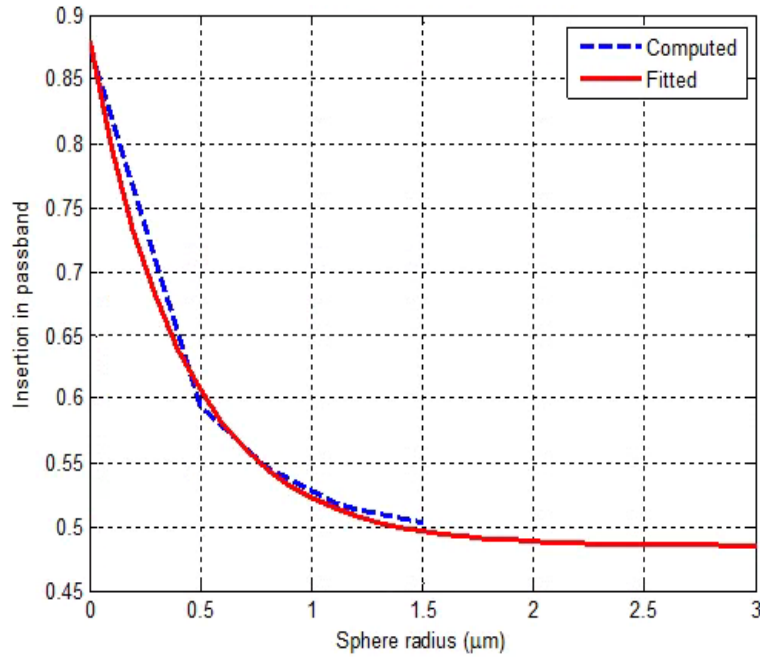


**Figure 5.10.** Computed and fitted insertion in passband of the filter.

Taking the surface roughness into account, stages of the design procedure for the channel filter can be summarized as follows:

- 1) Determine the surface roughness constant of the fabricated filter structure by analyzing the deteriorated measurement results.
- 2) Investigate the surface roughness values by inserting roughness resistance ( $R_{\text{rough}}$ ) and inductance ( $L_{\text{rough}}$ ) in circuit schematic and apply Huray's snowball approximation of surface roughness for all walls of the waveguide filter in full-wave simulation environment simultaneously. Find out  $R_{\text{rough}}$  and  $L_{\text{rough}}$  values for corresponding radius of spherically-rough surface in three-dimensional (3-D) filter structure.
- 3) After determining  $R_{\text{rough}}$  and  $L_{\text{rough}}$  values, insert only  $L_{\text{rough}}$  into the ideal circuit model and re-achieve the ideal filter response at beginning by exploiting local optimization and search algorithms.

- 4) After optimizing the parameter values in existence of  $L_{\text{rough}}$ , it is possible to construct 3-D filter structure and achieve desired filtering response by taking the surface roughness effect into account.
- 5) Fine-tune the resonator lengths, gap distances and iris thicknesses in 3-D full-wave model for optimum filter performance.
- 6) Realize fine-tuned channel filter structure and check filtering characteristics.





## **CHAPTER VI**

### **CONCLUSIONS**

This study focuses on accomplishing a deep literature survey on the waveguide filters, multiplexer configurations, conductor surface roughness effect and developing a systematic design procedure for miniaturized waveguide filter and multiplexers, modifying the design procedure involved in the influence of the surface roughness on filtering response. One chapter of this thesis addresses the prior and similar works in the literature includes comprehensive evaluations and assessments on them whilst the following two chapters undertake the systematic design procedure for the channel filter and multiplexer. Also, analysis of the surface roughness effect on filtering response and realization together with measurement activities are presented in one chapter of this thesis.

In Chapter 3, generalized design methodology is examined and versatile assessment of the various realization techniques is presented. Starting from the determination and calculation of the filter order, the procedure for the design of the narrowband, miniaturized and direct-coupled waveguide filter is mentioned thoroughly. Also, all derivations and simulation results both in full-wave and circuit level are illustrated with explanatory tables and curves.

In Chapter 4, multiplexer design studies using various approaches in literature are examined and a computer-aided design methodology for compact frequency multiplexer is mentioned. Design of the manifold junction is dwelled on and design steps are explained thoroughly by illustrating full-wave and circuit simulation

results. Design framework for the contiguous band multiplexer structures is developed as a result of the evaluation of the E-plane and H-plane manifold-coupled multiplexers.

In Chapter 5, fabrication details and experimental results are reported with explanatory comments and consequences. Mainly, significant outcomes of the investigation on the effect of the surface roughness on filtering response of the highly-selective and narrowband filtering response are demonstrated. A novel design methodology involving the surface roughness is proposed and several channel filters for different surface roughness constant are conceived and realized so as to inspect the validity of the procedure. Hence, a well consistency is observed between expected and measured performance of the channel filters. Moreover, TRL measurement set-up and surface profilometer curves for the fabricated channel filter are presented with all crucial findings.

Following the completion of comprehensive full-wave and circuit level computations and analysis involving surface roughness phenomena on miniaturized and narrowband waveguide filter, next, a number of channel filter realization performed and validation of the proposed technique was done successfully at the end of the comparison of the experimental and expected results.

In the scope of this thesis, accomplishments can be summarized as follows:

- A novel approach to extract the circuit model of the narrowband waveguide filter is developed and systematic design procedure with hybrid optimization technique is introduced for faster filter construction.
- Surface roughness phenomena is investigated versatilely and effect of it on high quality factor waveguide filters are examined. It is concluded that surface roughness becomes a dominant limiting factor for miniaturized and highly-selective waveguide configurations and ought to be considered at design stage properly. Taking this phenomena into consideration, desired filtering response is achieved successfully after the modification of the

design parameters such as resonator lengths, iris thicknesses and gap distances.

- Manifold-coupled multiplexer configurations are analyzed and detailed design study based on simultaneous circuit and full-wave optimization is completed. As an illustration, three-channel and six-channel contiguous band waveguide multiplexers are conceived and demonstrated.

For the future, one may focus on the realization of the manifold-coupled and contiguous band multiplexer by conceiving the narrowband and compact channel filters with manifold junctions considering conductor surface roughness effect.



## REFERENCES

- [1] Y. Zhang, “Modeling and design of microwave-millimeterwave filters and multiplexers,” 2006.
- [2] M. Latif and S. Lahore, “Design of 5- Channel C- Band Input Multiplexer for Communication Satellites,” *J. Space Technol.*, vol. 5, no. 1, 2015.
- [3] L. Rogla, M. T. Sancho-Ruiz-de-Castañeda, A. Álvarez Melcón, and S. Sobrino, “Predistorted Ku-band rectangular waveguide input filter,” 2013.
- [4] R. Cameron and M. Yu, “Design of manifold-coupled multiplexers,” *IEEE Microw. Mag.*, vol. 8, no. 5, pp. 46–59, Oct. 2007.
- [5] J. D. Rhodes and R. Levy, “A generalized multiplexer theory,” *IEEE Trans. Microw. Theory Tech.*, vol. 27, no. 2, pp. 99–111, 1979.
- [6] C. Rauscher, S. W. Kirchoefer, J. M. Pond, A. C. Guyette, and D. R. Jachowski, “A Compact Ridge-Waveguide Contiguous-Channel Frequency Multiplexer,” *IEEE Trans. Microw. Theory Tech.*, vol. 57, no. 3, pp. 647–656, Mar. 2009.
- [7] C. Rauscher, “Design of dielectric-filled cavity filters with ultrawide stopband Characteristics,” *IEEE Trans. Microw. Theory Tech.*, vol. 53, no. 5, pp. 1777–1786, May 2005.
- [8] C. Rauscher and S. W. Kirchoefer, “Miniature ridge-waveguide filter module employing moldable dielectric material,” *IEEE Trans. Microw. Theory Tech.*, vol. 54, no. 3, pp. 1190–1195, Mar. 2006.
- [9] J. R. Montejo-Garai, J. A. Ruiz-Cruz, and J. M. Rebollar, “Full-wave design of H-plane contiguous manifold output multiplexers using the fictitious reactive load concept,” *IEEE Trans. Microw. Theory Tech.*, vol. 53, no. 8, pp. 2628–2632, Aug. 2005.
- [10] L. Accatino and M. Mongiardo, “Hybrid circuit-full-wave computer-aided design of a manifold multiplexers without tuning elements,” *IEEE Trans. Microw. Theory Tech.*, vol. 50, no. 9, pp. 2044–2047, Sep. 2002.
- [11] C. Carceller, P. Soto, V. Boria, M. Guglielmi, and J. Gil, “Design of Compact Wideband Manifold-Coupled Multiplexers,” *IEEE Trans. Microw. Theory Tech.*, vol. 63, no. 10, pp. 3398–3407, Oct. 2015.

- [12] S. Cogollos *et al.*, “Efficient Design of Waveguide Manifold Multiplexers Based on Low-Order EM Distributed Models,” *IEEE Trans. Microw. Theory Tech.*, vol. 63, no. 8, pp. 2540–2549, Aug. 2015.
- [13] Maria Brumos Vicente, “Design of Microwave Filters And Multiplexers In Waveguide Technology Using Distributed Models,” Universidad Politecnica de Valencia, Valencia, 2014.
- [14] S. Shin and S. Kanamaluru, “Diplexer design using EM and circuit simulation techniques,” *Microw. Mag. IEEE*, vol. 8, no. 2, pp. 77–82, 2007.
- [15] J. R. Montejo-Garai, J. A. Ruiz-Cruz, and J. M. Rebollar, “Efficient Design of Contiguous-Band Elliptic-Response Manifold Output Multiplexers with Single-Terminated Filters,” *Electromagnetics*, vol. 30, no. 8, pp. 644–659, Dec. 2010.
- [16] A. Pons Abenza, M. Martinez-Mendoza, F. D. Quesada Pereira, and A. Alvarez-Melcon, “Design of manifold multiplexers in all-inductive dual-mode rectangular waveguide technology using the coupling matrix formalism: MULTIPLEXER WITH ALL-INDUCTIVE FILTERS,” *Radio Sci.*, vol. 51, no. 7, pp. 1065–1080, Jul. 2016.
- [17] A. Morini, T. Rozzi, M. Farina, and G. Venanzoni, “A New Look at the Practical Design of Compact Diplexers,” *IEEE Trans. Microw. Theory Tech.*, vol. 54, no. 9, pp. 3515–3520, Sep. 2006.
- [18] M. A. Ismail, D. Smith, A. Panariello, Y. Wang, and M. Yu, “EM-Based Design of Large-Scale Dielectric-Resonator Filters and Multiplexers by Space Mapping,” *IEEE Trans. Microw. Theory Tech.*, vol. 52, no. 1, pp. 386–392, Jan. 2004.
- [19] F. Loras-Gonzalez, S. Sobrino-Arias, I. Hidalgo-Carpintero, D. Segovia-Vargas, and M. Salazar-Palma, “A novel Ku-band dielectric resonator triplexer based on generalized multiplexer theory,” in *Microwave Symposium Digest (MTT), 2010 IEEE MTT-S International*, 2010, pp. 884–887.
- [20] K.-L. Wu and W. Meng, “A Direct Synthesis Approach for Microwave Filters With a Complex Load and Its Application to Direct Diplexer Design,” *IEEE Trans. Microw. Theory Tech.*, vol. 55, no. 5, pp. 1010–1017, May 2007.
- [21] J. A. Ruiz-Cruz, J. R. Montejo-Garai, J. M. Rebollar Machain, and S. Sobrino, “Compact full Ku-band triplexer with improved E-plane power divider,” *Prog. Electromagn. Res.*, vol. 86, pp. 39–51, 2008.
- [22] J. M. Rebollar and J. Esteban, “A modified E-plane trifurcation and its application to broadband triplexers,” in *Antennas and Propagation Society International Symposium, 2001. IEEE*, 2001, vol. 2, pp. 242–245.
- [23] J. Dittloff and F. Arndt, “Rigorous field theory design of millimeter-wave E-plane integrated circuit multiplexers,” *IEEE Trans. Microw. Theory Tech.*, vol. 37, no. 2, pp. 340–350, 1989.

- [24] A. Morini, T. Rozzi, and M. Morelli, “New formulae for the initial design in the optimization of T-junction manifold multiplexers,” in *Microwave Symposium Digest, 1997., IEEE MTT-S International*, 1997, vol. 2, pp. 1025–1028.
- [25] A. Morini, T. Rozzi, and M. Mongiardo, “Efficient CAD of wideband contiguous channel multiplexers,” in *Microwave Symposium Digest, 1996., IEEE MTT-S International*, 1996, vol. 3, pp. 1651–1654.
- [26] F. M. Vanin, D. Schmitt, and R. Levy, “Dimensional Synthesis for Wide-Band Waveguide Filters and Diplexers,” *IEEE Trans. Microw. Theory Tech.*, vol. 52, no. 11, pp. 2488–2495, Nov. 2004.
- [27] Y. Wang, S. Li, and M. Yu, “Hybrid Models for Effective Design and Optimization of Large-Scale Multiplexing Networks,” *IEEE Trans. Microw. Theory Tech.*, vol. 61, no. 5, pp. 1839–1849, May 2013.
- [28] M. Yu and Y. Wang, “Enhanced Microwave Multiplexing Network,” *IEEE Trans. Microw. Theory Tech.*, vol. 59, no. 2, pp. 270–277, Feb. 2011.
- [29] S. Li and Y. Wang, “Design of enhanced microwave multiplexing networks with H-plane T-junctions,” in *Microwave Conference Proceedings (APMC), 2011 Asia-Pacific*, 2011, pp. 1066–1069.
- [30] S. Q. Li, “Effective Design of Multiplexing Networks for Applications in Communications Satellites,” University of Ontario Institute of Technology, 2011.
- [31] P. Jarry, *Design and realizations of miniaturized fractal RF and microwave filters*. Hoboken, N.J: Wiley, 2009.
- [32] R. V. Snyder and S. Bastioli, “Broad Passband, Wide Stopband, High Power Evanescent Mode Filters Using Capacitively-Loaded Ridges,” in *Microwave Conference (EuMC), 2012 42nd European*, 2012, pp. 176–179.
- [33] Elif İnan, “A New Finite Transmission Zero Generation Technique In Evanescent Mode Waveguide Comblines Filters,” Middle East Technical University, Ankara, 2014.
- [34] Q. Zhang and T. Itoh, “Computer-aided design of evanescent-mode waveguide filter with nontouching E-plane fins,” *Microw. Theory Tech. IEEE Trans. On*, vol. 36, no. 2, pp. 404–412, 1988.
- [35] G. F. Craven and C. K. Mok, “The design of evanescent mode waveguide bandpass filters for a prescribed insertion loss characteristic,” *Microw. Theory Tech. IEEE Trans. On*, vol. 19, no. 3, pp. 295–308, 1971.
- [36] P. Ludlow, V. Fusco, G. Goussetis, and D. E. Zelenchuk, “Applying Band-Pass Filter Techniques to the Design of Small-Aperture Evanescent-Mode Waveguide Antennas,” *IEEE Trans. Antennas Propag.*, vol. 61, no. 1, pp. 134–142, Jan. 2013.

- [37] Y. C. S. K. G. Gray, "Analysis and design of evanescent-mode waveguide dielectric resonator filters," presented at the IEEE MTT-S International Microwave Symposium Digest, 1984, vol. Vol.84, pp. 238–239.
- [38] T. Zaki, "Length reduction of evanescent-mode ridge waveguide bandpass filters," *Prog. Electromagn. Res.*, vol. 40, pp. 71–90, 2003.
- [39] V. Tornielli Di Crestvolant, "Ridge waveguide bandpass filters for satellite applications," 2010.
- [40] S. B. Cohn, "Direct-coupled-resonator filters," *Proc. IRE*, vol. 45, no. 2, pp. 187–196, 1957.
- [41] A. E. Atia and A. E. Williams, "Narrow-bandpass waveguide filters," *Microw. Theory Tech. IEEE Trans. On*, vol. 20, no. 4, pp. 258–265, 1972.
- [42] H.-C. Chang and K. A. Zaki, "Evanescent-mode coupling of dual-mode rectangular waveguide filters," *Microw. Theory Tech. IEEE Trans. On*, vol. 39, no. 8, pp. 1307–1312, 1991.
- [43] M. Guglielmi, P. Jarry, E. Kerherve, O. Roquebrun, and D. Schmitt, "A new family of all-inductive dual-mode filters," *IEEE Trans. Microw. Theory Tech.*, vol. 49, no. 10, pp. 1764–1769, 2001.
- [44] M. M. Mendoza, D. M. Martinez, D. C. Rebenaque, and A. Alvarez-Melcon, "Enhanced topologies for the design of dual-mode filters using inductive waveguide structures," *Radio Sci.*, vol. 50, no. 1, pp. 66–77, Jan. 2015.
- [45] P. Soto, E. Tarin, V. E. Boria, C. Vicente, J. Gil, and B. Gimeno, "Accurate Synthesis and Design of Wideband and Inhomogeneous Inductive Waveguide Filters," *IEEE Trans. Microw. Theory Tech.*, vol. 58, no. 8, pp. 2220–2230, Aug. 2010.
- [46] P. Soto, A. Bergner, J. L. Gomez, V. E. Boria, and H. Esteban, "Automated design of inductively coupled rectangular waveguide filters using space mapping optimization," *Eur Congr Comput. Methods Appl. Sci. Eng. Barc. Spain*, 2000.
- [47] M. Guglielmi, A. Alvarez, and G. Gheri, "Multimode synthesis procedure for microwave filters based on thick inductive windows," in *Microwave Symposium Digest, 1993., IEEE MTT-S International*, 1993, pp. 447–450.
- [48] Qianqian Wang, "Synthesis and Design of Direct-Coupled Rectangular Waveguide Filters with Arbitrary Inverter Sequence."
- [49] I. C. Hunter, L. Billonet, B. Jarry, and P. Guillon, "Microwave filters-applications and technology," *Microw. Theory Tech. IEEE Trans. On*, vol. 50, no. 3, pp. 794–805, 2002.
- [50] M. S. Uhm, J. Lee, J. H. Park, and J. P. Kim, "An efficient optimization design of a manifold multiplexer using an accurate equivalent circuit model of coupling irises of channel filters," in *Microwave Symposium Digest, 2005 IEEE MTT-S International*, 2005, p. 4–pp.



- [51] S. B. Cohn, "Microwave bandpass filters containing high-Q dielectric resonators," *Microw. Theory Tech. IEEE Trans. On*, vol. 16, no. 4, pp. 218–227, 1968.
- [52] S. Moraud, S. Verdeyme, P. Guillon, Y. Latouche, S. Vigneron, and B. Theron, "A new dielectric loaded cavity for high power microwave filtering," in *Microwave Symposium Digest, 1996., IEEE MTT-S International, 1996*, vol. 2, pp. 615–618.
- [53] R. Borowiec, "Dielectric resonator filters," in *Microwaves, Radar, and Wireless Communication (MIKON), 2014 20th International Conference on*, 2014, pp. 1–4.
- [54] J.-F. Liang, K. A. Zaki, and A. E. Atia, "Mixed modes dielectric resonator filters," *IEEE Trans. Microw. Theory Tech.*, vol. 42, no. 12, pp. 2449–2454, 1994.
- [55] V. Boria and B. Gimeno, "Waveguide filters for satellites," *IEEE Microw. Mag.*, vol. 8, no. 5, pp. 60–70, Oct. 2007.
- [56] R. Lopez-Villarroya and others, "E-plane parallel coupled resonators for waveguide bandpass filter applications," Heriot-Watt University, 2012.
- [57] G. Goussetis, R. Lopez-Villarroya, E. Dومانis, O. S. Arowolo, and J.-S. Hong, "Quality factor of E-plane periodically loaded waveguide resonators and filter applications," *IET Microw. Antennas Propag.*, vol. 5, no. 7, p. 818, 2011.
- [58] L. Harle, "Microwave micromachined cavity filters," Citeseer, 2003.
- [59] W. Gautier, A. Stehle, B. Schoenlinner, V. Ziegler, U. Prechtel, and W. Menzel, "Low-loss micro-machined four-pole linear phase filter in silicon technology," in *Microwave Conference, 2009. EuMC 2009. European, 2009*, pp. 1413–1416.
- [60] A. Q. A. Qureshi, "Multilayer Micromachined RF MEMS Filters at Ka and L/S Band For On-Board Satellite Communication Systems," University of Trento, 2013.
- [61] C. A. D. Morcillo, B. Lacroix, H. Gu, J. Miller, and J. Papapolymerou, "Compact and low-cost topology for evanescent-mode waveguide filters with dielectric loading in the X Band," in *Microwave Conference (EuMC), 2012 42nd European, 2012*, pp. 172–175.
- [62] N. Marcuvitz, *Waveguide Handbook*. McGraw-Hill Book, 1985.
- [63] C. Pérez-Arancibia, P. Zhang, O. P. Bruno, and Y. Y. Lau, "Electromagnetic power absorption due to bumps and trenches on flat surfaces," *J. Appl. Phys.*, vol. 116, no. 12, p. 124904, 2014.
- [64] S. P. Morgan, "Effect of Surface Roughness on Eddy Current Losses at Microwave Frequencies," *J. Appl. Phys.*, vol. 20, no. 4, pp. 352–362, Apr. 1949.

- [65] X. Ma, "Modeling of conductor surface roughness effect," University of Illinois at Urbana-Champaign, Urbana, Illinois, 2014.
- [66] S. Hall *et al.*, "Multigigahertz Causal Transmission Line Modeling Methodology Using a 3-D Hemispherical Surface Roughness Approach," *IEEE Trans. Microw. Theory Tech.*, vol. 55, no. 12, pp. 2614–2624, Dec. 2007.
- [67] M. V. Lukic and D. S. Filipovic, "Modeling of 3-D Surface Roughness Effects With Application to  $\mu$ -Coaxial Lines," *IEEE Trans. Microw. Theory Tech.*, vol. 55, no. 3, pp. 518–525, Mar. 2007.
- [68] C. L. Holloway and E. F. Kuester, "Power loss associated with conducting and superconducting rough interfaces," *IEEE Trans. Microw. Theory Tech.*, vol. 48, no. 10, pp. 1601–1610, 2000.
- [69] L. Proekt and A. C. Cangellaris, "Investigation of the impact of conductor surface roughness on interconnect frequency-dependent ohmic loss," in *Electronic Components and Technology Conference, 2003. Proceedings. 53rd, 2003*, pp. 1004–1010.
- [70] P. G. Huray *et al.*, "Fundamentals of a 3-D 'snowball' model for surface roughness power losses," in *Signal Propagation on Interconnects, 2007. SPI 2007. IEEE Workshop on, 2007*, pp. 121–124.
- [71] Y. Shlepnev and C. Nwachukwu, "Roughness characterization for interconnect analysis," in *Electromagnetic Compatibility (EMC), 2011 IEEE International Symposium on, 2011*, pp. 518–523.
- [72] A. C. Scogna and M. Schauer, "Performance analysis of stripline surface roughness models," in *Electromagnetic Compatibility-EMC Europe, 2008 International Symposium on, 2008*, pp. 1–6.
- [73] B. Curran, I. Ndip, S. Guttowski, and H. Reichl, "On the quantification and improvement of the models for surface roughness," in *Signal Propagation on Interconnects, 2009. SPI'09. IEEE Workshop on, 2009*, pp. 1–4.
- [74] Leung Tsang, Xiaoxiong Gu, and H. Braunisch, "Effects of random rough surface on absorption by conductors at microwave frequencies," *IEEE Microw. Wirel. Compon. Lett.*, vol. 16, no. 4, pp. 221–223, Apr. 2006.
- [75] Ruihua Ding, L. Tsang, and H. Braunisch, "Wave Propagation in a Randomly Rough Parallel-Plate Waveguide," *IEEE Trans. Microw. Theory Tech.*, vol. 57, no. 5, pp. 1216–1223, May 2009.
- [76] J. A. R. Cruz, "Contribution to the CAD of Microwave-Millimeterwave Passive Devices by Mode-Matching Techniques.," PhD thesis, Univ. PolitÈcnica de Madrid, Madrid, Spain.
- [77] G. M. L. Young, E.M.T. Jones, *Microwave Filters, Impedance-Matching Networks, and Coupling Structures*. Denham, Massachusetts: Artech Microwave Library, 1980.

- [78] R. Levy, "Theory of direct-coupled-cavity filters," *Microw. Theory Tech. IEEE Trans. On*, vol. 15, no. 6, pp. 340–348, 1967.
- [79] Yifan Wang, "Novel Design Approach for High Performance Waveguide Filters," University of Waterloo, Waterloo, Ontario, Canada, 2008.
- [80] P. Mohammadi, "Low loss substrate integrated waveguide N-way power divider," Middle East Technical University, 2012.
- [81] L. Li, K. Wu, and P. Russer, "On the thru-reflect-line (TRL) numerical calibration and error analysis for parameter extraction of circuit model," *Int. J. RF Microw. Comput.-Aided Eng.*, vol. 16, no. 5, pp. 470–482, Sep. 2006.
- [82] L. Simonovich, "Practical method for modeling conductor roughness using cubic close-packing of equal spheres," in *Electromagnetic Compatibility (EMC), 2016 IEEE International Symposium on*, 2016, pp. 917–920.
- [83] X. Ma, "Modeling of conductor surface roughness effect," 2015.



# CURRICULUM VITAE

## PERSONAL INFORMATION

---

**Surname, Name:** Sevinç, Yusuf

**Nationality:** Turkish

**Date and Place of Birth:** 07 December 1988, Eskişehir

**Phone:** +90 312 210 4417

**Fax:** +90 312 210 2301

**E-mail:** ysevinc@metu.edu.tr

## EDUCATION

---

Degree	Institution	Graduation Year
B.S.	Süleyman Demirel University Electronics and Communication Eng.	2010
High School	Muzaffer Demir Anadolu Lisesi	2006

## WORK EXPERIENCE

---

Year	Place	Enrollment
2011-Present	METU EEE	Research Asistant
2010-2011	Bartın University EEE	Research Asistant
August 2008	Havelsan Inc	Summer Practice
July 2009	Turkish Telecom Inc.	Summer Practice

## HONORS AND AWARDS

---

- Ranked 1<sup>st</sup> among SDU ECE BS graduates of the 2006-2010 term.
- Ranked 1<sup>st</sup> among Muzaffer Demir Anadolu Lisesi graduates of the 2006 year

## PUBLICATIONS

---

### International Journal Publications

- **Y. Sevinc** and S. Demir, “Waveguide multiplexer: miniaturized contiguous-band six-channel multiplexer structure,” *IET Journal of Engineering*, August 2017
- **Y. Sevinc** and A. Kaya, “Reconfigurable antenna structure for RFID system applications using varactor-loading technique” *Turkish Journal of Electrical Engineering and Computer Sciences*, vol. 20, no. 4, pp. 453–462, 2012.

### International Conference Publications

- O. Bayraktar, **Y. Sevinc**, O. A. Civi, S. Demir, and S. Koc, “Ka-band phased array antenna with circular rim,” in *2015 IEEE International Symposium on Antennas and Propagation & USNC/URSI National Radio Science Meeting*, 2015, pp. 2479–2480.
- O. Bayraktar, E. Kobal, **Y. Sevinc**, C. Cetintepe, I. Comart, K. Demirel, E. S. Topalli, T. Akin, S. Demir, and O. A. Civi, “RF MEMS based millimeter wave phased array for short range communication,” in *2015 9th European Conference on Antennas and Propagation (EuCAP)*, 2015, pp. 1–5.

- **Y. Sevinc** and A. Kaya, “Enhancement of ISM band RFID system performance with varactor-loaded compact RFID tag antenna” in *2010 10th Mediterranean Microwave Symposium*, 2010, pp. 130–134.